UILU-ENG 88-3601

Report No. 140

# A MICRO-MECHANISTIC LIFE PREDICTION MODEL SUITABLE FOR ISOTHERMAL AND THERMO-MECHANICAL FATIGUE

by

Richard W. Neu
Materials and Design Division
Department of Mechanical and Industrial Engineering

A Report of the

MATERIALS ENGINEERING - MECHANICAL BEHAVIOR

College of Engineering, University of Illinois at Urbana-Champaign

January 1988

# A MICRO-MECHANISTIC LIFE PREDICTION MODEL SUITABLE FOR ISOTHERMAL AND THERMO-MECHANICAL FATIGUE

BY

RICHARD WILLIAM NEU

B.S., University of Illinois, 1986

THESIS

Submitted in partial fulfillment of the requirements
for the degree of Master of Science in Mechanical Engineering
in the Graduate College of the
University of Illinois at Urbana-Champaign, 1988

Urbana, Illinois

# A MICRO-MECHANISTIC LIFE PREDICTION MODEL SUITABLE FOR ISOTHERMAL AND THERMO-MECHANICAL FATIGUE

## ABSTRACT

A life prediction model is developed for crack nucleation and early crack growth based on fatigue, environment (oxidation), and creep damage. The model handles arbitrary strain-temperature phasings (i.e., in-phase and out-of-phase thermo-mechanical fatigue, isothermal fatigue, and others including non-proportional phasings). It works for a broad range of temperatures, strain rates, and strain ranges. An oxide growth model is presented which describes oxide growth as a repeated micro-rupture process. Using this model, an oxidation damage expression is derived with constants directly linked to micro-mechanistic measurements in oxide growth. A creep damage expression, which is stress based, is coupled with a unified constitutive equation. A set of interrupted tests were performed to provide valuable damage progression information. Tests are performed in a helium atmosphere to isolate creep damage from oxidation damage. Fatigue life predictions compare favorably with experiments in 1070 steel for a wide range of test conditions and strain-temperature phasings.

# ACKNOWLEDGMENT

This research was funded by the Association of American Railroads, Technical Center, Chicago, Illinois. The cooperation of Dr. Daniel Stone and Mr. Michael C. Fec is gratefully acknowledged.

My advisor, Professor Huseyin Sehitoglu, is acknowledged for his pertinent insight and technical advice, as well as the freedom he has given me to pursue my research. His time spent in discussions and review of this research is greatly appreciated.

I would also like to acknowledge the assistance from Mr. Mark Karasek and Mr. Don Slavik. They performed some of the experimental tests in this report. Their instruction and timely advice during my early years as a research assistant were especially worthwhile. Also, Miss Nina Sluz is thanked for helping with experiments and writing computer programs.

I thank all my friends and colleagues for their continuing support through the thick and thin. Lastly, my parents are thanked for their continued support and encouragement throughout my education. They have always given me the freedom to pursue my own goals.

TABLE OF CONTENTS

## LIST OF TABLES

LIST OF FIGURES

# NOMENCLATURE

| | |
|---|---|
| $A$ | coefficient in creep damage equation |
| $A_c$ | flow rule coefficient in constitutive law |
| $a$ | strain rate sensitivity constant in oxidation term |
| $B$ | coefficient in oxidation growth equation |
| $b$ | fatigue strength exponent |
| $c$ | fatigue ductility exponent |
| $D_o$ | diffusion coefficient for oxidation |
| $D^{creep}$ | creep damage per cycle |
| $D^{fat}$ | fatigue damage per cycle |
| $D^{ox}$ | oxidation damage per cycle |
| $D^{tot}$ | total damage per cycle |
| $E$ | Young's modulus |
| $h_{cr}$ | critical total oxide growth when oxidation-induced crack growth ends and rapid crack growth begins |
| $h_{fi}$ | critical oxide layer thickness at fracture |
| $\bar{h}_f$ | average value of the critical oxide layer thickness at fracture |
| $h_i$ | oxide intrusion depth |
| $h_o$ | total oxide growth |
| $h_s$ | surface oxide thickness |
| $K$ | drag stress |
| $K_p$ | parabolic oxidation constant |
| $K_p^{eff}$ | effective parabolic oxidation constant |
| $K_{sat}$ | saturated drag stress |
| $N$ | number of cycles |
| $N_f$ | number of cycles to specimen failure |
| $N_f^{creep}$ | number of cycles to failure from creep damage |
| $N_f^{exp}$ | number of cycles to failure from experimental tests |
| $N_f^{fat}$ | number of cycles to failure from fatigue damage |
| $N_f^{ox}$ | number of cycles to failure from oxidation damage |
| $N_f^{P}$ | long crack propagation life (cycles) |
| $N_f^{tot}$ | total number of cycles of a component |
| $Q$ | activation energy for oxidation |
| $R$ | universal gas constant |

| | |
|---|---|
| $T$ | temperature |
| $T_{max}$ | maximum temperature of a TMF cycle |
| $T_{min}$ | minimum temperature of a TMF cycle |
| $T_o$ | initial temperature of a TMF cycle |
| $t$ | time |
| $t_c$ | period of a cycle |
| $\alpha$ | back stress |
| $\alpha_o$ | expansion coefficient |
| $\alpha_1, \alpha_2$ | constants which represent the asymmetry of creep damage |
| $\beta$ | exponent on time in oxidation growth equation |
| $\Delta\varepsilon_{mech}$ | mechanical strain range |
| $\Delta H$ | activation energy for the rate-controlling creep mechanism |
| $\Delta H_c$ | activation energy in constitutive law |
| $\Delta K$ | stress intensity range |
| $\delta_o$ | measure of oxide ductility (material constant) |
| $\varepsilon_{mech}$ | mechanical strain |
| $\varepsilon_{th}$ | thermal strain |
| $\varepsilon'_f$ | fatigue ductility coefficient |
| $\dot{\bar{\varepsilon}}^{in}$ | equivalent inelastic strain rate |
| $\dot{\varepsilon}, \dot{\varepsilon}_{mech}$ | mechanical strain rate |
| $\dot{\varepsilon}_{th}$ | thermal strain rate |
| $\Phi^{creep}$ | phasing factor for creep |
| $\Phi^{ox}$ | phasing factor for oxidation |
| $\phi^{creep}$ | phasing function for creep |
| $\phi^{ox}$ | phasing function for oxidation |
| $\nu$ | frequency |
| $\sigma_H$ | hydrostatic stress |
| $\sigma_x$ | stress in a uniaxial test |
| $\bar{\sigma}$ | effective stress |
| $\sigma'_f$ | fatigue strength coefficient |
| $\xi^{creep}$ | shape factor for creep phasing function |
| $\xi^{ox}$ | shape factor for oxidation phasing function |

# 1. INTRODUCTION

## 1.1 Background

Hot sections of turbine engines, piping, pressure vessels, boiler tubes, and railroad wheels undergo varying strain-temperature histories. Life prediction models are needed to assist the engineer with the design and evaluation of these components. The models currently available are severely limited in their generality. In many of the current life prediction models only one or two parameters were considered when the model was formulated. This severely limits the application of the model outside the range of experiments used to derive the model. Since the mechanisms producing damage may be differ from one set of testing conditions to another, advancement in the area of life prediction needs to be in the identification of these different damage mechanisms, and the conditions which activate them. Microstructure and bulk parameters which quantify these mechanisms should be established. The model derived in this report attempts to take advantage of physical damage measurements and identifies these with a measure of lifetime.

Two types of high temperature fatigue tests are typically performed in the laboratory. These are isothermal fatigue, which are tests performed at a constant temperature, and thermo-mechanical fatigue, which involve tests performed under varying strain and temperature histories. There has been more data reported for the simpler isothermal fatigue tests; however, many critical components, such as hot turbine engine parts [1], undergo a complicated history which can be more closely approximated by a thermo-mechanical fatigue test in the laboratory. Therefore, it is important that the new generation of life prediction models are able to handle these complicated phasings of strain-temperature histories, and yet remain general enough so that the prediction model is not restricted to only a few temperature, strain rate, or strain range levels.

When elevated temperature experiments are conducted, environmental and creep effects on the life can become significant depending on the material and testing parameters. Both environmental effects and creep are activated simultaneously with fatigue and lower the life. Most high temperature life prediction models consider one of these additional damage mechanisms, but until recently seldom considered both effects. In most cases the strain-temperature variation with time and the material condition will dictate which mechanism is the most damaging.

## 1.2 Current Life Prediction Models for High Temperature Fatigue

### 1.2.1 Oxidation-Fatigue Models

There have been many different life prediction models proposed that incorporate some type of high temperature environmental effects (oxidation). The earliest life prediction model to take into account environmental effects is the frequency-modified strain-life equation [2] which included, in addition to the plastic strain range, a frequency factor which accounted for the effect of oxidation.

Another class of high temperature life prediction methods is the strain range partitioning method [3]. Originally, it was developed to handle the life prediction of a strain cycle, containing both plastic and creep strain components, but underlying mechanisms and parameters associated with the oxidation were not directly used. Recently, this method was modified to account for the effects of time dependence [4]. However, the uncertainty prevails whether hold-time effects are attributed to oxidation or creep damage in the material.

Some oxidation models have been derived using a micro-mechanistic approach and the structure of these models are discussed here. The early work on oxidation-fatigue interaction considered the effect of hold times on lifetime. These life prediction models are configured to handle either "crack initiation or crack growth to a certain size" with modified

low cycle fatigue equations or "long crack growth" with modified fracture mechanics parameters.

Challenger et al. [5] developed a model which predicts the cycles to initiate a surface oxide crack. The oxide is assumed to be at a zero strain state in compression, so that when the applied strain is reversed, a tensile strain in the oxide equal in magnitude to the total applied strain range easily causes oxide fracture. Therefore, the model predicts that under oxidizing conditions compression holds are more damaging than tension holds. This model does not take into account any creep effects for the $2\frac{1}{4}$ Cr-1 Mo alloy steel at 593°C, the highest temperature considered for this material in this study. In the absence of hold times the oxidation effect changes with strain rate (or frequency), and this was not considered in the model.

Using the parabolic oxidation law to characterize oxidation of surface connected grain boundaries in Rene 80, Antolovich et al [6,7] were able to derive a fatigue life equation. Crack initiation is assumed to occur when a critical combination between maximum stress and depth of the oxide spike at the grain boundaries is reached. The initiation fatigue lives were shown to decrease linearly with total cycle period and with hold times.

Saxena et al.'s [8] interest was in growth of long cracks; therefore, they proposed an oxidation-modified crack growth law involving $\Delta K$. Kinetics of oxidation (parabolic) at crack tips was included in the model. The model predicted that the growth rate due to oxidation increased with hold time to one-half power. The model was tested for several steels and Ni-base superalloys and provided satisfactory correlation. Liu and Oshida [9] have a model similar to Saxena et al.; however, they predict a linear dependence of growth rate with hold times or with strain rate.

Reuchet and Remy [10] developed a model by recognizing the accelerated oxide growth rate with increasing applied strain range. They postulated that an environmental crack advance involved both matrix oxidation and preferential oxidation of MC carbides

found in the cast cobalt-base superalloy MARM 509. Then the total crack growth is the sum of the crack advance due to the fatigue process and environmental process (established by metallographic measurements). This is in principle similar to the approach of Skelton and Bucklow [11].

To better understand the effect of the environment, many investigators [12-17] have performed tests in inert gas environments or in vacuum and compared these to tests performed in air or other oxidizing environments. These studies along with the present study indicate that a factor of 1.5 to 12 decrease in life in air is observed compared to tests in a non-oxidizing environment. This wide range of factors can be attributed to the material composition and testing parameters (e.g., temperature, strain range, and strain rate). At lower temperatures, when the material is less susceptible to environmental factors, one would not expect to observe a large difference in life comparing air and inert atmospheres. In addition, increasing the strain rate (frequency) reduces the time for the environmental species to attack the material; in this case the difference in life between air and the inert atmosphere would be minimal.

Some attempts have been made to predict thermo-mechanical fatigue behavior based on isothermal behavior [13,18,19]; however, the oxidation-induced damage micro-mechanisms occurring during a TMF cycle can be different from an isothermal cycle. Furthermore, the question of which isothermal temperature should be used to predict TMF data based on isothermal fatigue data is not resolved. Some critical TMF tests should be performed including experiments where oxidation damage is eliminated with environmental control. These tests and isothermal tests at different strain rates will be shown to be sufficient to build a consistent model which resolves many of the issues.

In the present life prediction model helium atmosphere tests are used to separate the oxidation, creep, and fatigue effects. The proposed model also differentiates between rupture of an initial surface oxide layer and the subsequent oxide rupture at crack tips.

1.2.2 Creep-Fatigue Models

The problem of creep-fatigue interaction has been addressed in early work. The strain range partitioning method [3] and time-cycle fraction rule (adopted as an ASME code [20]) were developed to handle plastic and creep strains on life. A modified time-cycle fraction rule has been used with applications to cumulative damage and may be found in Refs. [21-26]. The advantage of the cumulative damage approach is that past damage accumulation can affect current deterioration of the material. However, the expression for the evolution of damage is empirical, and each cycle must be integrated and then summed to obtain a total damage.

Many researchers have considered creep-fatigue to be a propagation-controlled problem where the damage micro-mechanism considered is assumed to influence the fatigue crack growth, or vise versa. Majumdar and Maiya [27] considered the influence of creep cavity growth ahead of a crack growing by fatigue in their damage-rate equations. In their model it is assumed that sintering of cavities occurs in compression, effectively reversing the creep damage occurring in tension. These damage-rate equations have recently been applied to thermo-mechanical fatigue loadings [28].

In crack propagation-controlled models the creep damage in a material is bounded by two extremes [29]. When no creep damage is present, the damage at the crack tip is given by the plastic zone size; when creep damage is extensive, it is assumed that plastic-creep zone ahead of the crack in the bulk of the material controls damage growth [29]. This model is analogous to the use of crack tip displacement parameter to characterize fatigue-creep crack growth [30].

Cavity formation ahead of a crack tip modifies the crack tip stress fields; therefore, modified fracture mechanics parameters have been used [8,9,31] to handle fatigue-creep crack growth. In the absence of cavities the crack tip stress/strain fields are still modified and this is reflected in the model of Nair and Tien [32]. However, it is uncertain whether the time-dependent effect in these modified fracture mechanics parameters results solely

from creep or some environmental damage in the form of grain boundary oxidation is present. Other micro-mechanisms which have been considered in creep-fatigue interactions include intergranular damage (nucleation and growth of grain boundary cavities without aid from a major crack) [33,34], growth of small cracks [16], and models for grain boundary sliding [35-37].

Experiments are needed to isolate the fatigue-creep effects from the oxidation effects allowing the constants in the creep damage term to be formulated directly. This could be accomplished by performing tests in helium environment which eliminates oxidation damage and thus isolates the creep damage from the environmental damage. The model proposed in this report is based on the type of experiments suggested above. Specifically the model (a) is coupled with a unified constitutive equation, (b) accounts for intergranular damage observed in conditions where creep damage is dominant, and (c) handles arbitrary strain-temperature histories (phasing).

## 1.3 Thermo-mechanical Fatigue and Phasing of Temperature and Strain

An important issue for fatigue at high temperatures is the development of a life prediction methodology which accounts for the arbitrary phasing of the mechanical strain and temperature on both oxidation and creep damage progression in the material. Baseline thermo-mechanical fatigue (TMF) studies usually involve both out-of-phase (maximum strain at minimum temperature) and in-phase (maximum strain at maximum temperature) testing. Illustrated in Fig. 1 are the phasings considered in current tests on 1070 steel. Note that mechanical strain is plotted against thermal strain which is related to temperature by

$$\varepsilon_{th} = \alpha_o(T-T_o) \tag{1.1}$$

where $\alpha_o$ is the thermal expansion coefficient (= $1.7 \times 10^{-5}$ 1/°C for 1070 steel), and $T_o$ is the initial temperature. If $\alpha_o$ varies with temperature, the right-hand side of Eq. 1.1 is evaluated by integration. The phasings in Fig. 1 are all proportional which means $\dot{\varepsilon}_{th}/\dot{\varepsilon}_{mech}$ remains constant throughout the cycle. Discussions of the mechanical behavior of 1070 steel under these phasings are given in Refs. [38-41].

In general, non-proportional phasing of mechanical strain and temperature should also be considered and may be more typical of the strain-temperature history of actual components. One example of a non-proportional phasing that has been considered in testing is the diamond-shaped [42-44] as shown in Fig. 2. A few researchers have considered and performed testing using non-proportional strain-temperature phasings [1,42-44]. However, there are no accepted life prediction methods to handle strain-temperature phasing. The proposed life prediction model has the potential to deal with these non-proportional phasings.

## 1.4 Experimental Work

The material considered in this study is 1070 steel which is typically used in railroad wheels. The chemical composition of the material is given in Table 1. The microstructure consists of pearlite colonies of 50 μm size with pearlite spacing of 0.5 to 1.0 μm. Details of microstructure, constitutive response, and experimental techniques are described elsewhere [18,39,45,46]. A wide range of tests have been performed on this material and are also reported in these references. These include isothermal tests performed at temperatures ranging from 20°C to 700°C and strain rates 0.02, 0.002, and 0.0002 $sec^{-1}$. Many TMF tests have been performed with the phasings indicated in Fig. 1. In these TMF tests a wide range of minimum temperatures (150°C to 550°C) and maximum temperatures (350°C to 700°C) have been considered in the testing program.

### 1.4.1 Experiments in Helium Atmosphere

In addition, helium atmosphere tests were performed under both isothermal (two strain rates examined) and TMF conditions (both out-of-phase total constraint and in-phase examined). These test results are used to distinguish the creep damage from the oxidation damage. The specimens tested in the helium atmosphere consisted of a specimen with its reduced section sealed from the outside atmosphere with bellows as shown in Fig. 3. Also shown in the figure is a photo of the specimen without bellows. The center convolutions of the bellows are made of stainless steel and were included to provide flexibility. The remainder of the bellows is composed of Inconel tubes that are able to couple with the induction coils used to heat the specimen. Induction inherently heats the bellows to a greater extent than the specimen gage section; consequently, the bellows must be able to endure temperatures much higher than the testing temperature of the specimen.

Except for the last brazing operation, all of the brazing of the bellows to the specimen was done in a vacuum using either electron beam welding or induction heating. The final brazing operation was executed in a helium atmosphere at atmospheric pressure (approximately 1 atm.). By this technique the helium was sealed inside the bellows. A vacuum may instead be sealed inside the bellows if desired; however, a vacuum did not transfer the heat produced in the bellows and resulted in slower heating times (by a factor of three). To determine the temperature of the specimen's gage length, a type K thermocouple with an Inconel sheath was attached in the middle of the gage section with a thin metal strip and brazed in place at the junction between the bellows and the specimen. The thermocouple can be seen coming out of the end of the bellows in Fig. 3.

The induction coil used in the testing consisted of two symmetric coils with inner and outer wraps. The coils were concentrated over the Inconel tubes of the bellows and were adjusted to minimize the temperature gradients in the 1 inch gage section of the specimen.

The strain was read using a 2.5 inch extensometer utilizing quartz rods positioned on the specimen outside the bellows. Since it was desired to control the strain of the 1 inch gage section, a calibration was performed to determine the equivalent displacement of the 2.5 inch extensometer for a given displacement of the 1 inch extensometer. Realizing that only the gage section is heated in the induction heating, it was necessary to repeat this calibration for each different temperature and strain range for the isothermal tests, and each of the various temperature ranges for the out-of-phase and in-phase TMF tests. Air tests (without bellows) were performed using the 2.5 inch extensometer to determine the accuracy of this calibration. The fatigue lives in air using the 2.5 inch extensometer compared favorably with the 1 inch extensometer data.

The results indicate that the increase in life from air to helium is dependent on the testing parameters. For isothermal fatigue the increase in life ranged from 2 to 12 times. This factor increased as the strain range decreased, indicating that oxidation is more detrimental at low strain ranges. For out-of-phase TMF the increase in life ranged from a factor of 2 to 5. However, for in-phase TMF the increase in life only ranged from 1.3 to 2, indicating that oxidation is a smaller contributing damage factor in this case.

### 1.4.2 Interrupted Experiments

To gain insight in the progression of damage in laboratory tests under different phasing conditions, interrupted tests in air were performed. These tests involved using a number of specimens for each test condition and stopping each one at some percentage of life (e.g., 10% $N_f$, 20% $N_f$, 40% $N_f$, 60% $N_f$, 80% $N_f$, and 100% $N_f$ were used). Each specimen in these tests was sectioned and then examined to detect microscopic damage. In particular, the oxide characteristics and oxide intrusion growth were examined. Also, the progress of internal creep damage along grain boundaries was revealed. The specific tests used in this study were

- Isothermal fatigue, Air, T = 600°C, $\Delta\varepsilon_{mech} = 0.0070$, $\dot{\varepsilon} = 0.0002\ sec^{-1}$, $N_f = 700$.
- Out-of-phase, total constraint TMF, Air, T = 150-600°C, $\Delta\varepsilon_{mech} = 0.0076$, $\dot{\varepsilon} \approx 0.0001\ sec^{-1}$, $N_f = 735$.
- In-phase TMF, Air, T = 150-600°C, $\Delta\varepsilon_{mech} = 0.0076$, $\dot{\varepsilon} \approx 0.0001\ sec^{-1}$, $N_f = 220$.

These tests can be readily compared since all three tests have similar strain ranges and strain rates, and the isothermal test was performed at the maximum temperature of the TMF cycle. Moreover, the comparisons among these tests can be attributed mostly to the strain-temperature phasing, since all other parameters are about the same.

### 1.4.3 Microscopy

After testing, specimens were sectioned longitudinally through the primary crack origin using a low speed saw, and then mounted in an epoxy so that the oxide would remain intact. The mounted specimens were polished with successively finer grades of abrasive paper, 6 μm and 1 μm diamond paste, and 0.05 μm alumina powder. A 5% Nital etch was used to disclose the microstructure. Scanning electron microscope (SEM) photographs illustrating the representative surface oxide and oxide "intrusions" for the three phasings considered are shown in Fig. 4. These microphotographs in Fig. 4 were taken at the same magnification at 80% $N_f$ for each phasing. The metal has been etched to show the grain structure. The oxide "intrusions" in isothermal fatigue and out-of-phase TMF are transgranular. Note that no oxide intrusions formed in the in-phase TMF case. In this case most of the damage is in the form of internal intergranular cracking at the pearlite colony boundaries perpendicular to the loading direction as shown in Fig. 5. These intergranular cracks are similar to the intergranular damage observed in a stress-hold creep test at 600°C, which is also shown in Fig. 5 for comparison.

In addition to the interrupted tests, the post-failure oxide characteristics from most of the other fatigue-life tests performed on 1070 steel were examined. Measurements of surface oxides, oxide-filled intrusions, and cracks were obtained from these SEM microphotographs. From these extensive examinations, a mechanistic model for oxidation-induced growth will be proposed.

# 2. LIFE PREDICTION METHODOLOGY

## 2.1 Damage Mechanisms

The proposed life prediction methodology considers the fatigue, creep, and environmental damage which can be experienced by a component. It is applicable to strain-temperature histories with isothermal loading as a special case. Mechanical strain range, strain rate, temperature, and the phasing of the temperature and the mechanical strain dictate the damage induced in the material. The life prediction model is configured to incorporate these variables.

Because this is such a complex problem, a few simplifying assumptions need to be made before proceeding. First, consider that three possible damage mechanisms exist: (1) fatigue, (2) environmental attack (oxidation), and (3) creep. Depending on the temperature, strain, and phasing all three of these damage mechanisms could be operating. If the temperature is too low for significant oxidation and creep, then the fatigue damage mechanism will control the life. In an out-of-phase TMF test on the material considered (in which the maximum temperature occurs at a compressive stress), oxidation damage can be significant, while creep damage is negligible since void growth and intergranular cracking mechanisms are suppressed in compression. In this case the life will be governed by the oxidation damage mechanism.

In the model the damage per cycle from these three mechanisms are summed to obtain a total damage per cycle, $D^{tot}$,

$$D^{tot} = D^{fat} + D^{ox} + D^{creep} \tag{2.1}$$

where the superscripts *fat*, *ox*, and *creep* represent fatigue, oxidation, and creep, respectively. Without prior knowledge of the most damaging mechanisms for a given strain-temperature history, this equation will predict the total damage.

Equation 2.1 may be rewritten in terms of the failure life, $N_f$, since damage is equal to $1/N_f$ (assuming linear damage and damage is equal to 1 at failure),

$$\frac{1}{N_f} = \frac{1}{N_f^{fat}} + \frac{1}{N_f^{ox}} + \frac{1}{N_f^{creep}} \tag{2.2}$$

The discussion of these damage terms follows. The fatigue damage term is represented by the strain-life equation [47] and is discussed in the next section. The discussion and development of the oxidation and creep damage terms is more involved and is each considered in a separate chapter. The model constants will be described for 1070 steel, but the model would be applicable to other materials.

## 2.2 Fatigue Damage Term

Fatigue damage is represented by classical fatigue mechanisms which normally occur at ambient temperatures. These include to-and-fro slip of dislocations and the formation of a crack. Crack growth occurs by localized deformation and slip in the cyclic plastic zone ahead of the crack tip. Most of the tests in this study are performed at elevated temperatures where many variables (strain range, strain rate, temperature, and strain-temperature phasing) may affect the life. However, the "fatigue" mechanism (involving crack nucleation and early crack growth) is assumed to be governed by mechanical strain range, $\Delta\varepsilon_{mech}$. Plastic strain range component of $\Delta\varepsilon_{mech}$ may also be utilized; however, for many loading conditions including thermal loading, its determination requires further calculations. The use of total strain range is simpler and equally relevant as plastic strain range.

The fatigue life term, $N_f^{fat}$, is estimated from the strain-life relation [47],

$$\frac{\Delta\varepsilon_{mech}}{2} = \frac{\sigma_f'}{E}\left(2N_f^{fat}\right)^b + \varepsilon_f'\left(2N_f^{fat}\right)^c \tag{2.3}$$

where

E is Young's modulus,

$\sigma_f'$ is the fatigue strength coefficient,

b is the fatigue strength exponent,

$\varepsilon_f'$ is the fatigue ductility coefficient, and

c is the fatigue ductility exponent.

The constants are determined from isothermal room temperature fatigue tests and are given in Ref. [46]. In Fig. 6, the room temperature (20°C) isothermal strain-life curve for 1070 steel is shown along with other 1070 steel data which would also be expected to have a life based solely on $N_f^{fat}$. These include isothermal tests performed at or below 400°C, where little or no oxidation and creep occur, and 600°C isothermal helium tests performed at a high strain rate ($\dot{\varepsilon} = 0.02$ sec$^{-1}$), which eliminates oxidation effects and minimizes creep effects.

The room temperature strain-life curve can be considered an upper bound on life. The lives of all tests performed with this material were found to be less than or approximately equal to the room temperature tests. Any decrease in life can be attributed to $D^{ox}$, $D^{creep}$, or both.

In cases where crack growth outside the size of the specimen has to be considered, the fatigue life includes a long crack propagation period which is determined using fracture mechanics or modified fracture mechanics parameters [8,9,31]. Crack growth experiments would result in determination of $N_f^P$, long crack propagation life. Then

$$N_f^{tot} = N_f + N_f^P \tag{2.4}$$

where $N_f$ is determined by the proposed model and $N_f^{tot}$ represents both specimen life (initiation and crack growth to a certain size) and long crack propagation life.

# 3. DEVELOPMENT OF THE OXIDATION DAMAGE TERM

## 3.1 Oxidation-Induced Crack Growth Model

The oxidation damage is based on measurements of surface and crack tip oxidation kinetics and repeated rupture of oxide. A thorough scanning electron microscope (SEM) study of the surface oxide and oxide "intrusion" characteristics for most of the laboratory tests was performed. As an outgrowth from this SEM study, a damage model is proposed which reflects the oxidation-induced crack nucleation and growth as observed in the microphotographs. Oxidation-induced crack growth is described as the repeated formation of an oxide layer at the crack tip and its rupture, exposing fresh metallic material to the environment. "Crack nucleation" is defined as the rupture of the first oxide layer formed.

### 3.1.1 Type I Growth

The formation of an oxide intrusion by the process of oxide rupture is illustrated by Fig. 7. Initially, an oxide layer forms on the surface (a). When this oxide layer reaches a critical thickness, $h_{f1}$, the oxide ruptures and "crack nucleation" has occurred (b). Then fresh metallic surface is exposed to the environment which rapidly oxidizes (c). When the thickness of this newly formed oxide reaches $h_{f2}$, the oxide again ruptures (d). The process continues as shown in (e)-(f). Note that the critical thickness when rupture occurs does not have to be constant but may change with applied strain range, strain rate, and temperature.

Type I growth is characterized by a "continuous" oxide layer. "Continuous" oxide layer results in oxide intrusions with no visible stratification in the oxide. This will be distinguished from Type II growth which is characterized by "multi-layer" or "stratified" oxide growth, which has been observed by other researchers [11,45,46,48,49].

### 3.1.2 Type II Growth

A schematic illustrating Type II growth is given in Fig. 8. It is important to note that the progression of growth is similar to Type I in that the oxide ruptures when it reaches some critical layer thickness, $h_{fi}$. However, when the oxide ruptures in Type II growth, it also detaches from the surface. This results in exposing a larger fresh surface area to the environment, accounting for the wider intrusions characteristically observed with Type II growth [46]. A representative example of each type of growth is shown in Fig. 9 (magnification of tips in Figs. 4b and 4a, respectively). Note that the oxide stratifications are visible in Type II; therefore, a direct measure of $h_{fi}$ can be obtained. This is illustrated in Fig. 10.

## 3.2 Derivation of the Oxidation Damage Term

The methodology of the oxidation-induced crack growth model is now discussed. The model is general and is applicable to both Type I and Type II oxide rupture mechanisms. An equation is first derived to obtain the oxidation-induced crack growth per cycle, $dh_o/dN$, where $h_o$ is defined in Fig. 11 as the sum of the surface oxide thickness, $h_s$, and the oxide intrusion depth, $h_i$, components. First, $dh_o/dN$ is separated into two factors by the chain rule,

$$\frac{dh_o}{dN} = \frac{dh_o}{dt} \cdot \frac{dt}{dN} \tag{3.1}$$

so that the crack growth rate per unit time, $dh_o/dt$, is obtained, which is required in the subsequent derivation. In Eq. 3.1, $dt/dN$ is the cycle period, $t_c$,

$$\frac{dh_o}{dN} = \frac{dh_o}{dt} \cdot t_c \tag{3.2}$$

The factor $dh_o/dt$ can be considered as an effective oxide growth rate of the primary oxidation-induced crack. This factor can be defined by the oxidation kinetics and the critical oxide layer thickness at rupture, $h_f$. If an oxide layer does not rupture, the model assumes oxidation follows some oxidation growth law. In 1070 steel oxidation follows parabolic growth [50], but other oxidation growth laws may be used depending on the material. The parabolic growth law is given as:

$$h_o = \sqrt{K_p t} \tag{3.3}$$

where $K_p$ is the parabolic oxidation constant which is a function of temperature. The time, t, is measured from the instant when fresh metal surface is exposed to the environment.

In general, $K_p$ will not be constant for a cycle which undergoes a varying temperature history. Therefore, an effective oxidation constant, $K_p^{eff}$, is defined as

$$K_p^{eff} = \frac{1}{t_c}\int_0^{t_c} D_o \exp\left(\frac{-Q}{RT(t)}\right)dt \tag{3.4}$$

where

$D_o$ is the diffusion coefficient,

Q is the activation energy for oxidation,

R is the gas constant,

T(t) is the temperature, which can vary with time, and

$t_c$ is the period of the cycle.

Subsequently, $K_p^{eff}$ will be used in the derivation.

If the oxide repeatedly ruptures, then the oxidation growth no longer follows the parabolic law. At the locality of rupture, where fresh metal is exposed to the environment, oxidation once again follows a parabolic growth law as if no previous oxidation has occurred. This results in a higher localized oxidation rate and is illustrated in Fig. 12 as a

series of parabolic curves on top of one another with the vertex of the upper parabolic curve located at the point on the one below it where rupture of oxide occurs. Connecting these vertex points creates the effective total oxide growth curve. The slope of this curve gives the effective growth rate, $dh_o/dt$. The equation of this curve is

$$h_o = B \frac{K_p^{eff}}{\bar{h}_f} t^{\beta} \tag{3.5}$$

where $\bar{h}_f$ is an average value of the critical oxide thickness at rupture, and B and $\beta$ are constants. For the case of linear (versus parabolic) oxide growth, $B = \beta = 1$ and $\bar{h}_f = h_{f1}$ = constant, and $dh_o/dt$ = constant. In general, though, the effective growth is non-linear and will increase with time as shown in Fig. 12 since $h_{fi+1} < h_{fi}$. This occurs due to the increase in the mechanical strain range at the oxide intrusion tip as the intrusion grows. Similarly, increasing the applied mechanical strain range results in decreasing the rupturing thickness of the oxide, $h_{fi}$, as will be illustrated later. The growth rate $dh_o/dt$ has been measured in laboratory tests and has a similar shape to the schematic of Fig. 13. As shown in Fig. 13, the crack length versus cycles curves from all three interrupted tests show power law growth (linear on log-log plot) up to a certain crack size. Beyond this crack size rapid crack propagation takes place and the oxidation effect becomes small. Note that the oxidation-induced crack growth does not operate in the in-phase TMF case. Comparing the in-phase case to out-of-phase TMF and isothermal fatigue, the crack growth rate during the initial portion of life is low. Intergranular damage rapidly accumulates and results in rapid damage in the latter part of life.

Differentiating Eq. 3.5 with respect to time and substituting this equation back into (3.2) gives

$$\frac{dh_o}{dN} = B \frac{K_p^{eff}}{\bar{h}_f} \beta t^{\beta-1} \cdot t_c \tag{3.6}$$

where t is the test duration and can be replaced with $N \cdot t_c$, the number of cycles, N, multiplied by the period of each cycle, $t_c$,

$$\frac{dh_o}{dN} = B \frac{K_p^{eff}}{\bar{h}_f} \beta N^{\beta-1} \cdot t_c^{\beta} \tag{3.7}$$

The average critical oxide thickness at rupture, $\bar{h}_f$, is a function of the mechanical strain range, the phasing of the temperature and mechanical strains, and the strain rate. Experimental measurement of $\bar{h}_f$ (direct measurement of the stratified oxide layer thickness in the oxide intrusions) is plotted against the mechanical strain range, $\Delta\varepsilon_{mech}$, for three different phasing conditions in Fig. 14. These results are for 1070 steel studied here. The experimental results are indicated by data points. Based on the data points, curves relating $\Delta\varepsilon_{mech}$, the phasing, $\Phi^{ox}$, and the strain rate, $\dot{\varepsilon}$, can be expressed by

$$\bar{h}_f = \frac{\delta_o}{(\Delta\varepsilon_{mech})^2 \, \Phi^{ox} \, \dot{\varepsilon}^a} \tag{3.8}$$

where the exponent 2 on $\Delta\varepsilon_{mech}$ represents the slope of the curve in the diagram. The phasing, $\Phi^{ox}$, is a function of the ratio of the thermal and mechanical strain rates. It ranges in value from 0 which indicates that no environmental damage results from the phasing to 1 which indicates that the coupling of the environment and phasing are most detrimental to the life. The material constants, $\delta_o$ and a, may be estimated from the plot in Fig. 14. The constant, a, predicts the strain rate sensitivity of $\bar{h}_f$, and $\delta_o$ is a measure of oxide ductility, which is equivalent to $\bar{h}_f$ when $\Delta\varepsilon_{mech}$, $\Phi^{ox}$, and $\dot{\varepsilon}$ are unity, and can be determined from Fig. 14.

Substituting (3.8) into (3.7) gives

$$\frac{dh_o}{dN} = \frac{B \, (\Delta\varepsilon_{mech})^2 \, \Phi^{ox} \, \dot{\varepsilon}^a \, K_p^{eff} \, \beta N^{\beta-1} \, t_c^{\beta}}{\delta_o} \tag{3.9}$$

The crack is assumed to grow from 0 to some critical length, $h_{cr}$. This represents the oxidation-induced crack growth. This behavior ends when $h_o = h_{cr}$ and then crack begins to grow rapidly and oxide penetration trails behind the crack tip. Fracture mechanics parameters would characterize crack growth beyond $h_{cr}$. Integrating N from 0 to $N_f^{ox}$ and solving for $N_f^{ox}$,

$$N_f^{ox} = \left[ \frac{h_{cr}\, \delta_o}{B\, (\Delta\varepsilon_{mech})^2\, \Phi^{ox}\, \dot{\varepsilon}^a\, K_p^{eff}} \right]^{\beta^{-1}} \frac{1}{t_c} \tag{3.10}$$

Since the time of a cycle for continuous cycling can be written in terms of the mechanical strain range and the strain rate by

$$t_c = \frac{2\, \Delta\varepsilon_{mech}}{\dot{\varepsilon}} \tag{3.11}$$

Eq. 3.10 can be stated in terms of the strain rate instead of the cycle period,

$$N_f^{ox} = \left[ \frac{h_{cr}\, \delta_o}{B\, \Phi^{ox}\, K_p^{eff}} \right]^{\beta^{-1}} \frac{\dot{\varepsilon}^{\,1-(a/\beta)}}{2(\Delta\varepsilon_{mech})^{(2/\beta)+1}} \tag{3.12}$$

In this equation, the $K_p^{eff}$ term in the denominator accounts for the temperature dependence and is given by Eq. 3.4. The mechanical strain range and the strain rate are directly accounted for in the equation with $\Delta\varepsilon_{mech}$ and $\dot{\varepsilon}$ terms, respectively. The phasing term, $\Phi^{ox}$, accounts for the influence of the temperature-mechanical strain history and is discussed in the next section. For strain-time histories with complex variations, Eq. 3.11 will include additional terms.

3.3 Phasing Factor

Each history is represented by a unique value of $\Phi^{ox}$, defined by integrating $\phi^{ox}$, which is a function of the ratio of $\dot{\varepsilon}_{th}/\dot{\varepsilon}_{mech}$, over the period of the history,

$$\Phi^{ox} = \frac{1}{t_c}\int_0^{t_c} \phi^{ox}\, dt \tag{3.13}$$

The division by $t_c$ allows $\Phi^{ox}$ to range from 0 to 1 and thus represent the effective phasing parameter for any strain-temperature history.

The form of $\phi^{ox}$ was chosen to represent the behavior of the oxide cracking that has been observed experimentally. For example, consider the out-of-phase TMF case: In this case low temperature and high tensile stresses coincide, and consequently the oxide cracks readily. In this case, for a given mechanical strain range, the $\bar{h}_f$ level is small as shown in Fig. 14. If the phasing is represented by the ratio of the thermal and mechanical strain rates, $\dot{\varepsilon}_{th}/\dot{\varepsilon}_{mech} = -1$ represents the out-of-phase TMF case. This case is designated as a benchmark by setting $\phi^{ox} = 1$ at $\dot{\varepsilon}_{th}/\dot{\varepsilon}_{mech} = -1$. For the limiting case of free expansion ($\dot{\varepsilon}_{th}/\dot{\varepsilon}_{mech} \rightarrow \pm\infty$), $\phi^{ox}$ should approach zero. Other histories designated by $\dot{\varepsilon}_{th}/\dot{\varepsilon}_{mech}$ will have unique values of $\phi^{ox}$ which fall between the limits 0 and 1. The level of $\bar{h}_f$ at a given strain range is higher in the in-phase TMF case ($\dot{\varepsilon}_{th}/\dot{\varepsilon}_{mech} = 1$) compared to the isothermal fatigue case ($\dot{\varepsilon}_{th}/\dot{\varepsilon}_{mech} = 0$) as indicated in Fig. 14.

Based on these observations, the function $\phi^{ox}$ was chosen to be:

$$\phi^{ox} = \exp\left[-\frac{1}{2}\left(\frac{(\dot{\varepsilon}_{th}/\dot{\varepsilon}_{mech}) + 1}{\xi^{ox}}\right)^2\right] \tag{3.14}$$

The parameter $\xi^{ox}$ is introduced as a measure of the relative amount of damage associated with the different phasings. This exponential function is plotted in Fig. 15 for several $\xi^{ox}$ values. In this case the curves show that peak damage occurs when $\dot{\varepsilon}_{th}/\dot{\varepsilon}_{mech} = -1$ (out-of-phase TMF, total constraint).

3.4 Determination of the Constants

In this section it is shown how each constant in the oxidation damage term is established.

$\xi^{ox}$: Consider two tests which have different strain-temperature phasings, and $N_f^{ox}$ dominates the damage sum. One of these tests is an out-of-phase TMF since $\phi^{ox}$ is assumed to be 1 for this case. The $\dot{\varepsilon}$, $\Delta\varepsilon_{mech}$, and $K_p^{eff}$ should be approximately the same for both cases. $N_f^{ox}$ is known for both cases. Therefore, only $\phi_2^{ox}$ (subscripts distinguish between the two tests) for the second test is unknown and can be solved for by rearranging Eq. 3.12,

$$\phi_2^{ox} = \phi_1^{ox}\left(\frac{N_{f_1}^{ox}}{N_{f_2}^{ox}}\right)^{\beta}\left(\frac{K_{p_1}^{eff}}{K_{p_2}^{eff}}\right)\left(\frac{\dot{\varepsilon}_2}{\dot{\varepsilon}_1}\right)^{\beta-a}\left(\frac{\Delta\varepsilon_{mech_1}}{\Delta\varepsilon_{mech_2}}\right)^{2+\beta} \tag{3.15}$$

By substituting this value of $\phi_2^{ox}$ into Eq. 3.14, $\xi^{ox}$ can be determined. The two tests used were

- (1) Out-of-phase TMF, T = 150-600°C, $\Delta\varepsilon_{mech1} = 0.0076$, $\dot{\varepsilon}_1 \approx 0.0001$ $sec^{-1}$, $N_{f1}^{ox} \approx 735$, $\phi_1^{ox} = 1$.
- (2) Isothermal fatigue, T = 600°C, $\Delta\varepsilon_{mech2} = 0.0070$, $\dot{\varepsilon}_2 = 0.0002$ $sec^{-1}$, $N_{f2}^{ox} \approx 700$.

Based on the above analysis, $\phi_2^{ox} = 0.88$ and $\xi^{ox} \approx 2$ The function $\phi^{ox}$ using this value has been shown in Fig. 15.

a: Consider two isothermal fatigue experiments at strain rates $\dot{\varepsilon}_1 = 0.0002$ $sec^{-1}$ and $\dot{\varepsilon}_2 = 0.02$ $sec^{-1}$. From Fig. 14 one can determine from the isothermal case the corresponding $\bar{h}_f$ values for both of these strain rates at a constant $\Delta\varepsilon_{mech}$. Then,

$$a = \frac{\ln(\bar{h}_{f_1}/\bar{h}_{f_2})}{\ln(\dot{\varepsilon}_2/\dot{\varepsilon}_1)} \tag{3.16}$$

$\delta_o$: This material constant represents the value of the $\bar{h}_f$-axis intercept at $\Delta\varepsilon_{mech} = 1$ when $\Phi^{ox}$ and $\dot{\varepsilon}$ are also unity. One laboratory test which has a multi-layered oxide (Type II growth behavior) is required to obtain this constant:

- Isothermal fatigue, T = 600°C, $\Delta\varepsilon_{mech} = 0.01$, $\dot{\varepsilon} = 0.0002\ sec^{-1}$, $\bar{h}_f \approx 1.5\ \mu m$, $\Phi^{ox} = 0.88$.

By solving for $\delta_o$ in Eq. 3.8,

$$\delta_o = \bar{h}_f (\Delta\varepsilon_{mech})^2 \Phi^{ox} \dot{\varepsilon}^a \tag{3.17}$$

and then substituting the above test parameters, the constant, $\delta_o$, was determined. In this study $\delta_o$ was found to be $2.22 \times 10^{-7}\ \mu m \cdot sec^{-0.75}$. The value of $\bar{h}_f$ is the average value of $h_{fi}$ measured from microphotographs, such as shown in Fig. 10.

$D_o$ and Q: $D_o$ is the diffusion coefficient and Q is the activation energy for oxidation. They were established from oxide growth measurements on specimens subjected to zero load. Two temperatures were considered to obtain the constants: 600°C and 400°C. The parabolic growth constant, $K_p$, was determined at both of these temperatures by fitting a parabolic curve through the experimental data. Since

$$K_p = D_o e^{(-Q/RT)} \tag{3.18}$$

$D_o$ and Q can be calculated. In Fig. 16, the growth curves for various temperatures as established from Eq. 3.18 are plotted along with the laboratory data used to obtain the constants.

$\beta$: This constant is the exponent on t for the effective oxidation-induced growth curve (Fig. 12). It was chosen to represent the crack growth behavior observed in laboratory tests (Fig. 13). Experimental results indicate an average value of $\beta = 1.5$.

B, $h_{cr}$: These two constants are interrelated. The units on B are ($sec^{1-\beta}$) (see Eq. 3.5) and the units on $h_{cr}$ are ($\mu m$). Consider a test which is used to obtain the critical crack length, $h_{cr}$. There is a corresponding time to reach this length and B is related to this time. Using the life and cycle time from this test, the constant B is obtained by:

$$B = \left(t_c \cdot N_f^{ox}\right)^{1-\beta} \tag{3.19}$$

In this study, the following test was used:

- Isothermal fatigue, T = 600°C, $\Delta\varepsilon_{mech} = 0.01$, $\dot{\varepsilon} = 0.0002\ sec^{-1}$, $N_f = 228$.

The value of $h_{cr}$ was determined from Eq. 3.12 where $N_f^{ox}$, the test parameters ($\Delta\varepsilon_{mech}$, $\dot{\varepsilon}$), and other constants for the same experiment used to compute B are known.

# 4. DEVELOPMENT OF THE CREEP DAMAGE TERM

## 4.1 Measure of Creep Damage

Physical measures of creep damage were sought for by examining tested specimens with the SEM. Most creep damage, which is detectable with the SEM, is in the form of internal intergranular cracking (e.g., see Fig. 17). This damage was only observed in the in-phase TMF test specimens. None of the isothermal or out-of-phase TMF tests had any detectable intergranular damage.

The in-phase TMF 150-600°C test was one of the tests considered in the interrupted study. It was found that below 60% $N_f$, no creep damage in the form of intergranular cracking (greater than 0.10 μm) was observed. At 60% $N_f$, a few small (less than 1.0 μm) cavities along grain boundaries were detected. Significant measurable damage was not found until 100% $N_f$ was reached.

These interrupted tests presented a dilemma. It is desired that a creep damage term represent some physically measurable damage, but there is none detectable for most of the life. Therefore, the macroscopic (bulk) parameters which are causing the void formation, and then subsequent void growth and intergranular cracking, were used.

Creep damage can be considered as an asymmetric problem with respect to tensile and compressive loading. The damage occurring under the tensile loading usually is different from compressive loading [51]. Considering the physical damage, the void growth and intergranular cracking mechanisms are suppressed under compressive loading. However, other creep mechanisms operate both in compression and tension. These include grain boundary sliding, grain boundary diffusion, lattice diffusion, and dislocation creep. Voids are initiated at grain boundaries by the operation of these mechanisms under either tension or compression loadings. But, the growth of voids and intergranular crack growth occur predominantly under tensile loading [35,52]. Consequently, to take into account the

asymmetry, the creep damage term is a function of effective and hydrostatic stress components:

$$D^{creep} = \int_0^{t_c} A\, e^{(-\Delta H/RT)} \left( \frac{\alpha_1 \bar{\sigma} + \alpha_2 \sigma_H}{K} \right)^m dt \qquad (4.1)$$

where

$\Delta H$ is the activation energy for the rate-controlling creep mechanism,

R is the gas constant,

T is the temperature,

$\bar{\sigma}$ is the effective stress,

$\sigma_H$ is the hydrostatic stress,

K is the drag stress,

$\alpha_1$ and $\alpha_2$ are scaling factors which represent the relative amount of damage occurring in tension and compression, and

A, m are material constants.

In order to use this equation, a constitutive model must be employed which can relate the known strains to the stresses. This is necessary to handle different strain rates, thermo-mechanical loadings, and hold-time effects.

For the predictions in this report a unified constitutive model recently developed for 1070 steel [53,54] is used. This model utilizes two state variables: (1) The drag stress, K, which is a measure of strength and (2) back stress, $\alpha$, which is recognized as an internal stress reflecting the non-isotropy in the material. In creep the back stress, $\alpha$, accounts for non-isotropy as well as transient creep behavior. Since it is desirable to obtain the creep damage for the stable cycle, a simplification is made in the constitutive model so that the approximate stable response can be directly obtained, bypassing any initial transient behavior. This is accomplished by setting the drag stress to the saturated value, $K = K_{sat}$,

where $K_{sat}$ is a function of the temperature, and set the back stress to zero, $\alpha = 0$. Under stress relaxation conditions, the back stress tends to zero.

In the absence of the drag stress, K, in the creep damage term (Eq. 4.1) may result in inconsistent predictions as described below. Consider three isothermal tests performed each at an increasingly higher temperature. The creep damage would be expected to increase as the temperature increases. If the strain rate is constant among these three tests, then there are two remaining factors in Eq. 4.1 which contribute to the damage: the exponential factor involving temperature and the stress. The temperature factor correctly increases as the temperature increases; however, because the yield stress of this material decreases as temperature increases, the stress factor decreases. If this stress factor decreases faster than the temperature factor increases the damage, then the model will predict more creep damage at the lower temperatures. This is contrary to reason. Therefore, it was recognized that creep damage is a function of the instantaneous stress relative to the instantaneous drag stress.

Consider a uniaxial loading example where all the creep damage is assumed to occur in tension. If $\alpha_1 = 1/3$ and $\alpha_2 = 1$ are chosen, then Eq. 4.1 implies that no damage occurs under compressive loading and only tensile loads result in any accumulation of damage with $D^{creep}$ given by

$$D^{creep} = \int_0^{t_c} A\, e^{(-\Delta H/RT)} \left(\frac{2}{3}\frac{\sigma_x}{K}\right)^m dt \qquad (4.2)$$

## 4.2 Creep Damage under Different Phasing Conditions

Consider the following dilemma comparing the experimental creep lives and microstructural damage observations to the predicted creep lives using Eq. 4.1 for the two tests below:

- In-Phase TMF, T =150-600°C, $\Delta\varepsilon_{mech} = 0.0076$, $\dot{\varepsilon} \approx 0.0001$ $sec^{-1}$, Experimental $N_f^{creep} \approx 432$.
- Isothermal Fatigue, T = 600°C, $\Delta\varepsilon_{mech} = 0.0070$, $\dot{\varepsilon} = 0.0002$ $sec^{-1}$, Experimental $N_f^{creep} \approx 10{,}000$.

As the model stands up to this point, it does not distinguish between the effect of the phasing on the creep damage. It predicts that the creep damage is about the same in both cases. This arises because the three independent variables (i.e., T, $\sigma$, and $t_c$) in the creep damage term (Eq. 4.1) are nearly the same in both of these tests.

However, both from experimental observation as well as experimental $N_f^{creep}$ values, this is clearly not accurate. For all in-phase TMF tests, including the lowest temperature range test performed (150-450°C), internal intergranular cracking is observed, which results from the growth of voids and subsequent intergranular creep damage. In all isothermal test specimens (fully reversed loading and symmetric wave form), no intergranular damage is observed and all cracking is transgranular. This indicates that different damage mechanisms are operating in each of these tests. This must be reflected in the creep damage equation.

A phasing factor, $\Phi^{creep}$, similar to the one used in the oxidation damage term is incorporated into the creep damage term. The phasing factor for creep will have the same form (Eqs. 3.14 and 3.15) as the $\Phi^{ox}$ factor for oxidation. For example, assume

$$\Phi^{creep} = \frac{1}{t_c}\int_0^{t_c} \phi^{creep}\, dt \tag{4.3}$$

where $t_c$ is the cycle time and $\phi^{creep}$ is an exponential function of $\dot{\varepsilon}_{th}/\dot{\varepsilon}_{mech}$ characterizing the severity of the creep damage for any ratio of the thermal and mechanical strain rates. This function is represented by a normal distribution for which the peak ($\phi^{creep} = 1$) occurs where the phasing of the thermal and mechanical strain rates is most damaging,

$$\phi^{creep} = \exp\left[-\frac{1}{2}\left(\frac{(\dot{\varepsilon}_{thr}/\dot{\varepsilon}_{mech}) - 1}{\xi^{creep}}\right)^2\right] \tag{4.4}$$

The constant, $\xi^{creep}$, defines the sensitivity of the phasing is to the creep damage. This function is shown plotted in Fig. 18. From laboratory tests the in-phase TMF case ($\dot{\varepsilon}_{thr}/\dot{\varepsilon}_{mech} = 1$) shows the most creep damage (creep voids and intergranular cracking); therefore, this case is assigned the value $\phi^{creep} = 1$ as shown in Fig. 18, which is a plot of Eq. 4.4. By comparing the $N_f^{creep}$ experimental values for two different phasings, an assessment of the sensitivity to the phasing, and thus, $\xi^{creep}$, can be obtained. Based on the two tests given at the beginning of this section, $\xi^{creep} \approx 0.40$. The distribution of $\phi^{creep}$ shown in Fig. 18 is for this value. Substituting Eq. 4.4 into Eq. 4.3, then multiplying Eq. 4.3 to Eq. 4.1 gives the final form of the creep damage term,

$$D^{creep} = \frac{1}{t_c}\int_0^{t_c} \exp\left[-\frac{1}{2}\left(\frac{(\dot{\varepsilon}_{thr}/\dot{\varepsilon}_{mech}) - 1}{\xi^{creep}}\right)^2\right] Ae^{(-\Delta H/RT)}\left(\frac{\alpha_1\bar{\sigma} + \alpha_2\sigma_H}{K}\right)^m dt \tag{4.5}$$

4.3 Determination of the Constants

$\alpha_1$, $\alpha_2$: First, $\alpha_1$ and $\alpha_2$ are determined. These constants are included in the model because of the recognition that the microstructural creep damage in tension differs from compression. If it is assumed that no creep damage accumulates in compression (as assumed in 1070 steel), $\alpha_1 = 1/3$ and $\alpha_2 = 1$ for uniaxial loading.

$\Delta H$: The activation energy for creep, $\Delta H$, is experimentally determined from creep tests. The value of $\Delta H$ is 248.1 kJ/mol for 1070 steel [38].

A, m: These constants are interrelated and must be determined in a systematic fashion. By substituting two laboratory test results each into Eq. 4.5, two equations and two unknown constants can be obtained. However, Eq. 4.5 requires that the experimental

value for $N_f^{creep}$ be used. It can be estimated by rearranging Eq. 2.2, and using the experimental life, $N_f^{exp}$, instead of $N_f$,

$$\frac{1}{N_f^{creep}} = \frac{1}{N_f^{exp}} - \frac{1}{N_f^{fat}} - \frac{1}{N_f^{ox}} \tag{4.6}$$

The following two tests were used to obtain these constants:

- Isothermal fatigue, Helium, T = 600°C, $\Delta\varepsilon_{mech} = 0.0030$, $\dot{\varepsilon} = 0.0002\ sec^{-1}$, $N_f^{exp} = 60{,}914$, $N_f^{fat} = 440{,}683$.
- Isothermal fatigue, Helium, T = 600°C, $\Delta\varepsilon_{mech} = 0.0030$, $\dot{\varepsilon} = 0.02\ sec^{-1}$, $N_f^{exp} = 250{,}000$, $N_f^{fat} = 440{,}683$.

By using helium tests, the last term of Eq. 4.6 is eliminated ($1/N_f^{ox} \rightarrow 0$). The $N_f^{fat}$ contribution is determined from the strain-life equation (Eq. 2.3).

The life of the lower strain rate helium test is much less than the high strain rate test indicating that non-environmental time-dependent mechanisms must be producing damage. Therefore, it is valid to use these two tests to estimate the creep damage constants A and m.

# 5. RESULTS

## 5.1 Summary of the Prediction Model

A summary of the prediction model is now given. The total fatigue life, $N_f$, is given by

$$\frac{1}{N_f} = \frac{1}{N_f^{fat}} + \frac{1}{N_f^{ox}} + \frac{1}{N_f^{creep}} \tag{2.2}$$

where the terms on the right hand side are given as follows.

The fatigue-life term, $N_f^{fat}$, is iteratively determined by

$$\frac{\Delta\varepsilon_{mech}}{2} = \frac{\sigma_f'}{E}\left(2N_f^{fat}\right)^b + \varepsilon_f'\left(2N_f^{fat}\right)^c \tag{2.3}$$

using the fatigue constants determined with isothermal 20°C tests. This equation implies that $N_f^{fat}$ is a function of $\Delta\varepsilon_{mech}$ only.

The oxidation life term, $N_f^{ox}$, is given by

$$N_f^{ox} = \left[\frac{h_{cr}\,\delta_o}{B\,\Phi^{ox}\,K_p^{eff}}\right]^{\beta^{-1}} \frac{\dot{\varepsilon}^{1-(\alpha/\beta)}}{2(\Delta\varepsilon_{mech})^{(2/\beta)+1}} \tag{3.12}$$

where

$$\Phi^{ox} = \frac{1}{t_c}\int_0^{t_c} \exp\left[-\frac{1}{2}\left(\frac{(\dot{\varepsilon}_{th}/\dot{\varepsilon}_{mech}) + 1}{\xi^{ox}}\right)^2\right] dt \tag{3.13}$$

Besides mechanical strain range, other parameters are considered which can contribute to the oxidation damage. These include strain rate, temperature, and phasing of the temperature and strain. In Eq. 3.13, $\Phi^{ox}$ is an effective phasing factor for the cycle being examined.

The creep damage term, which is equal to $1/N_f^{creep}$, is given by

$$D^{creep} = \frac{1}{t_c}\int_0^{t_c} \exp\left[-\frac{1}{2}\left(\frac{(\dot{\varepsilon}_{th}/\dot{\varepsilon}_{mech}) - 1}{\xi^{creep}}\right)^2\right] A e^{(-\Delta H/RT)} \left(\frac{\alpha_1\bar{\sigma} + \alpha_2\sigma_H}{K}\right)^m dt \qquad (4.5)$$

In this expression the creep damage is integrated over a cycle. Factors which contribute to the creep damage are included inside the integral. These include temperature, the normalized stress with drag stress, creep phasing factor (the exponential factor in Eq. 4.7), and time. A condensed list of these equations is given in Table 2. A list of all the constants used in the prediction model is provided in Table 3.

## 5.2 Predictions

The predictions for many testing conditions are plotted as strain-life curves in Figures 19-33. Included on these prediction plots are 1070 steel life data. Some of the data has been reported elsewhere [39,46], but all of the plotted test data has been condensed into Table 4. The tests used to establish the constants are noted in Table 4. Some comments and discussion specific to each prediction figure is now given.

Predictions of isothermal fatigue tests performed at 600°C in air are given in Fig. 19. The lines on this plot indicate the prediction curves at three strain rates used in the testing program. Test data are indicated by symbols. In Table 4 the governing damage mechanism is given for each test along with the predicted life value. The governing damage mechanism is the term in Eq. 2.1 which predicts the most damage for that test. For the tests at 600°C, the governing damage mechanism is oxidation for all cases except two (high strain rate and high strain range), which are governed by the fatigue mechanism. The model correctly predicts that there is little time available for the oxidation damage mechanism to operate in these two test cases.

Predictions and laboratory tests for comparable out-of-phase and in-phase TMF tests are shown on Figs. 20 and 21. For both phasings, $T_{min}$ = 150°C. From Table 4 it

should be noted that when $\Delta\varepsilon_{mech}$ is small (which corresponds to a maximum temperature less than 500°C), the governing damage mechanism is fatigue. As $\Delta\varepsilon_{mech}$ increases (with the corresponding increase in temperature), the mechanism changes to oxidation for out-of-phase TMF and to creep for in-phase TMF. In the case of out-of-phase loading, the oxide experiences tension at the low temperature end of the cycle, while in the case of in-phase loading, the specimen is in tension at the high temperature, resulting in the operation of the void growth and intergranular cracking mechanisms.

Additional isothermal fatigue predictions are given in Figs. 22-25 for temperatures 20°C, 400°C, 500°C, and 700°C. The prediction for 20°C (Fig. 22) degenerates into the strain-life curve given by Eq. 2.3, because neither oxidation nor creep mechanisms operate. At 400°C (Fig. 23) only small mechanical strain ranges show any strain rate dependence on the life. At temperatures below 400°C the isothermal predictions resembles the 20°C strain-life curve. At 500°C (Fig. 24) a significant strain rate effect on life is predicted; unfortunately, there is limited data at this temperature to show that a strain rate effect is observed experimentally at this temperature. Isothermal predictions at 600°C show even more strain rate dependence on life as was shown previously in Fig. 19.

In Fig. 25 the predictions for 700°C are given. The predictions indicate that the life at 700°C will be less than at 600°C. However, the laboratory lives were greater at 700°C than at 600°C for the same strain range. This anomaly could be explained by a number of mechanisms. Excessive recovery in the material and recrystallization at 700°C has been confirmed based on the microstructure [55]. A phase transformation occurs in this steel around 680°C and this causes a volumetric strain decrease [55]. Moreover, the oxidation damage mechanism is predicted by the model to be controlling the life at 700°C. This mechanism assumes that the oxide ruptures at some critical thickness, $h_{fi}$, before crack advancement can proceed. In the model $h_{fi}$ is assumed to be a function of the $\Delta\varepsilon_{mech}$, $\dot{\varepsilon}$, and $\Phi^{ox}$. However, at 700°C the oxide will creep [56], and thus resist cracking.

Therefore, $h_{fi}$ at 700°C is likely to be greater than predicted by the model. Further studies into this issue are needed.

Predictions and experimental test data for other total constraint out-of-phase TMF tests with $T_{min}$ different from 150°C are shown in Figs. 26-28. These confirm that the model works for any general temperature range.

One advantage of this prediction model is its ability to handle tests of any given phasing. Two additional phasings, for which experimental data is available, are partial constraint and over constraint out-of-phase TMF (see Fig. 1). For partial constraint, $\dot{\varepsilon}_{th}/\dot{\varepsilon}_{mech} < -1$. The prediction for the experimental tests performed at $\dot{\varepsilon}_{th}/\dot{\varepsilon}_{mech} \approx -2$ is given in Fig. 29. When $\dot{\varepsilon}_{th}/\dot{\varepsilon}_{mech}$ is between -1 (total constraint, $\Delta\varepsilon_{mech} = \Delta\varepsilon_{th}$) and 0 (isothermal conditions), over constraint conditions exist. The prediction shown in Fig. 30 is for the case $\Delta\varepsilon_{mech} = 2\Delta\varepsilon_{th}$ ($\dot{\varepsilon}_{th}/\dot{\varepsilon}_{mech} = -0.5$). Reasonably good predictions are demonstrated.

Tests in helium are also considered. Isothermal helium tests were performed at 600°C, and out-of-phase and in-phase TMF helium tests were performed with $T_{min} = 150$°C. The predictions and laboratory test data are shown in Figs. 31-33. For isothermal fatigue (Fig. 31), a surprising prediction occurs. The slowest strain rate is predicted to be less damaging than the intermediate strain rate, contrary to all tests performed on this material. Since $D^{ox} = 0$ and $D^{fat}$ = constant at all three strain rates, the problem lies entirely in the computation of $D^{creep}$. The root of this anomaly can be traced back to the flow rule used in the unified constitutive model which determines the stress history required by the creep damage term. The flow rule relates the effective inelastic strain rate to the effective stress, $\bar{\sigma}$, normalized with the drag stress, K [53,54]. When $\bar{\sigma}/K \leq 1.0$, the flow rule is a power law function; when $\bar{\sigma}/K > 1.0$, it is an exponential function. Consequently, as the applied strain rate is decreased, $\bar{\sigma}/K$ decreases and the flow rule changes from an exponential function to a power law function, which shows a much greater decrease in stress with a strain rate change, and damage decreases more rapidly.

In addition, the predictions of isothermal helium tests indicate that as the mechanical strain range is increased, the strain rate dependence decreases. The tests are shorter and thus creep damage is minimal. The laboratory tests performed at the largest $\Delta\varepsilon_{mech}$ have nearly identical lives confirming the trend observed in the prediction.

Out-of-phase and in-phase TMF helium tests were performed and are shown in Figs. 32 and 33. Note that the prediction for the out-of-phase degenerates into the fatigue strain-life curve. For this phasing, $N_f^{creep} \approx 0$ and because the tests were performed in helium, $N_f^{ox} = 0$.

# 6. DISCUSSION

The great advantage of this life prediction model is that it is general. (a) It can handle any arbitrary strain-temperature phasing (in-phase and out-of-phase TMF and others). (b) It works for a wide range of temperatures (20°C to 650°C), strain rates ($\dot{\varepsilon} = 0.02$ - $0.0002$ $sec^{-1}$), mechanical strain ranges ($\Delta\varepsilon_{mech} = 0.0030$ - $0.0200$), and atmospheres (air or inert). (c) The constants are directly linked to experiments. (d) The oxide rupture is accounted for by the temperature, strain rate, and strain dependence. (e) The creep term is stress based and has the capacity for treating compressive stresses as damaging or non-damaging. (f) The creep term is also coupled with a unified constitutive equation that predicts the stresses for a given history.

The fatigue, oxidation, and creep damage terms are derived independently. Thus, the damage mechanism which is the most dominant is determined readily. Oxidation and creep damage terms reported are based on physical damage mechanisms. However, the oxidation term, creep term, and fatigue term are not synergistically coupled. This coupling can be investigated by high strain rate tests that are initiated in air in which both fatigue and oxidation mechanisms operate and then continued in helium in which fatigue alone operates. The high strain rate eliminates creep damage, so that crack nucleation occurs by the oxidation-induced process and its effect on subsequent crack growth in absence of oxidation will result. Nevertheless, the coupling of fatigue with either oxidation or creep is considered to be a second order effect for this material. Other investigations [8] reached a similar conclusion for other materials.

The model is not limited to continuous symmetric wave shape cycling. The oxidation and creep equations (Eqs. 3.13 and 4.7) may be integrated to obtain expressions for other complex wave shapes, including hold-time effects. However, according to the oxidation term, any hold time in isothermal fatigue is not predicted to be damaging. This is explained by the initial assumption for the oxidation damage model that oxidation-induced

growth occurs by a rupturing process in this material. Under a strain or stress hold the oxide is assumed not to rupture. Furthermore, since no rupturing of the oxide occurs under a hold time, the environmental attack will lessen with time, because oxidation kinetics predict a decreasing oxidation rate from the parabolic law as the oxide grows thicker if no rupturing occurs. If the material developed an oxide which fractured with no aid from strain cycling, then hold time would be readily incorporated into the oxidation damage term. Nevertheless, the overall model will predict that the effect of hold times is damaging when creep damage is present. For example, under strain holds when stress relaxation occurs, a creep strain is produced in the cycle. This relaxation is predicted by the constitutive law and the creep damage term is a function of this stress.

Other isothermal wave shapes are supported by this model. Comparing slow-fast (slow tensile $\dot{\varepsilon}$ followed by fast compressive $\dot{\varepsilon}$) and fast-slow wave forms, the creep term will predict more damage in the slow-fast case, which is consistent with experimental observation [27]. The oxidation term does not distinguish between these two wave forms.

Some researchers have considered the coupling of creep and fatigue. Majumdar and Maiya [27] predict cavity growth in tension and sintering of the cavities in compression. For isothermal symmetrical wave form loading, their model predicts no synergistic interaction because the voids that grew in tension, sinter in compression. Only under conditions of hold-time fatigue and slow-fast cycles did any synergistic interaction take place in their model. The model proposed in this paper behaves similarly. For slow-fast and hold-time tests, the creep term will take over and predict additional damage.

Other investigators have considered the interaction of fatigue and oxidation. Challenger [5] assumed in his model that initiation life is the cycles to the first rupture of the surface oxide. In 1070 steel the surface oxide ruptures very early in life--sometimes during the first cycle. Therefore, an oxidation term modelled by a repeated oxide rupture is necessary. In addition, Challenger's model predicts that compression holds are more damaging than tensile when creep damage is negligible. The model proposed in this paper

does not distinguish between tensile and compressive holds in the oxidation term. Challenger used the tensile strain range in the oxide; however, under arbitrary phasings, it is difficult to determine the strain in the oxide. Therefore, simply the mechanical strain range was used, which is readily known. For tensile holds at high temperatures, the creep damage term will predict additional damage.

Other researchers have considered a mechanism whereby cracking generally occurs along oxidized surface-connected grain boundaries. Antolovich et al. [6] considered crack initiation when oxidized surface-connected grain boundaries first ruptured, and Liu and Oshida [9] considered crack growth along an oxidized grain boundary by a repeated micro-rupture of the oxide. In model proposed in this paper transgranular cracking is modelled as a repeated oxide growth and rupture process, whereas intergranular cracking is assumed to result from a creep process. If oxidation-induced growth occurs at grain boundaries, it would be necessary to modify the diffusion constants, which would account for the greater oxide penetration into the material.

In the oxidation term of the proposed model, the crack growth rate is related to frequency by, $dh_o/dN \propto 1/\nu^{0.75}$, where the constants for 1070 steel were used to determine the exponent. Liu and Oshida [9] predicted that the crack growth rate based on a repeated rupture of a grain boundary oxide is proportional to $1/\nu$. Data from many different materials, shown in Ref. [9], indicate that this exponent on $\nu$ can range from 0.5 to 1.0 over the frequency range of 0.001 to 10 cycles/sec. Therefore, the value for the exponent in the proposed oxidation damage model agrees with those exhibited by other materials.

The proposed model can be applied to other phasings not considered in the experimental testing. Other phasings should be performed to verify that the model is valid in these more general strain-temperature histories, which are typical to those experienced by actual components.

Considering the broad range of testing parameters examined, the predictions are quite satisfactory. 84 percent of the predictions are within a factor $\pm 2.5$ of the experimental

life. Moreover, for many of the thermo-mechanical fatigue tests, the scatter in the experimental lives affect the appearance of the accuracy of the model.

# 7. CONCLUSIONS

1. Isothermal fatigue, out-of-phase TMF, and in-phase TMF tests were performed in a helium atmosphere and compared to air results. Bellows with helium environment inside encased the reduced section of the specimen. This technique allowed the same specimen design to be used for all tests and required little modification in experimental techniques. Results indicate that helium lives can be 2 to 12 times greater than their air counterpart.

2. Interrupted tests were performed for three different strain-temperature histories (isothermal fatigue, out-of-phase TMF, and in-phase TMF). The progression of damage was examined using the scanning electron microscope and used to develop a mechanistic life prediction model.

3. A comprehensive life prediction model is proposed which is based on the sum of the fatigue, oxidation, and creep damage components.

4. The fatigue damage is based on the strain-life equation [47] with constants determined at room temperature. This damage expression gives an upper bound on life.

5. The oxidation damage is based on a repeated micro-rupture of the oxide at the oxide "intrusion" tip. This rupture process is a function of mechanical strain range, strain rate, strain-temperature phasing, and oxidation kinetics.

6. The creep damage is based on stress, temperature, strain-temperature phasing, and time. The stress history is determined using a unified constitutive equation.

7. A method to predict the damaging effects of arbitrary strain-temperature phasings is proposed.

Table 1 Chemical Composition of 1070 (Class U Wheel) Steel

Given as percent by weight:

| C | Mn | Si | Cu | Cr | P | S | Ni | Mo |
|---|---|---|---|---|---|---|---|---|
| 0.64 | 0.8 | 0.2 | 0.08 | 0.06 | <0.05 | 0.047 | 0.03 | <0.02 |

Fe
balance

Table 2 Summary of the Life Prediction Model

$$\frac{1}{N_f} = \frac{1}{N_f^{fat}} + \frac{1}{N_f^{ox}} + \frac{1}{N_f^{creep}} \tag{2.2}$$

$N_f^{fat}$ is determined from

$$\frac{\Delta\varepsilon_{mech}}{2} = \frac{\sigma_f'}{E}\left(2N_f^{fat}\right)^b + \varepsilon_f'\left(2N_f^{fat}\right)^c \tag{2.3}$$

$N_f^{ox}$ is determined from

$$N_f^{ox} = \left[\frac{h_{cr}\,\delta_o}{B\,\Phi^{ox}\,K_p^{eff}}\right]^{\beta^{-1}} \frac{\dot{\varepsilon}^{1-(a/\beta)}}{2(\Delta\varepsilon_{mech})^{(2/\beta)+1}} \tag{3.12}$$

where

$$\Phi^{ox} = \frac{1}{t_c}\int_0^{t_c} \exp\left[-\frac{1}{2}\left(\frac{(\dot{\varepsilon}_{th}/\dot{\varepsilon}_{mech}) + 1}{\xi^{ox}}\right)^2\right] dt \tag{3.13}$$

$N_f^{creep}$ is determined from

$$\frac{1}{N_f^{creep}} = \frac{1}{t_c}\int_0^{t_c} \exp\left[-\frac{1}{2}\left(\frac{(\dot{\varepsilon}_{th}/\dot{\varepsilon}_{mech}) - 1}{\xi^{creep}}\right)^2\right] A e^{(-\Delta H/RT)}\left(\frac{\alpha_1\bar{\sigma} + \alpha_2\sigma_H}{K}\right)^m dt \tag{4.5}$$

Table 3 Material Constants for 1070 Steel

Material Constants used in Fatigue Strain-Life Term (20°C):

$E = 200860$ MPa
$\sigma_f' = 958.0$ MPa
$b = -0.093$
$\varepsilon_f' = 0.0996$
$c = -0.464$

Material Constants used in Oxidation Damage Term:

$a = 0.75$
$\beta = 1.5$
$B = 6.62 \times 10^{-3}$ sec$^{-0.5}$
$\delta_o = 2.22 \times 10^{-7}$ μm· sec$^{-0.75}$
$D_o = 6.95 \times 10^{7}$ μm$^2$/sec
$Q = 156.5$ kJ/mol
$h_{cr} = 458.0$ μm
$\xi^{ox} = 2.0$

Material Constants used in Creep Damage Term:

$A = 1.562 \times 10^{14}$ sec$^{-1}$
$m = 11.34$
$\Delta H = 248.1$ kJ/mol
$\xi^{creep} = 0.40$

Simple Constitutive Law to Predict Stresses [53]:

$$\dot{\bar{\varepsilon}}^{in} = A_c \exp[-\Delta H_c/R(T+273)]\ f(\bar{\sigma}/K)$$
$A_c = 4.0 \times 10^{9}$ sec$^{-1}$
$\Delta H_c = 210.6$ kJ/mol

$$f(\bar{\sigma}/K) = \begin{cases} (\bar{\sigma}/K)^{5.4} & \bar{\sigma}/K < 1.0 \\ \exp[(\bar{\sigma}/K)^{8.3} - 1.0] & \bar{\sigma}/K > 1.0 \end{cases}$$

Table 3 (continued)

$K = K_{sat}$ (in this study)

$$K_{sat} = \begin{cases} 256.0 + 1.4 \times 10^{-3} T^2 & T \leq 304°C \\ 568.0 - 0.6T & T > 304°C \end{cases} \text{ (MPa)}$$

Table 4 Test Results and Predictions for 1070 Steel

* Indicates test used to establish constants.

(a) Isothermal Fatigue, T = 20°C, Air

| | | $\Delta\varepsilon_{mech}$ | Experimental $N_f$ | Predicted $N_f$ | Governing Damage Mechanism |
|---|---|---|---|---|---|
| $\dot{\varepsilon} = 0.02\ sec^{-1}$ | | | | | |
| | * | 0.0040 | 55102 | 66840 | fatigue |
| | * | 0.0050 | 24046 | 20080 | fatigue |
| | * | 0.0070 | 5503 | 4454 | fatigue |
| $\dot{\varepsilon} = 0.002\ sec^{-1}$ | | | | | |
| | * | 0.0100 | 2796 | 1197 | fatigue |
| | * | 0.0200 | 84 | 144 | fatigue |

(b) Isothermal Fatigue, T = 400°C, Air

| | | $\Delta\varepsilon_{mech}$ | Experimental $N_f$ | Predicted $N_f$ | Governing Damage Mechanism |
|---|---|---|---|---|---|
| $\dot{\varepsilon} = 0.02\ sec^{-1}$ | | | | | |
| | | 0.0040 | 40354 | 63770 | fatigue |
| | | 0.0050 | 8502 | 19600 | fatigue |
| | * | 0.0070 | 6262 | 4402 | fatigue |
| $\dot{\varepsilon} = 0.002\ sec^{-1}$ | | | | | |
| | | 0.0040 | 19046 | 58000 | fatigue |
| | | 0.0100 | 2323 | 1170 | fatigue |
| | | 0.0200 | 309 | 142 | fatigue |
| $\dot{\varepsilon} = 0.0002\ sec^{-1}$ | | | | | |
| | | 0.0040 | 21000 | 45080 | fatigue |
| | * | 0.0070 | 1474 | 3968 | fatigue |
| | * | 0.0100 | 1370 | 1113 | fatigue |

Table 4 (continued)

(c) Isothermal Fatigue, T = 500°C, Air

| | $\Delta\varepsilon_{mech}$ | Experimental $N_f$ | Predicted $N_f$ | Governing Damage Mechanism |
|---|---|---|---|---|
| $\dot{\varepsilon} = 0.002\ sec^{-1}$ | | | | |
| | 0.0200 | 188 | 123 | fatigue |

(d) Isothermal Fatigue, T = 600°C, Air

| | $\Delta\varepsilon_{mech}$ | Experimental $N_f$ | Predicted $N_f$ | Governing Damage Mechanism |
|---|---|---|---|---|
| $\dot{\varepsilon} = 0.02\ sec^{-1}$ | | | | |
| | 0.0030 | 27166 | 34540 | oxidation |
| | 0.0040 | 7748 | 10980 | oxidation |
| | 0.0050 | 6054 | 5158 | oxidation |
| | 0.0070 | 2631 | 1860 | fatigue |
| | 0.0100 | 1062 | 669 | fatigue |
| $\dot{\varepsilon} = 0.002\ sec^{-1}$ | | | | |
| | 0.0040 | 4190 | 3582 | oxidation |
| | 0.0100 | 822 | 342 | oxidation |
| $\dot{\varepsilon} = 0.0002\ sec^{-1}$ | | | | |
| | 0.0030 | 4980 | 3574 | oxidation |
| | 0.0040 | 1286 | 1780 | oxidation |
| | 0.0070 | 700 | 452 | oxidation |
| | 0.0100 | 228 | 187 | oxidation |

Table 4 (continued)

(e) Isothermal Fatigue, T = 600°C, Helium

| | $\Delta\varepsilon_{mech}$ | Experimental $N_f$ | Predicted $N_f$ | Governing Damage Mechanism |
|---|---|---|---|---|
| $\dot{\varepsilon} = 0.02\ sec^{-1}$ | | | | |
| * | 0.0030 | 250000 | 394600 | fatigue |
| | 0.0070 | 11528 | 2883 | fatigue |
| | 0.0100 | 2446 | 948 | fatigue |
| $\dot{\varepsilon} = 0.0002\ sec^{-1}$ | | | | |
| * | 0.0030 | 60914 | 63930 | creep |
| | 0.0070 | 4874 | 3284 | fatigue |
| | 0.0100 | 2467 | 1036 | fatigue |

(f) Isothermal Fatigue, T = 700°C, Air

| | $\Delta\varepsilon_{mech}$ | Experimental $N_f$ | Predicted $N_f$ | Governing Damage Mechanism |
|---|---|---|---|---|
| $\dot{\varepsilon} = 0.02\ sec^{-1}$ | | | | |
| | 0.0030 | 21486 | 5311 | oxidation |
| | 0.0040 | 9633 | 2102 | oxidation |
| | 0.0070 | 5629 | 556 | oxidation |
| $\dot{\varepsilon} = 0.002\ sec^{-1}$ | | | | |
| | 0.0070 | 2392 | 340 | oxidation |
| | 0.0100 | 942 | 142 | oxidation |
| | 0.0200 | 283 | 26 | oxidation |
| $\dot{\varepsilon} = 0.0002\ sec^{-1}$ | | | | |
| | 0.0040 | 2600 | 438 | oxidation |
| | 0.0070 | 1028 | 116 | oxidation |
| | 0.0100 | 617 | 50 | oxidation |

Table 4 (continued)

(g) Out-of-Phase TMF, Total Constraint, $T_{min}$ = 150°C, Air

| | $\Delta\varepsilon_{mech}$ | Experimental $N_f$ | Predicted $N_f$ | Governing Damage Mechanism |
|---|---|---|---|---|
| $\dot{\varepsilon} \approx 0.0001\ sec^{-1}$ | | | | |
| | 0.0043 | 13671 | 34839 | fatigue |
| | 0.0051 | 3048 | 15168 | fatigue |
| | 0.0058 | 4850 | 6592 | fatigue |
| | 0.0060 | 1524 | 5581 | fatigue |
| | 0.0066 | 2222 | 2706 | oxidation |
| | 0.0068 | 2181 | 2457 | oxidation |
| | 0.0076 | 800 | 965 | oxidation |
| * | 0.0076 | 735 | 965 | oxidation |
| | 0.0081 | 450 | 617 | oxidation |
| | 0.0081 | 430 | 617 | oxidation |
| | 0.0085 | 573 | 379 | oxidation |
| | 0.0085 | 436 | 379 | oxidation |
| | 0.0085 | 175 | 379 | oxidation |
| | 0.0094 | 410 | 166 | oxidation |

(h) Out-of-Phase TMF, Total Constraint, $T_{min}$ = 150°C, Helium

| | $\Delta\varepsilon_{mech}$ | Experimental $N_f$ | Predicted $N_f$ | Governing Damage Mechanism |
|---|---|---|---|---|
| $\dot{\varepsilon} \approx 0.0001\ sec^{-1}$ | | | | |
| | 0.0060 | 7135 | 8517 | fatigue |
| | 0.0076 | 2165 | 3373 | fatigue |
| | 0.0085 | 642 | 2187 | fatigue |

Table 4 (continued)

(i) Out-of-Phase TMF, Total Constraint, $T_{min}$ = 400°C, Air

| | $\Delta\varepsilon_{mech}$ | Experimental $N_f$ | Predicted $N_f$ | Governing Damage Mechanism |
|---|---|---|---|---|
| $\dot{\varepsilon} \approx 0.0001\ sec^{-1}$ | | | | |
| | 0.0034 | 2537 | 6389 | oxidation |
| | 0.0051 | 1099 | 646 | oxidation |

(j) Out-of-Phase TMF, Total Constraint, $T_{min}$ = 500°C, Air

| | $\Delta\varepsilon_{mech}$ | Experimental $N_f$ | Predicted $N_f$ | Governing Damage Mechanism |
|---|---|---|---|---|
| $\dot{\varepsilon} \approx 0.0001\ sec^{-1}$ | | | | |
| | 0.0017 | 10709 | 29410 | oxidation |
| | 0.0026 | 2010 | 5125 | oxidation |
| | 0.0034 | 1217 | 1458 | oxidation |

(k) Out-of-Phase TMF, Total Constraint, $T_{min}$ = 550°C, Air

| | $\Delta\varepsilon_{mech}$ | Experimental $N_f$ | Predicted $N_f$ | Governing Damage Mechanism |
|---|---|---|---|---|
| $\dot{\varepsilon} \approx 0.0001\ sec^{-1}$ | | | | |
| | 0.0017 | 13287 | 11180 | oxidation |

(l) Out-of-Phase TMF, Partial Constraint, $T_{min}$ = 150°C, Air

| | $\Delta\varepsilon_{mech}$ | Experimental $N_f$ | Predicted $N_f$ | Governing Damage Mechanism |
|---|---|---|---|---|
| $\dot{\varepsilon} \approx 0.0001\ sec^{-1}$ | | | | |
| | 0.0039 | 5000+ | 11250 | oxidation |
| | 0.0041 | 1538+ | 4425 | oxidation |
| | 0.0058 | 560+ | 1018 | oxidation |
| | 0.0064 | 258+ | 585 | oxidation |

+ Indicates instability developed (see Ref. [39]).

Table 4 (continued)

(m) Out-of-Phase TMF, Over Constraint, $T_{min}$ = 150°C, Air

| | $\Delta\varepsilon_{mech}$ | Experimental $N_f$ | Predicted $N_f$ | Governing Damage Mechanism |
|---|---|---|---|---|
| $\dot{\varepsilon} \approx 0.0001\ sec^{-1}$ | | | | |
| | 0.0068 | 4000 | 5223 | fatigue |
| | 0.0085 | 1900 | 2137 | fatigue |
| | 0.0102 | 666 | 1065 | fatigue |
| | 0.0119 | 350 | 584 | fatigue |
| | 0.0153 | 56 | 175 | fatigue |
| | 0.0153 | 65 | 175 | fatigue |

(n) In-Phase TMF, $T_{min}$ = 150°C, Air

| | $\Delta\varepsilon_{mech}$ | Experimental $N_f$ | Predicted $N_f$ | Governing Damage Mechanism |
|---|---|---|---|---|
| $\dot{\varepsilon} \approx 0.0001\ sec^{-1}$ | | | | |
| | 0.0051 | 5686 | 10220 | fatigue |
| | 0.0060 | 1590 | 2013 | creep |
| | 0.0068 | 438 | 500 | creep |
| * | 0.0076 | 220 | 229 | creep |
| | 0.0076 | 215 | 229 | creep |
| | 0.0094 | 161 | 115 | creep |

(o) In-Phase TMF, $T_{min}$ = 150°C, Helium

| | $\Delta\varepsilon_{mech}$ | Experimental $N_f$ | Predicted $N_f$ | Governing Damage Mechanism |
|---|---|---|---|---|
| $\dot{\varepsilon} \approx 0.0001\ sec^{-1}$ | | | | |
| | 0.0060 | 2024 | 2211 | creep |
| | 0.0076 | 432 | 261 | creep |

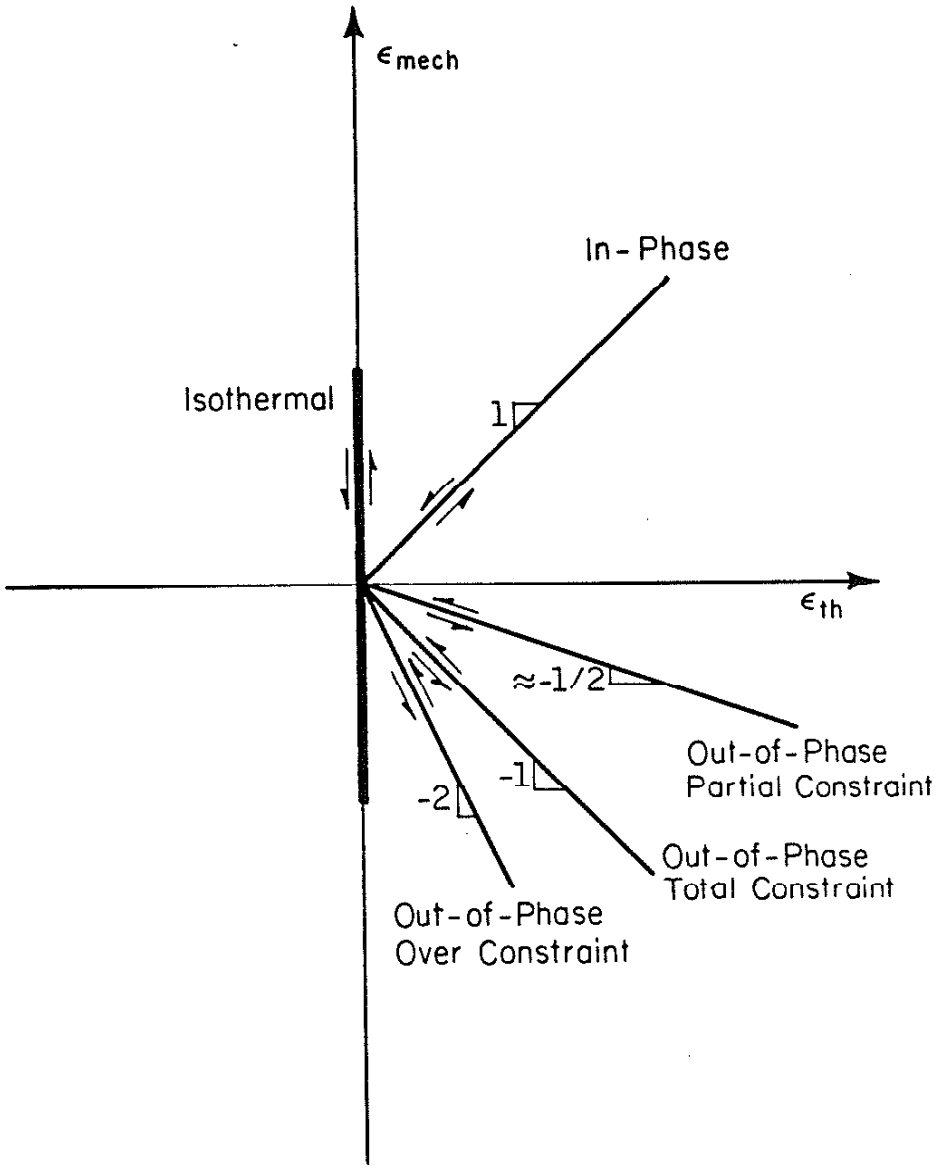


Figure 1 Schematic showing the strain-temperature histories considered in the 1070 steel testing program.

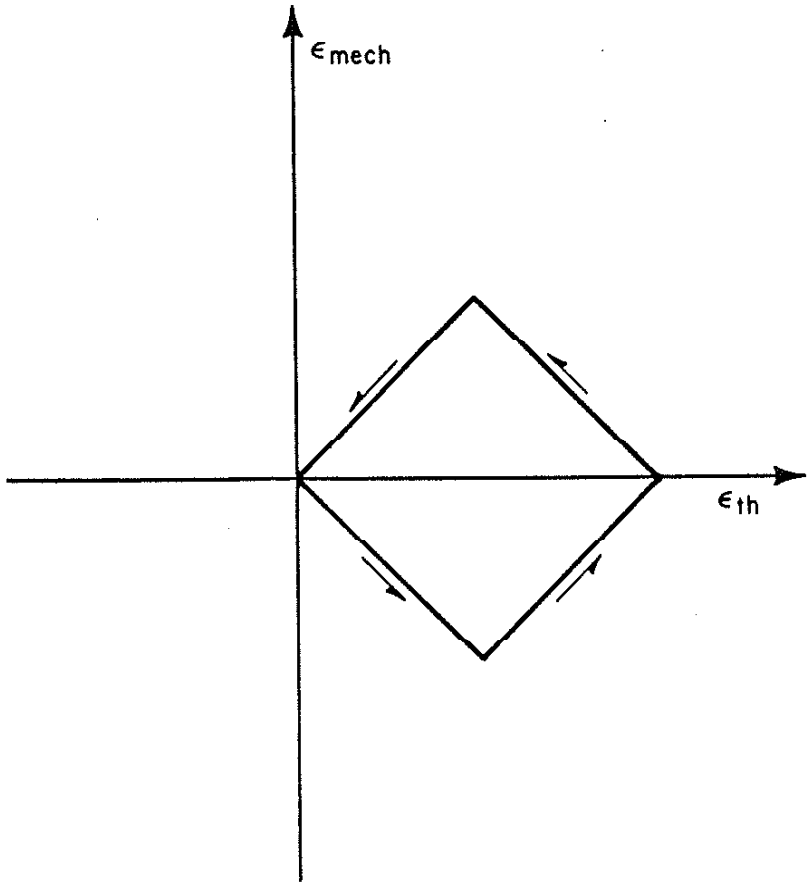


Figure 2 Example of a diamond-shaped non-proportional strain-temperature history.

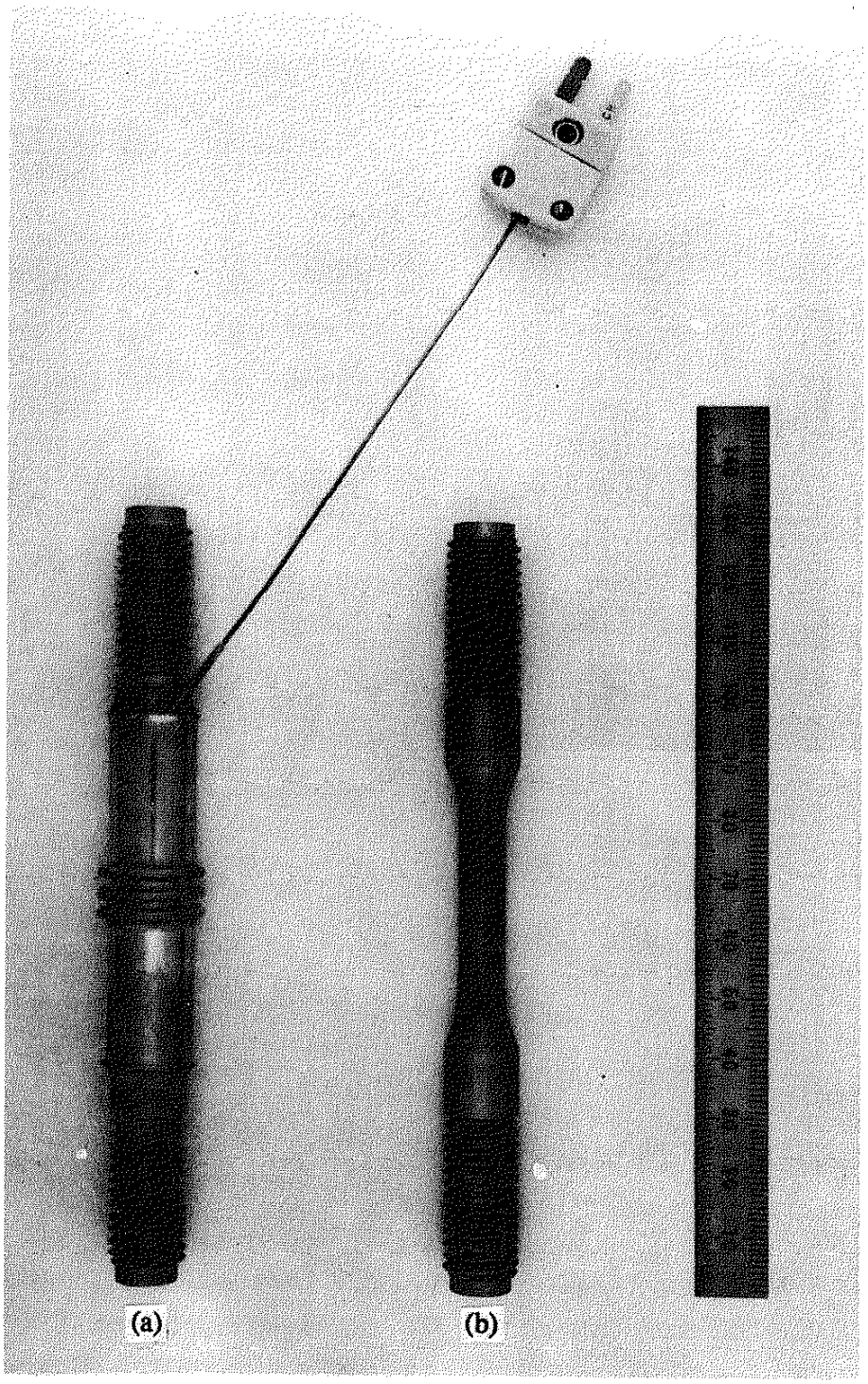


Figure 3 Specimen (a) with bellows and (b) without bellows.

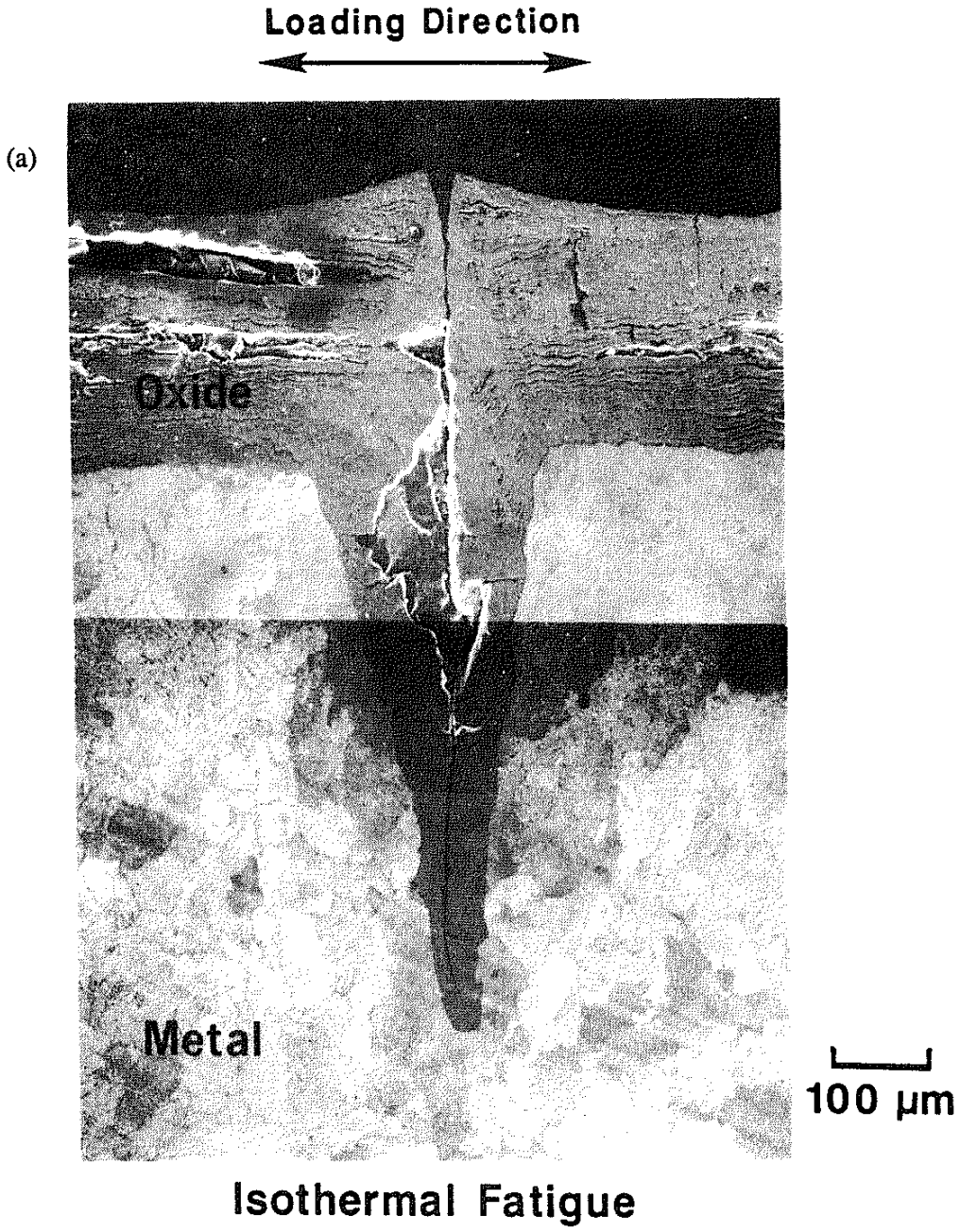


Figure 4 SEM microphotographs showing surface oxide and oxide "intrusions" for three different tests at 80% $N_f$. (a) Isothermal fatigue, T = 600°C, $\Delta\varepsilon_{mech} = 0.0070$, $\dot{\varepsilon} = 0.0002$ sec$^{-1}$, $N_f = 700$; (b) Out-of-phase, total constraint TMF, T = 150-600°C, $\Delta\varepsilon_{mech} = 0.0076$, $\dot{\varepsilon} \approx 0.0001$ sec$^{-1}$, $N_f = 735$; (c) In-phase TMF, T = 150-600°C, $\Delta\varepsilon_{mech} = 0.0076$, $\dot{\varepsilon} \approx 0.0001$ sec$^{-1}$, $N_f = 220$.

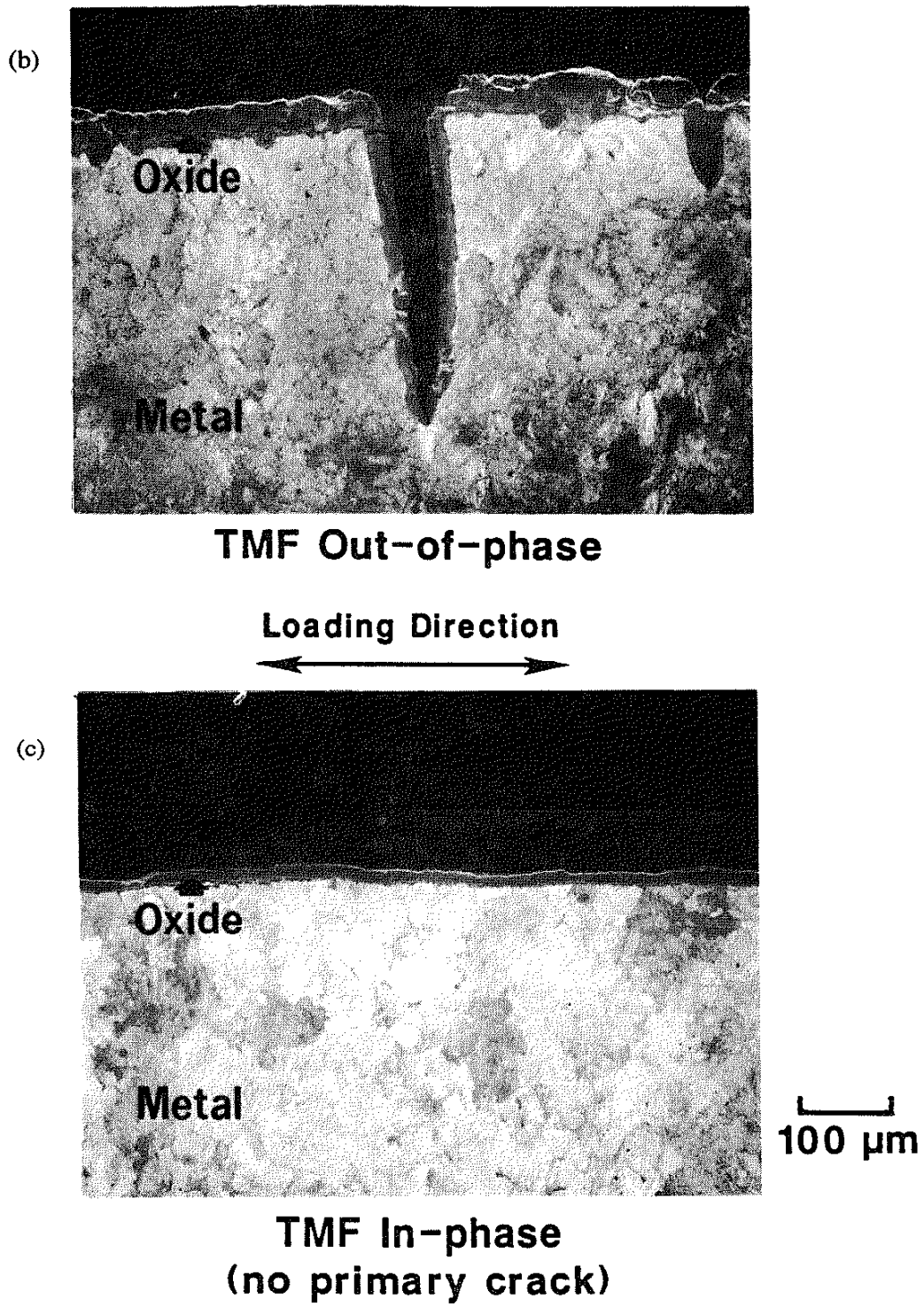


Figure 4 (continued)

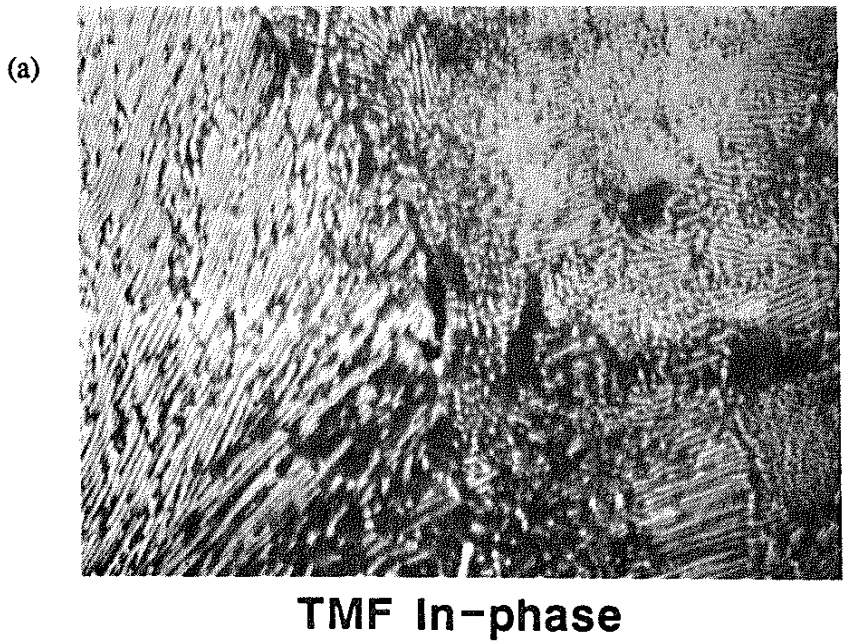


Figure 5 SEM microphotographs showing intergranular cracks in (a) In-phase TMF, T = 150-600°C, $\Delta\varepsilon_{mech}$ = 0.0076, $\dot{\varepsilon} \approx 0.0001\ sec^{-1}$, $N_f$ = 220; and (b) Creep test at 600°C.

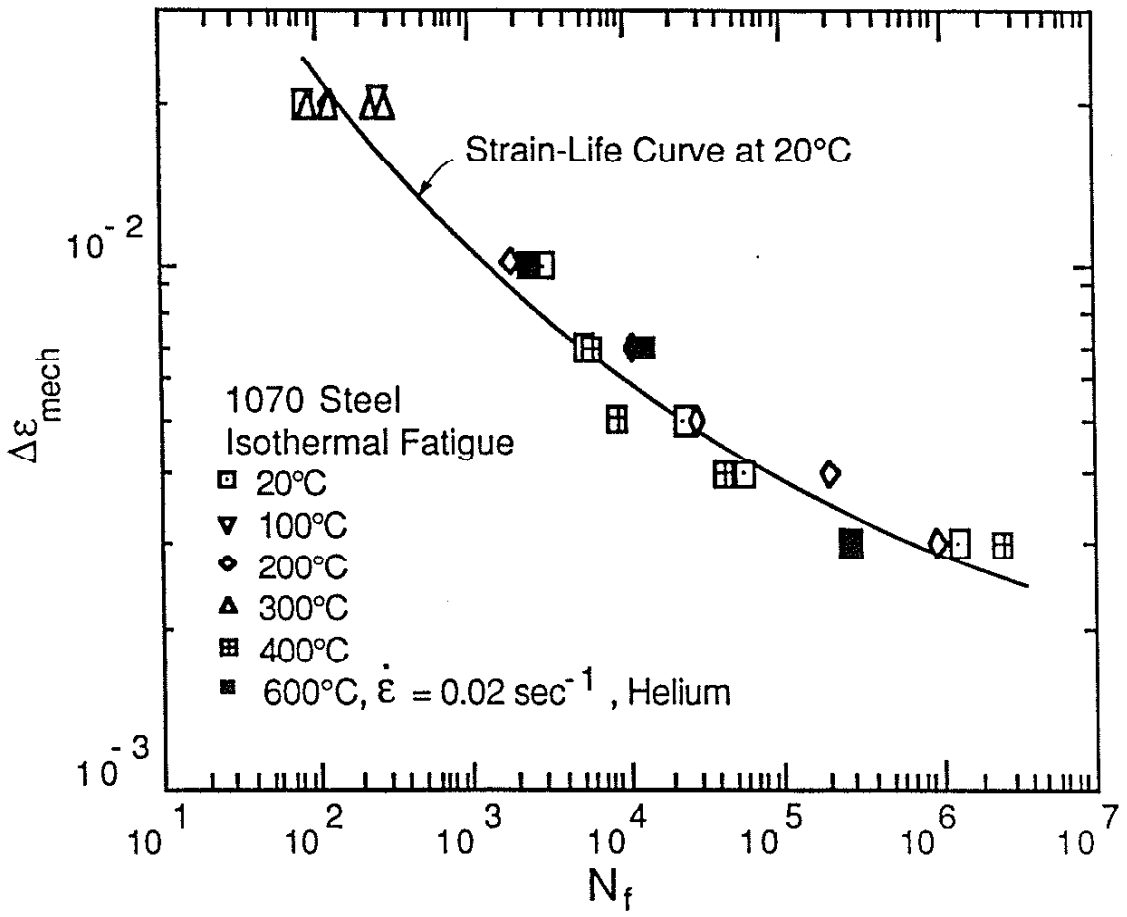


Figure 6 Strain-life curve at 20°C for 1070 steel with test results which have a life governed by fatigue damage only.

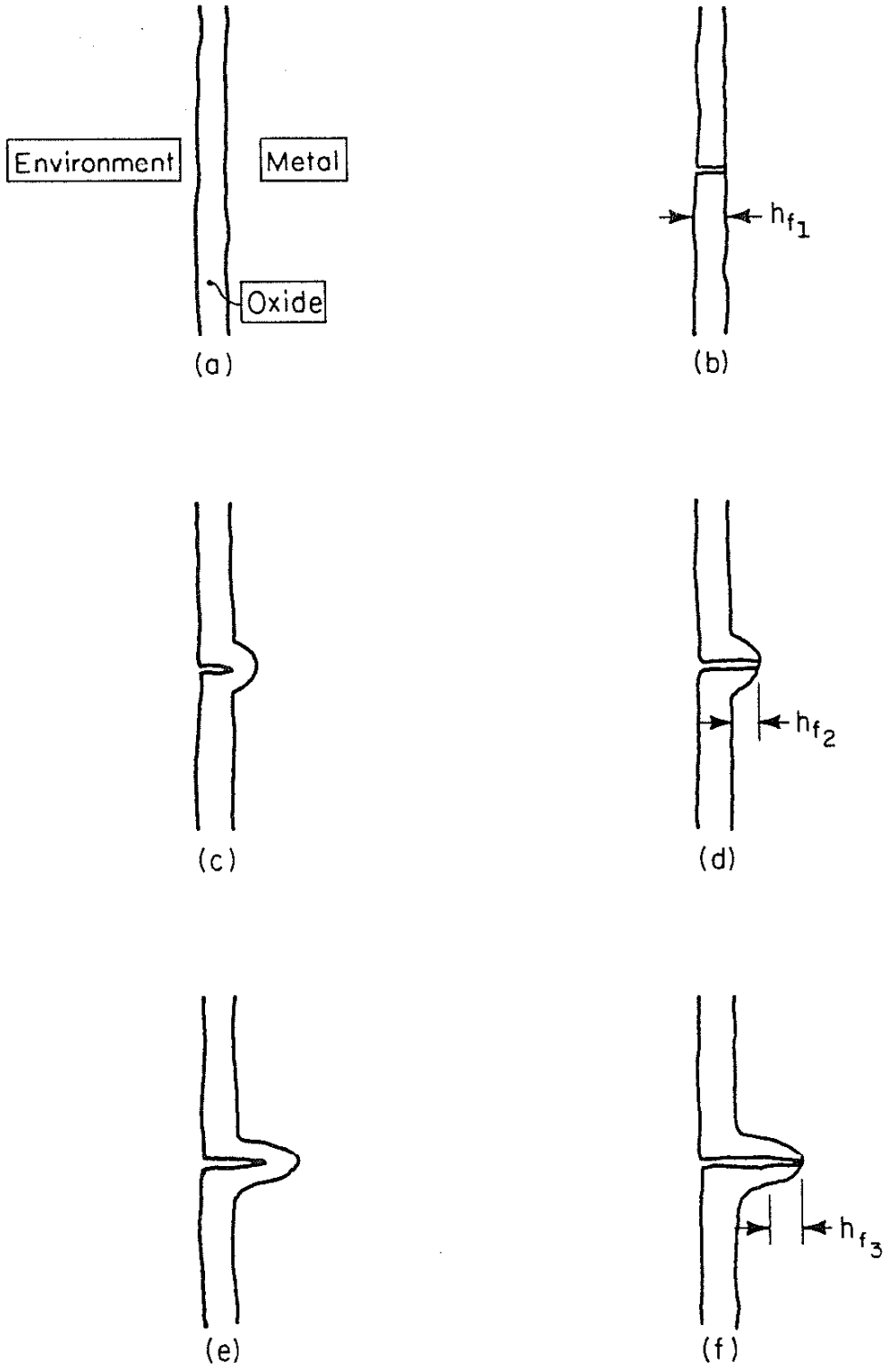


Figure 7 Schematic showing the nucleation of Type I oxide growth.

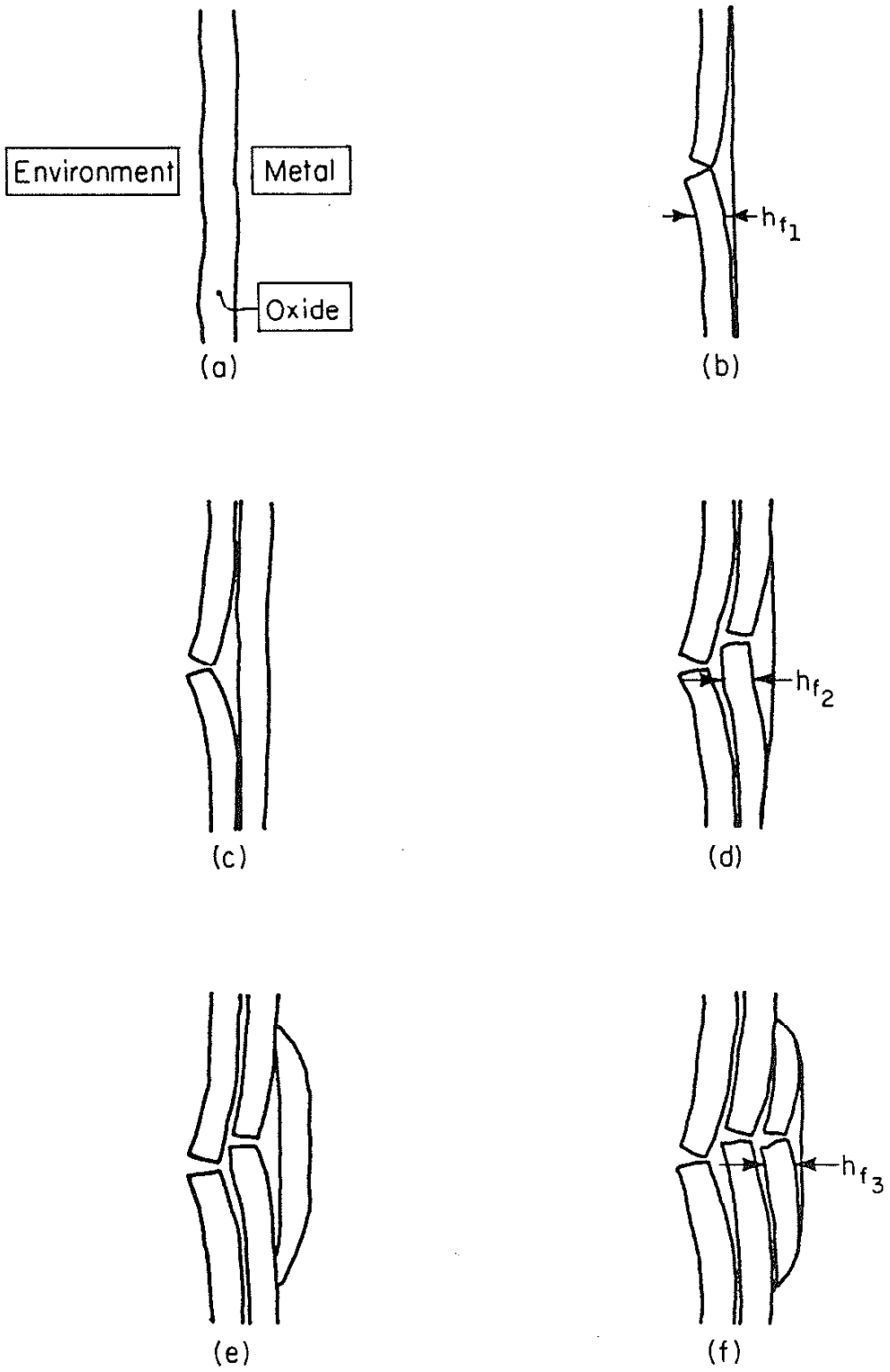


Figure 8 Schematic showing the nucleation of Type II oxide growth.

(a)

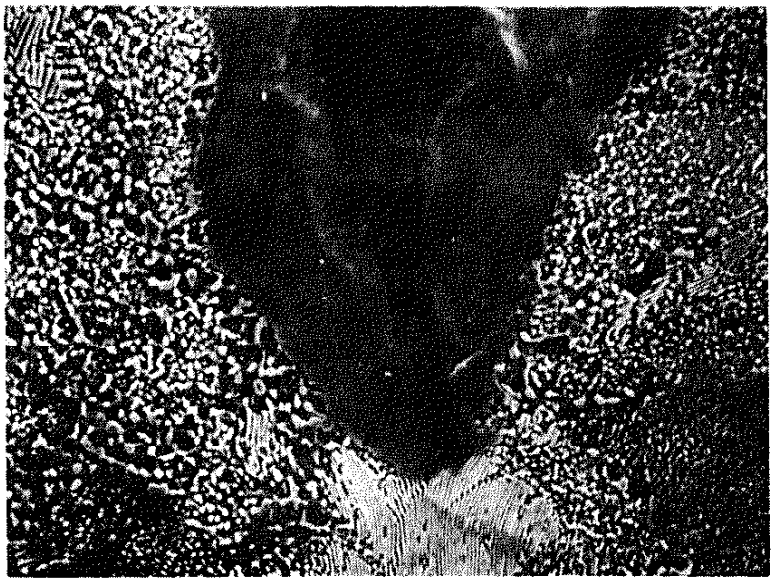

TMF Out-of-phase

Loading Direction

10 μm

(b)

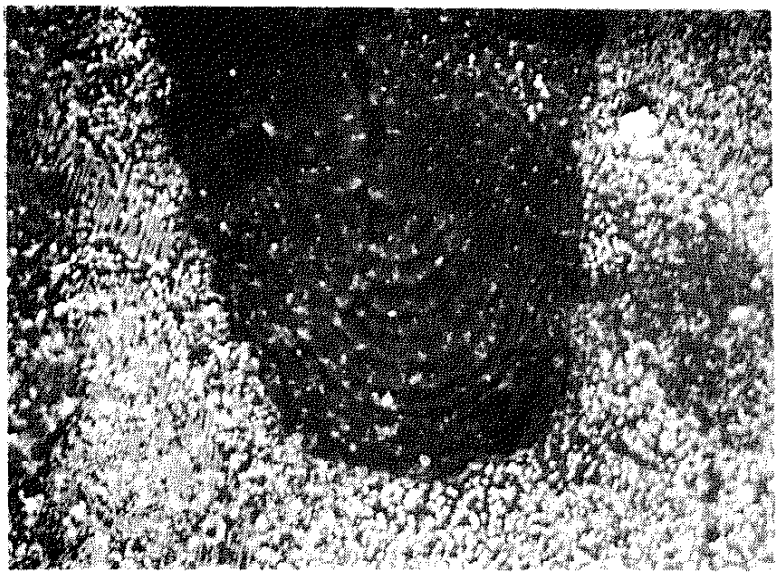

Isothermal Fatigue

Figure 9 SEM microphotographs showing oxide intrusion tips resulting from (a) Type I growth (Out-of-phase TMF, T = 150-600°C, $\Delta\varepsilon_{mech}$ = 0.0076, $\dot{\varepsilon} \approx 0.0001$ sec$^{-1}$) and (b) Type II growth (Isothermal Fatigue, T = 600°C, $\Delta\varepsilon_{mech} = 0.0070$, $\dot{\varepsilon} = 0.0002$ sec$^{-1}$).


Figure 10 SEM microphotograph illustrating the multi-layer oxide and an $h_{fi}$ measurement (Out-of-phase TMF, T = 500-600°C, $\Delta\varepsilon_{mech} = 0.0017$, $\dot{\varepsilon} \approx 0.0001$ sec$^{-1}$).

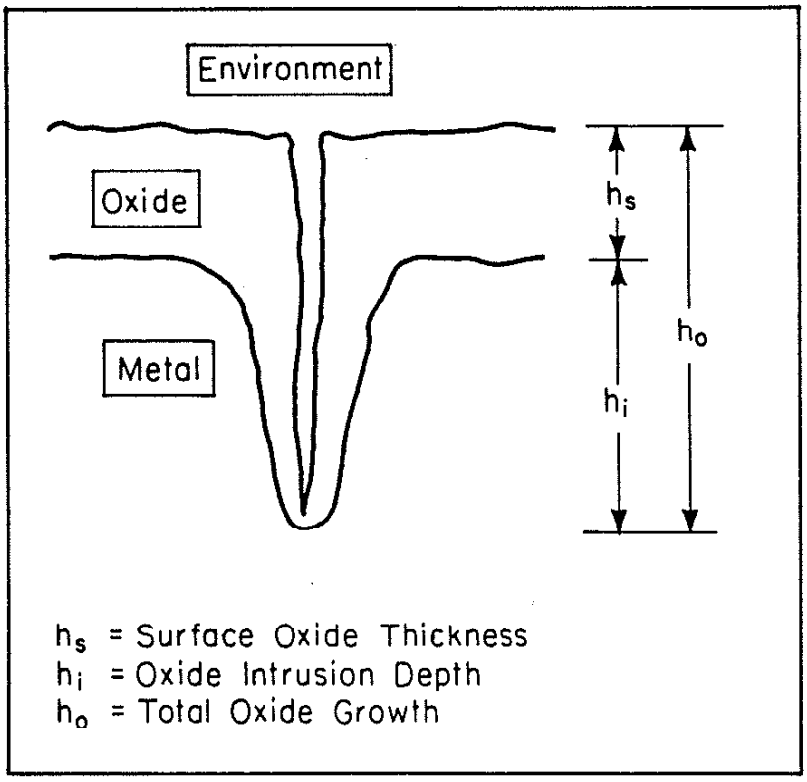


Figure 11 Definitions of $h_s$, $h_i$, and $h_o$.

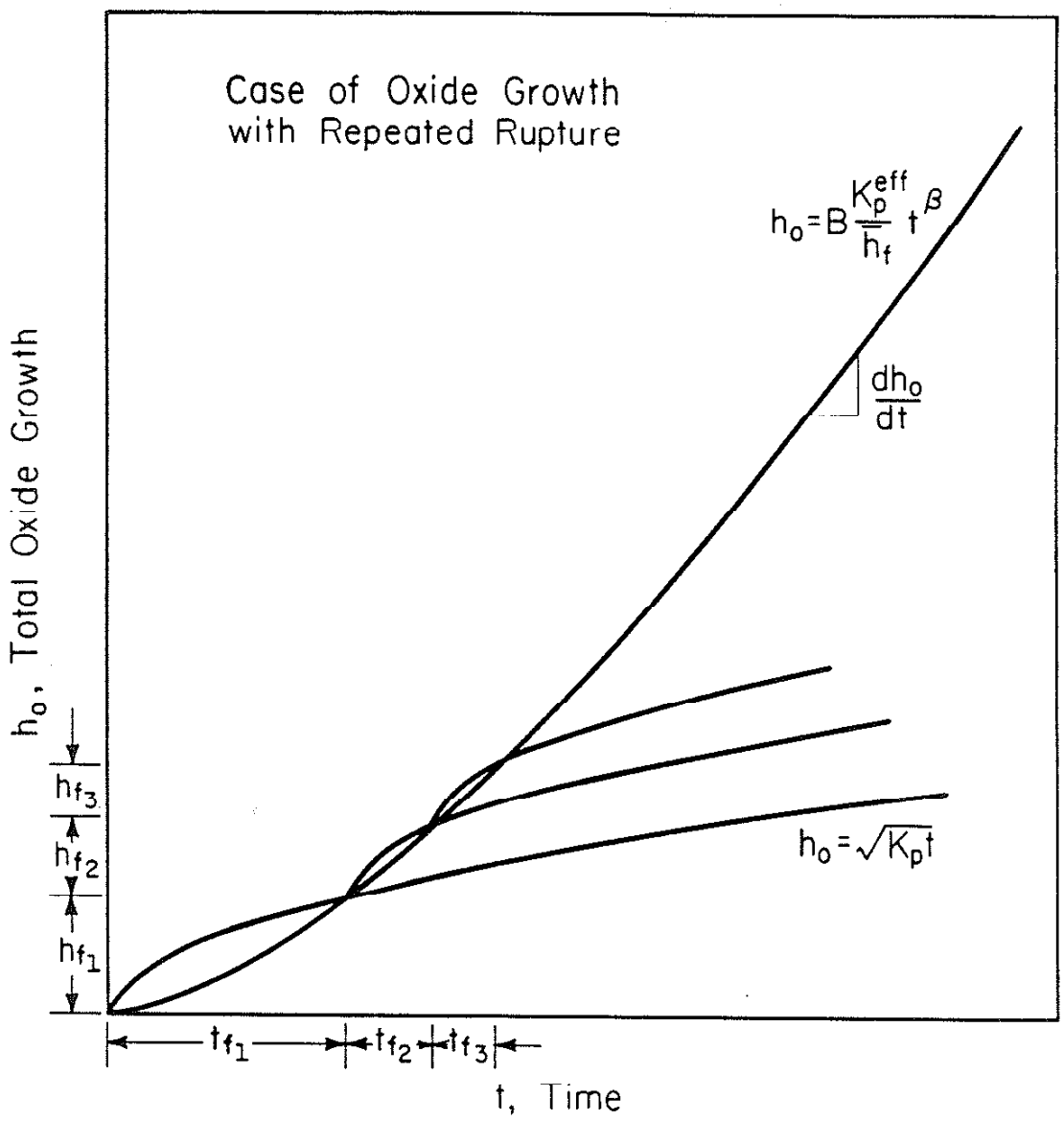


Figure 12 Diagram illustrating oxide growth with repeated rupture.

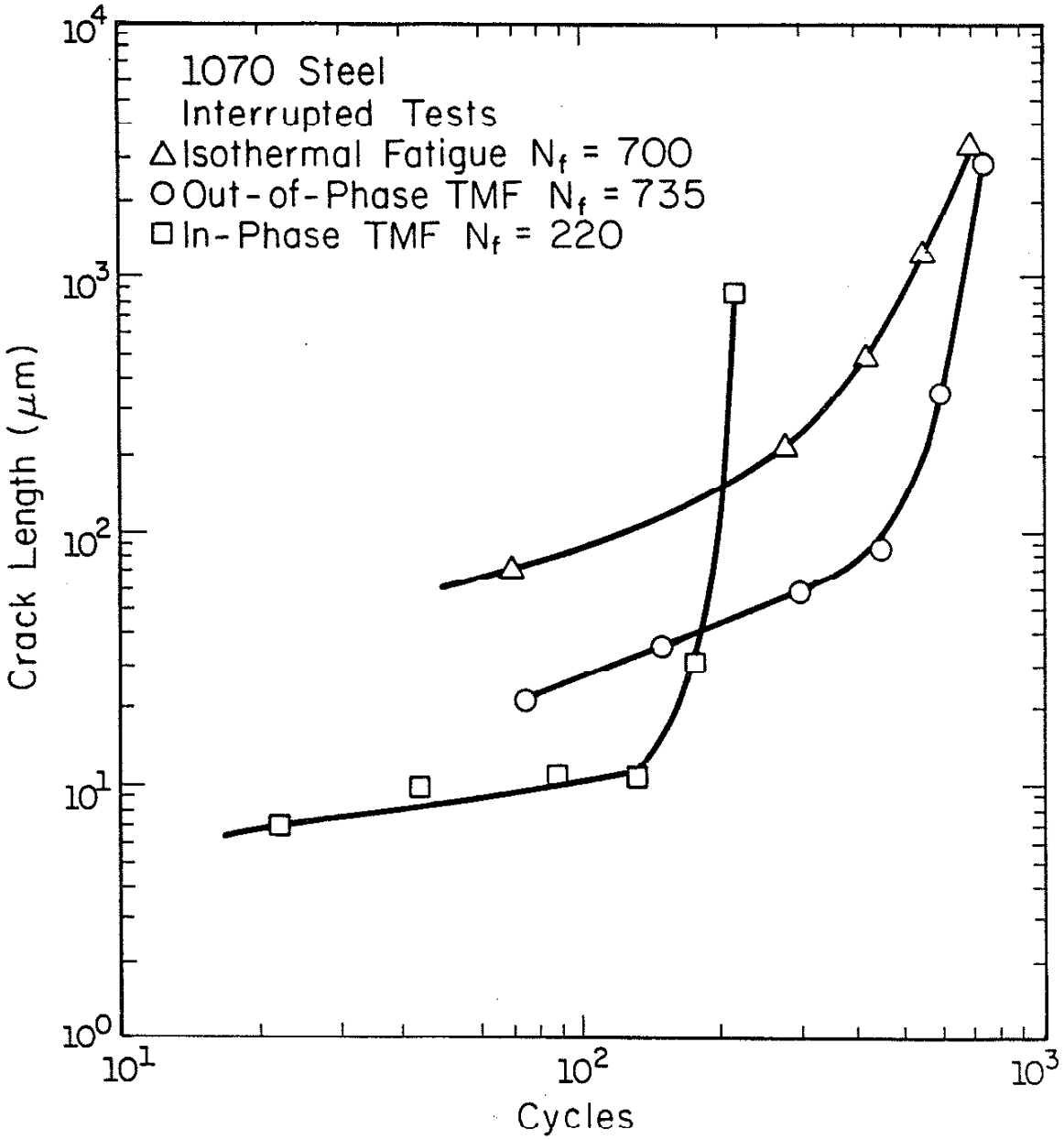


Figure 13 Crack growth for the interrupted tests.

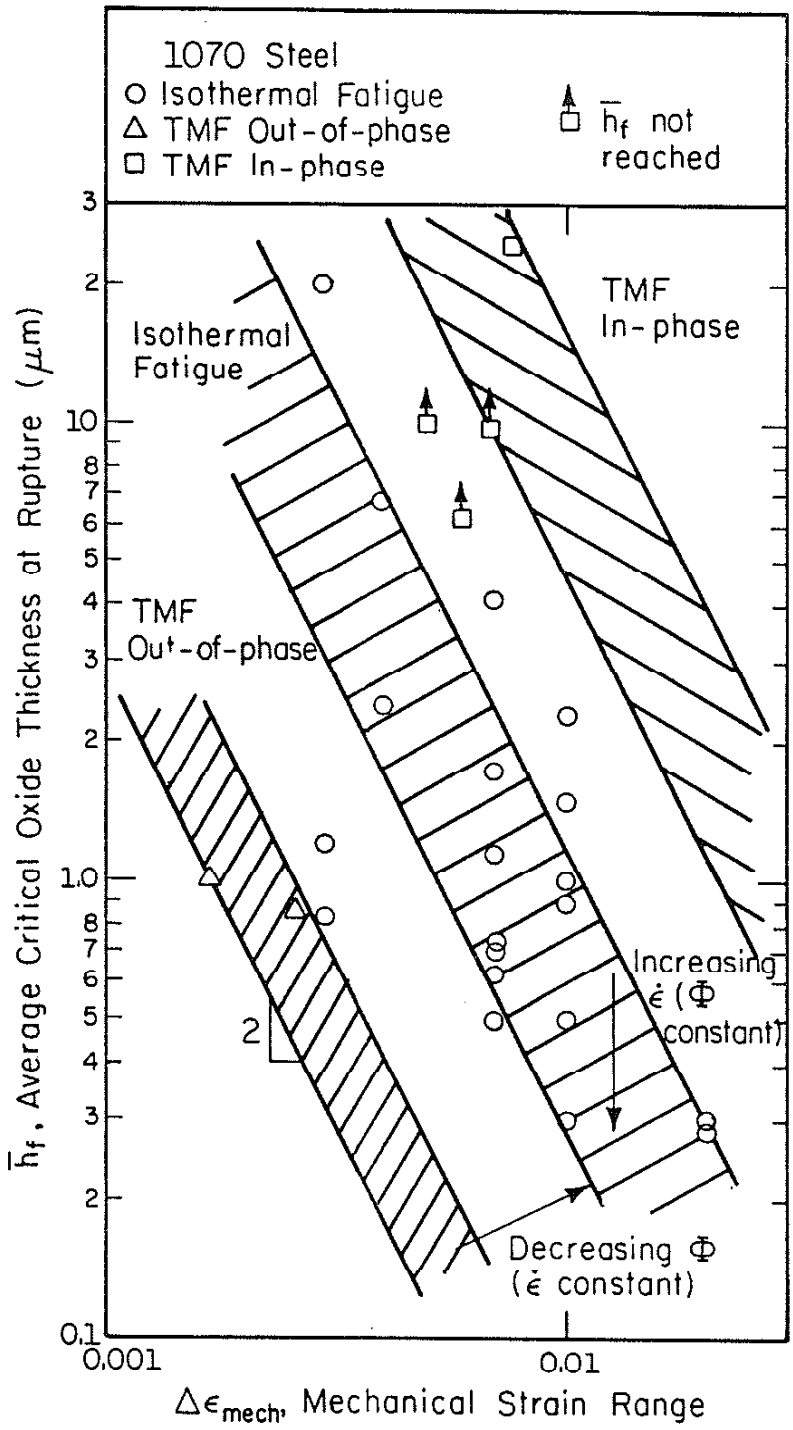


Figure 14 Plot of average critical oxide thickness at rupture from tests of various phasings.

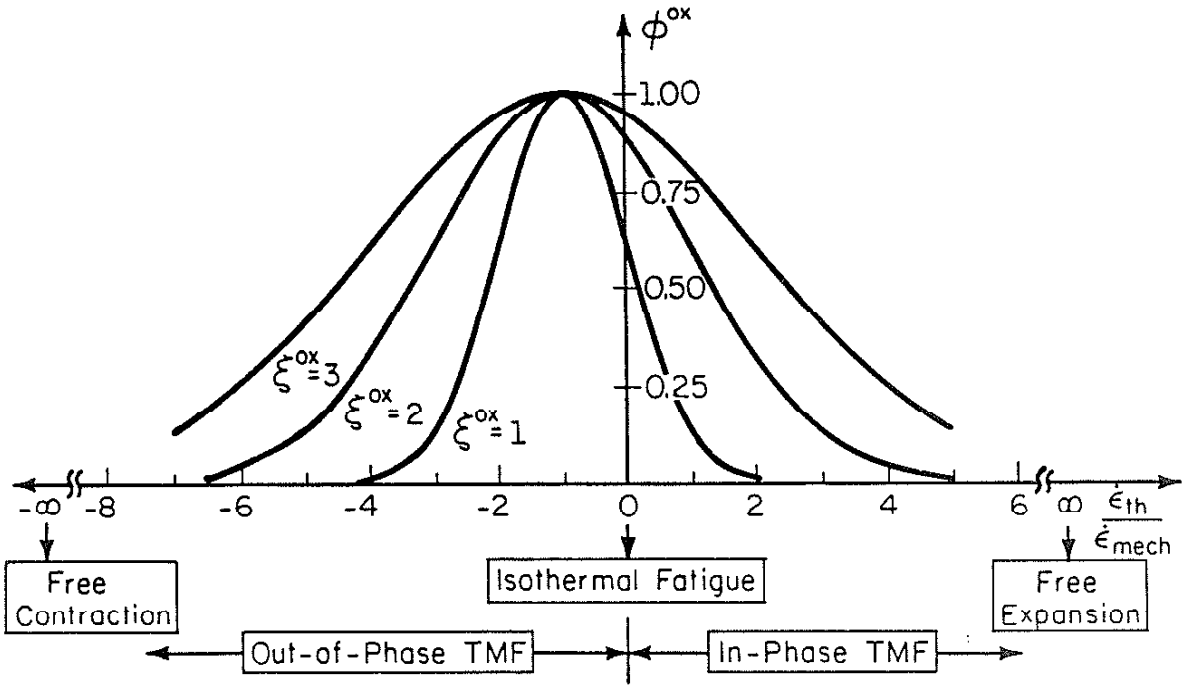


Figure 15 Plot showing the $\phi^{ox}$ function for three different $\xi^{ox}$ values with peak damage occurring at $\dot{\epsilon}_{th}/\dot{\epsilon}_{mech} = -1$.

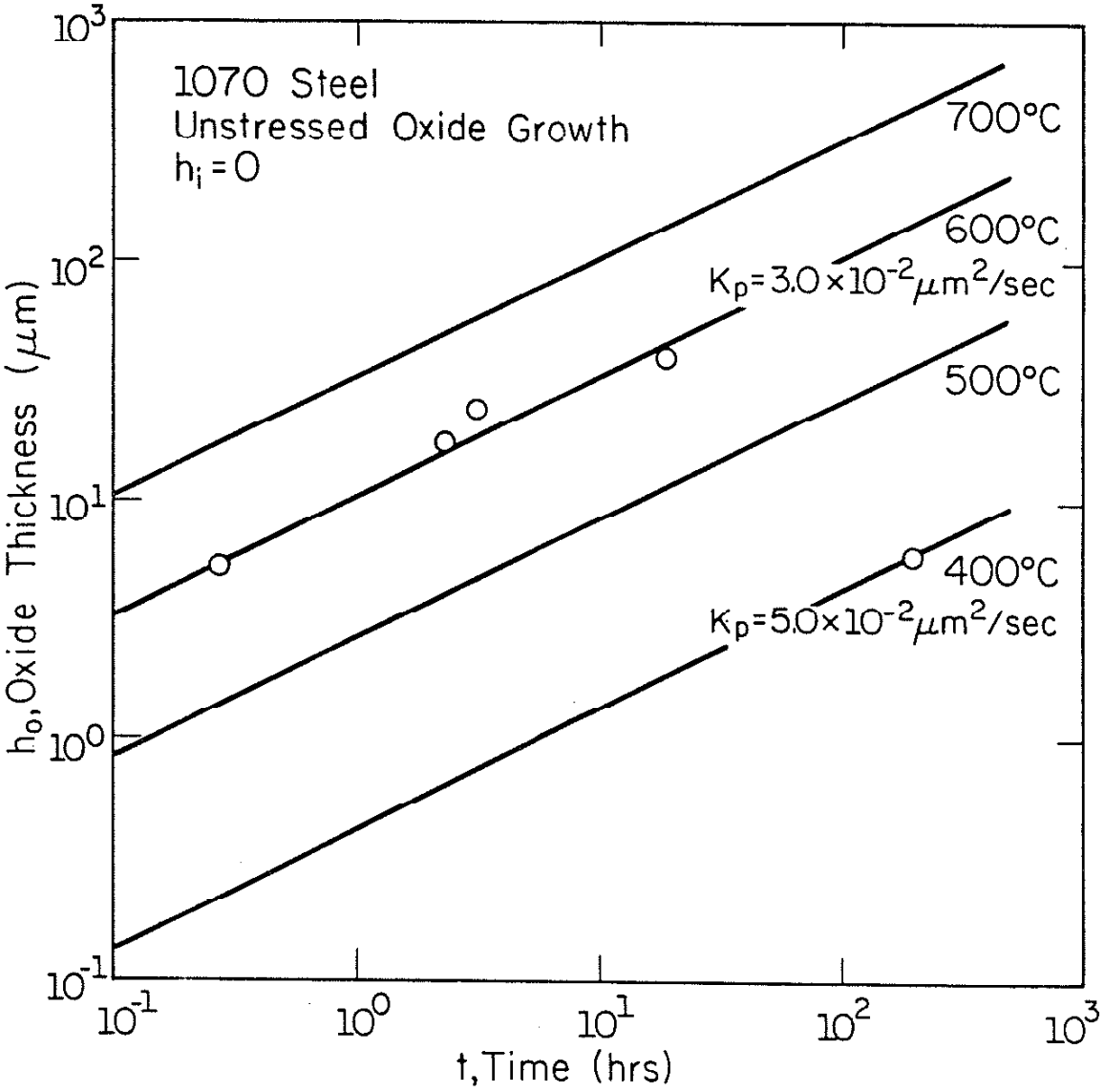


Figure 16 Plot of the unstressed parabolic growth at various temperatures.


Figure 17 SEM microphotograph showing intergranular cracking from in-phase TMF cycling (T = 150-600°C).

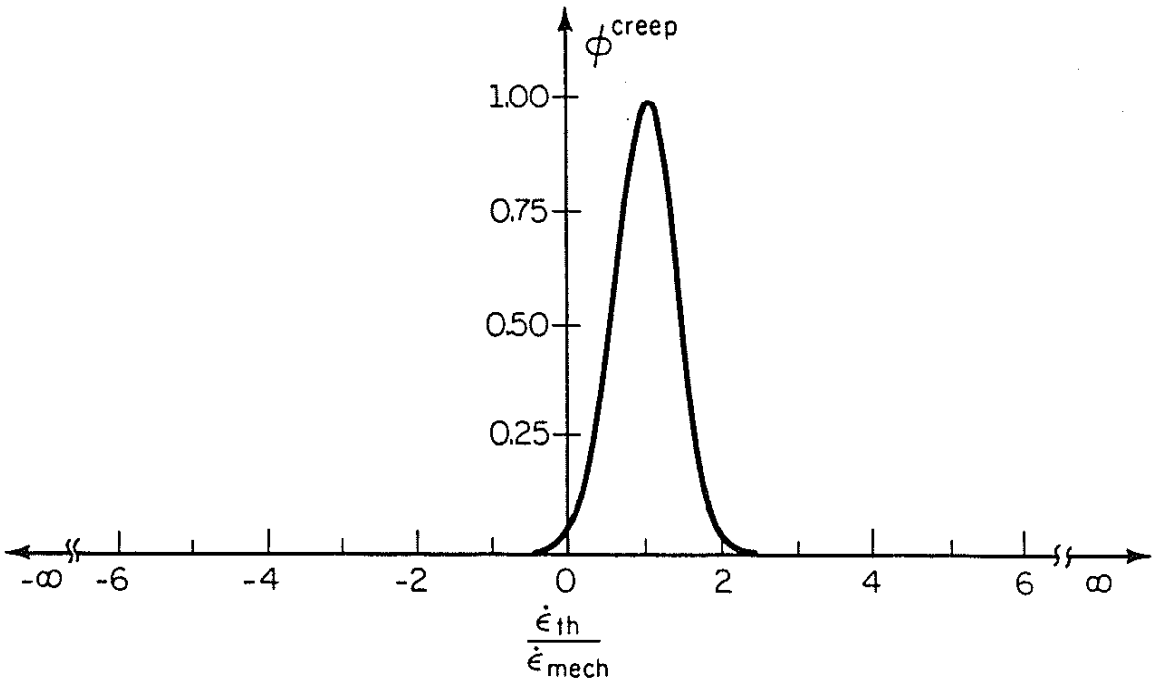


Figure 18 Plot of the creep phasing function, $\phi^{creep}$.

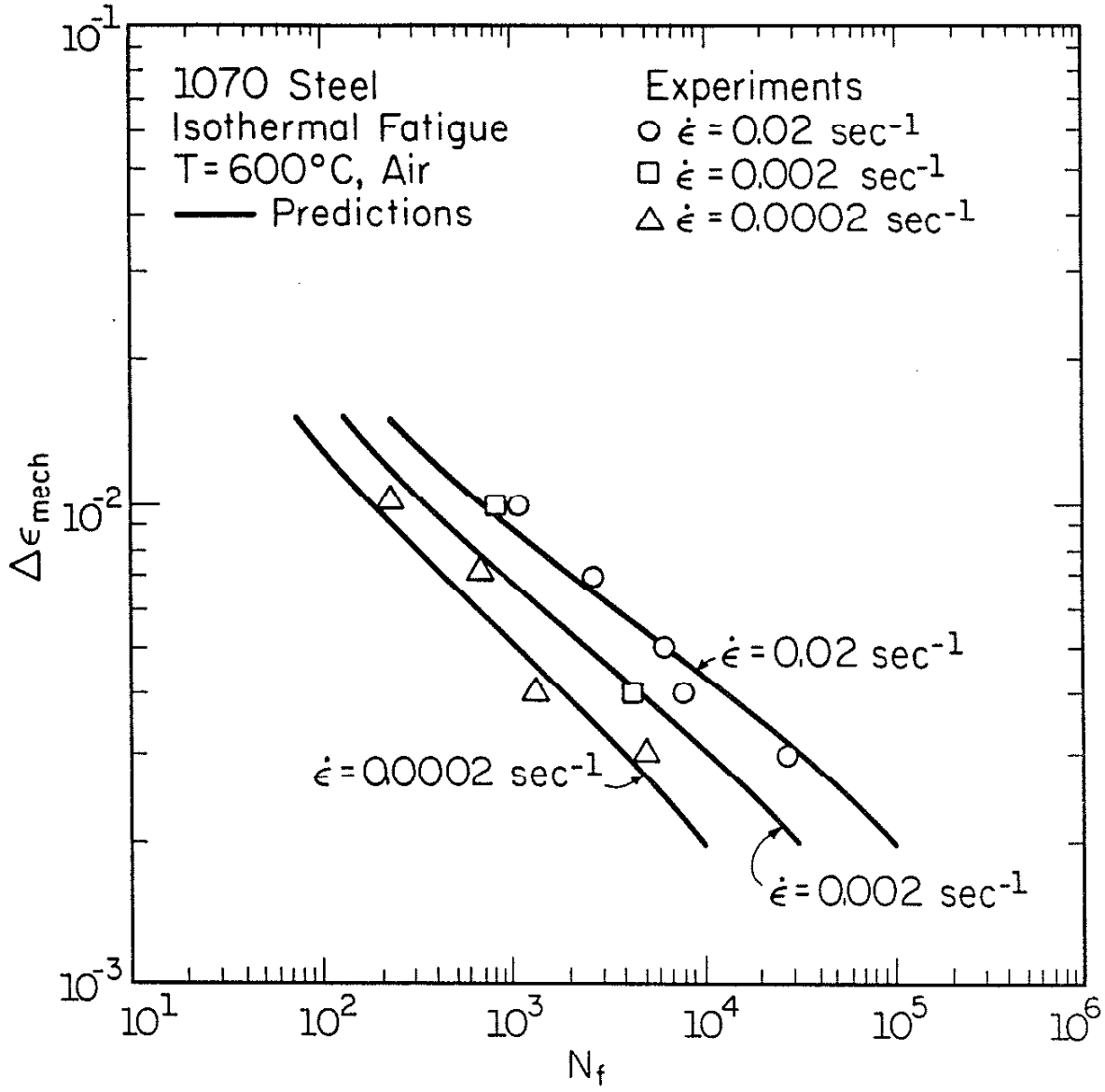


Figure 19 Comparison of predicted and experimental lives for isothermal fatigue, T = 600°C, air.

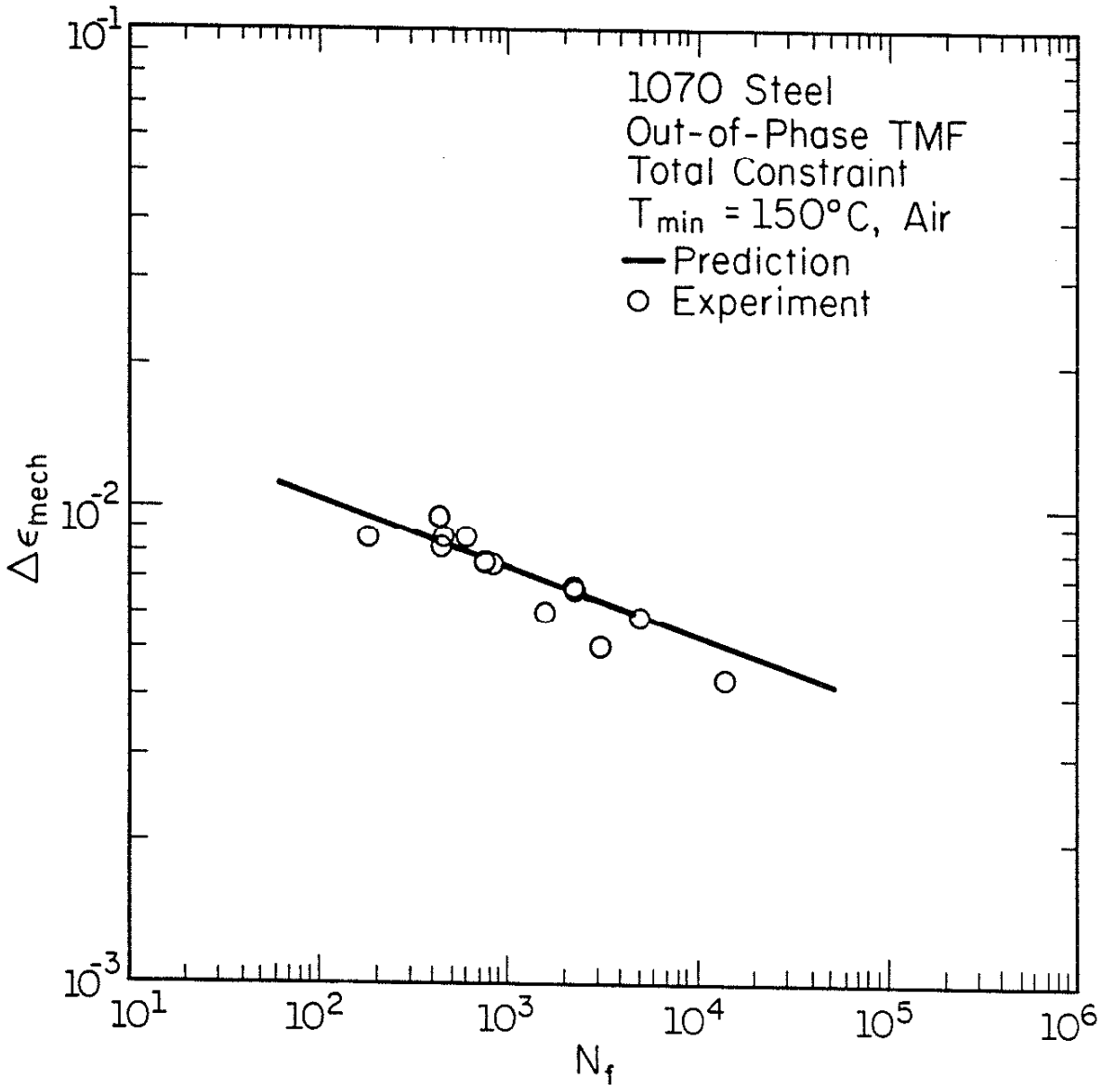


Figure 20 Comparison of predicted and experimental lives for out-of-phase total constraint TMF, $T_{min}$ = 150°C, air.

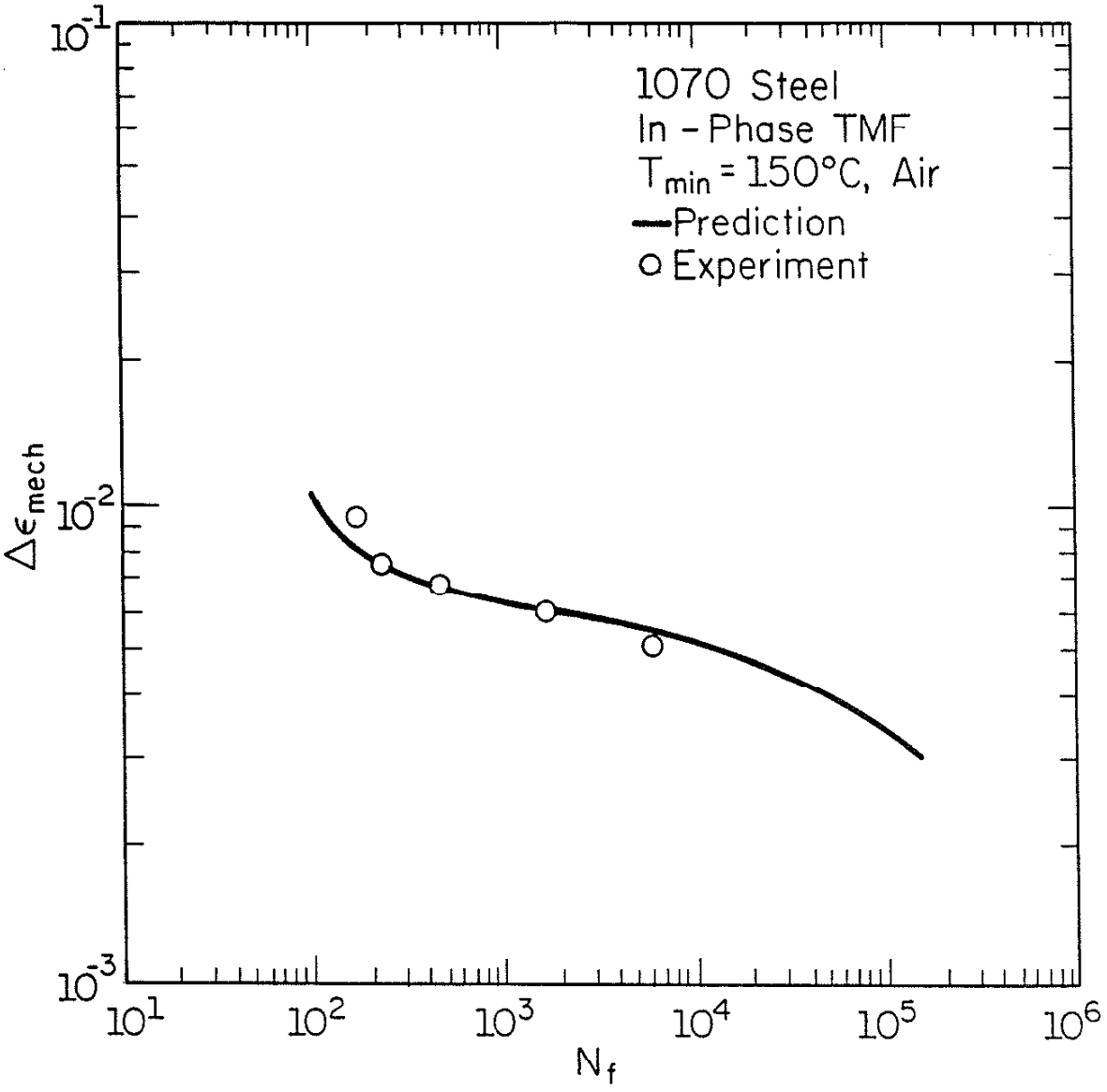


Figure 21 Comparison of predicted and experimental lives for in-phase TMF, $T_{min}$ = 150°C, air.

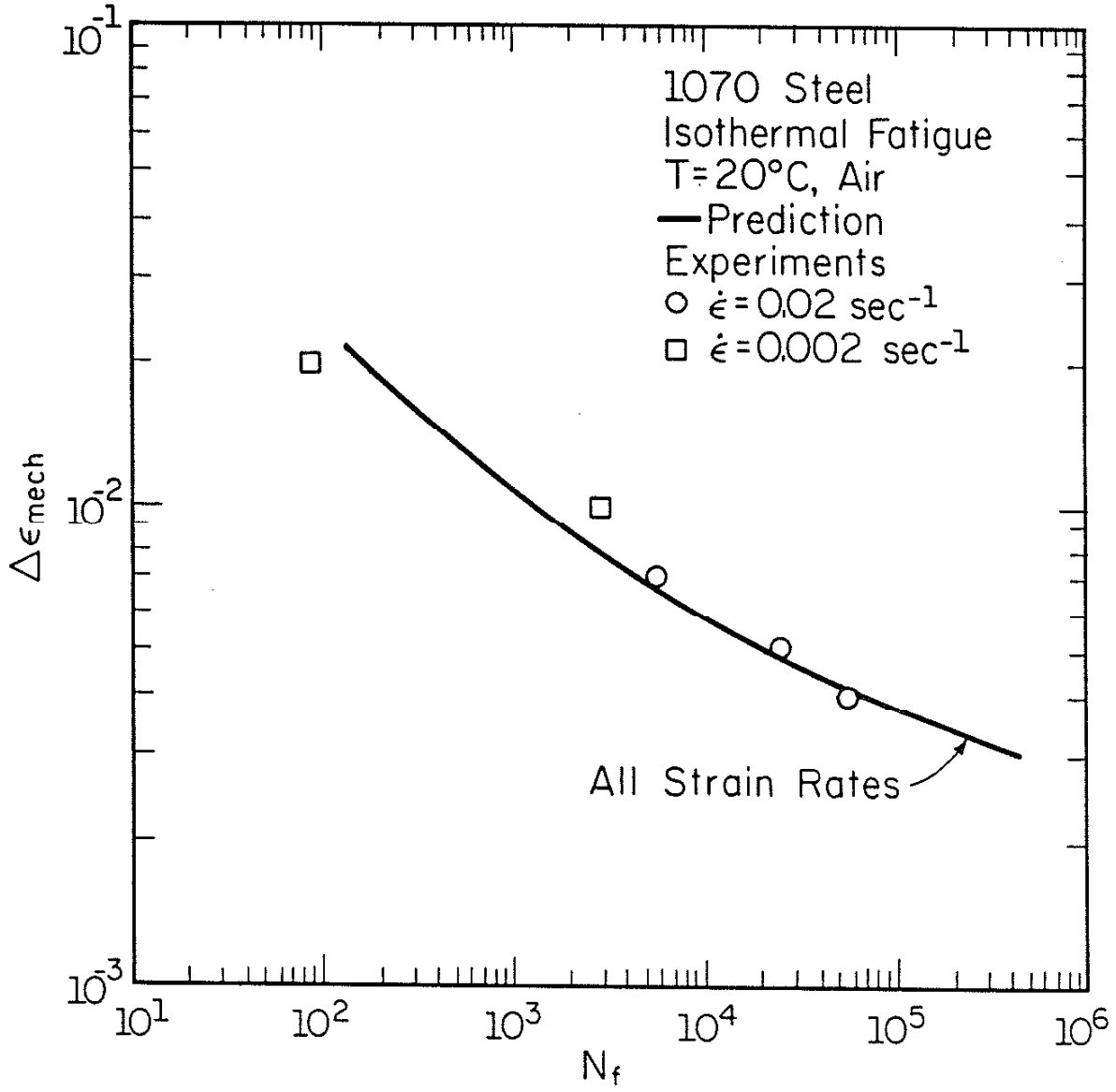


Figure 22 Comparison of predicted and experimental lives for isothermal fatigue, T = 20°C, air.

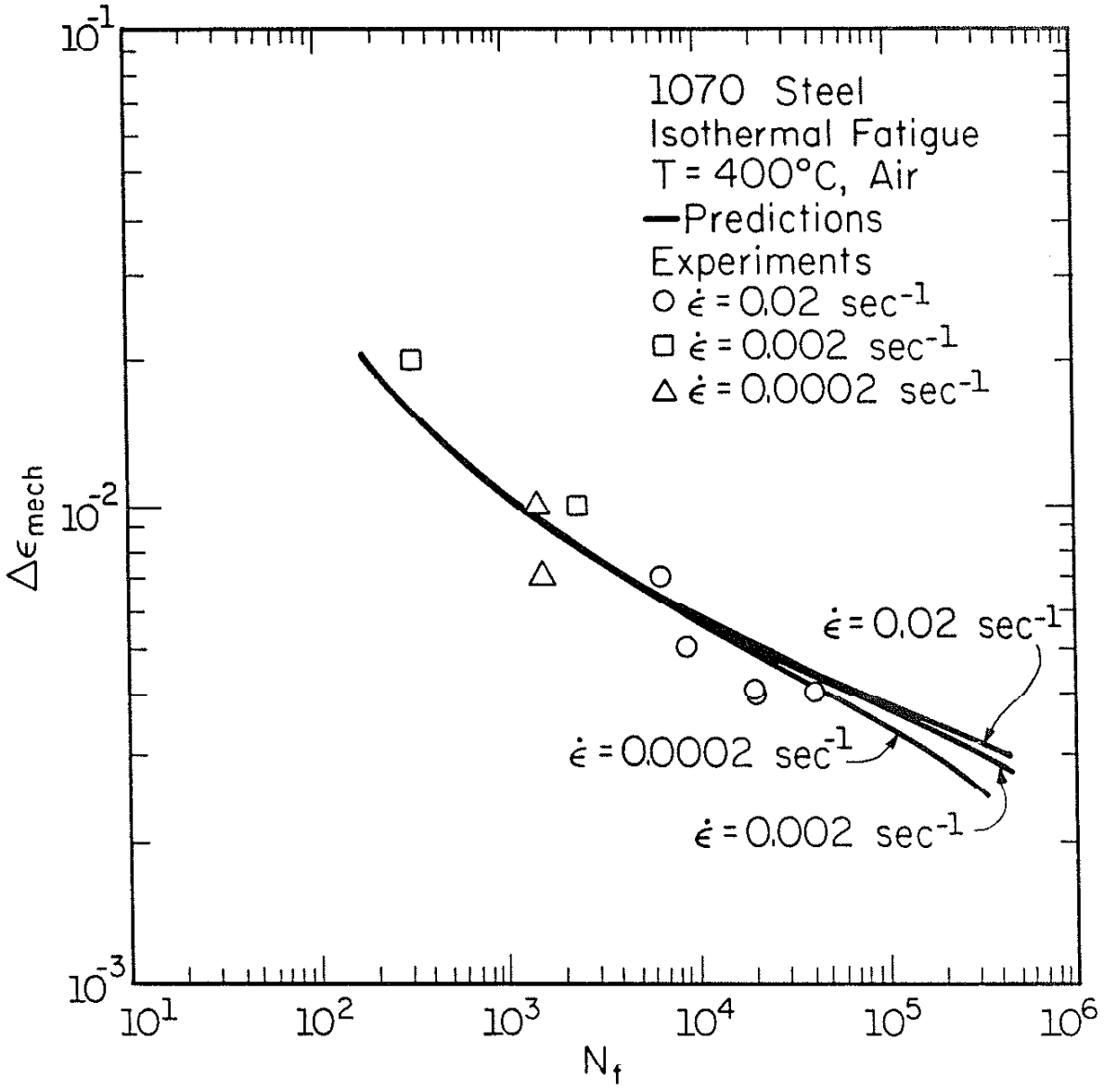


Figure 23 Comparison of predicted and experimental lives for isothermal fatigue, T = 400°C, air.

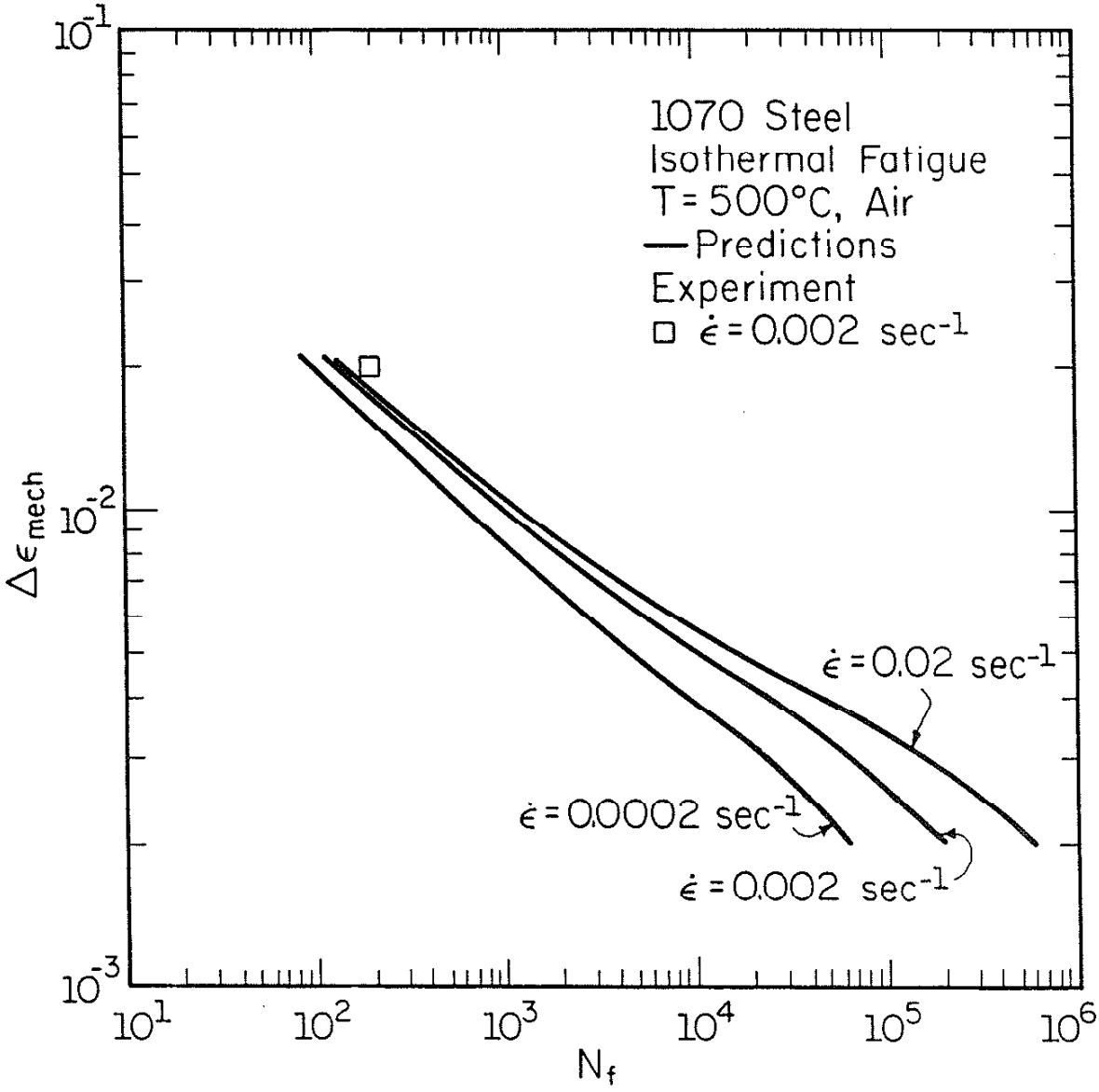


Figure 24 Comparison of predicted and experimental lives for isothermal fatigue, T = 500°C, air.

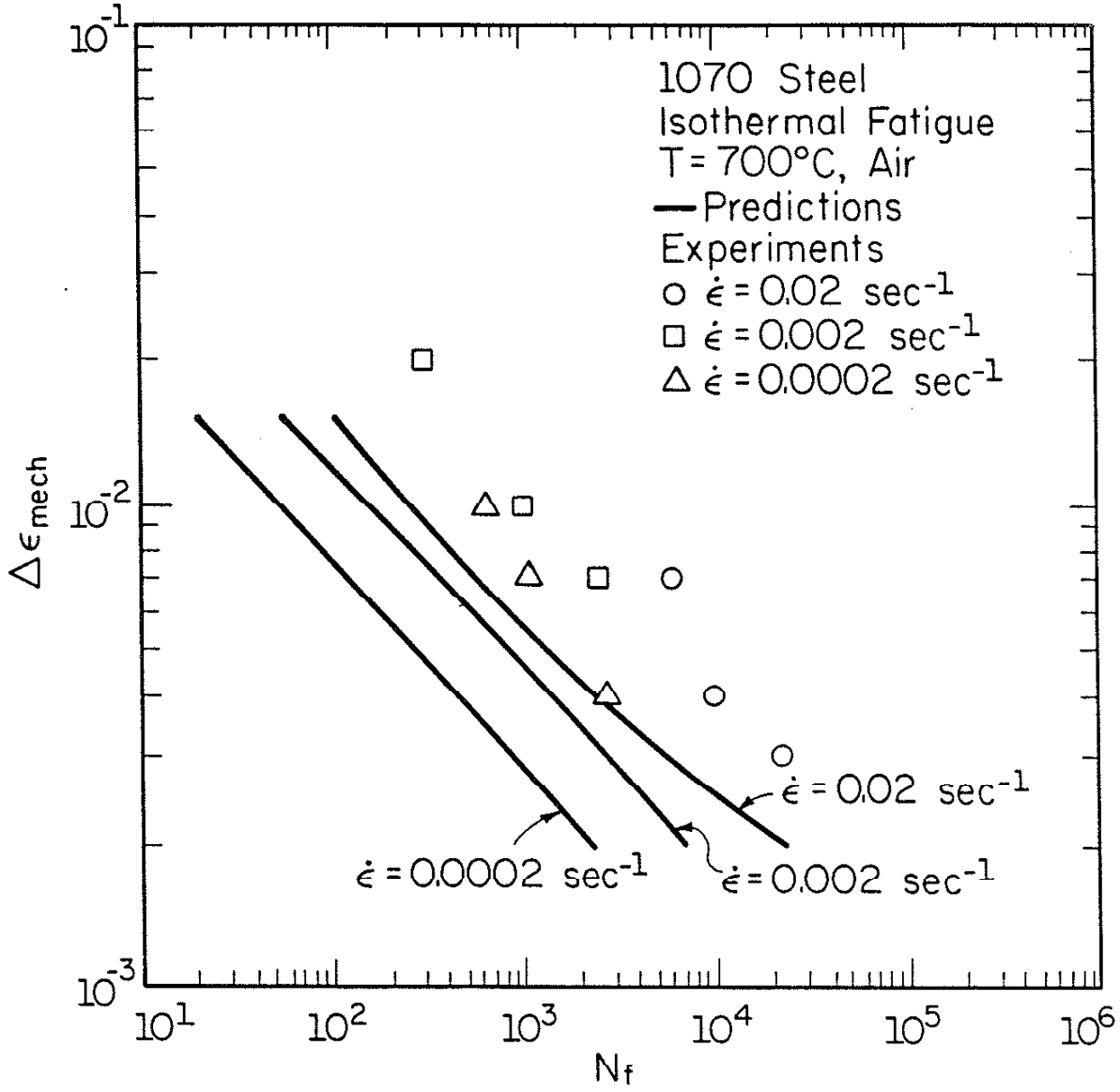


Figure 25 Comparison of predicted and experimental lives for isothermal fatigue, T = 700°C, air.

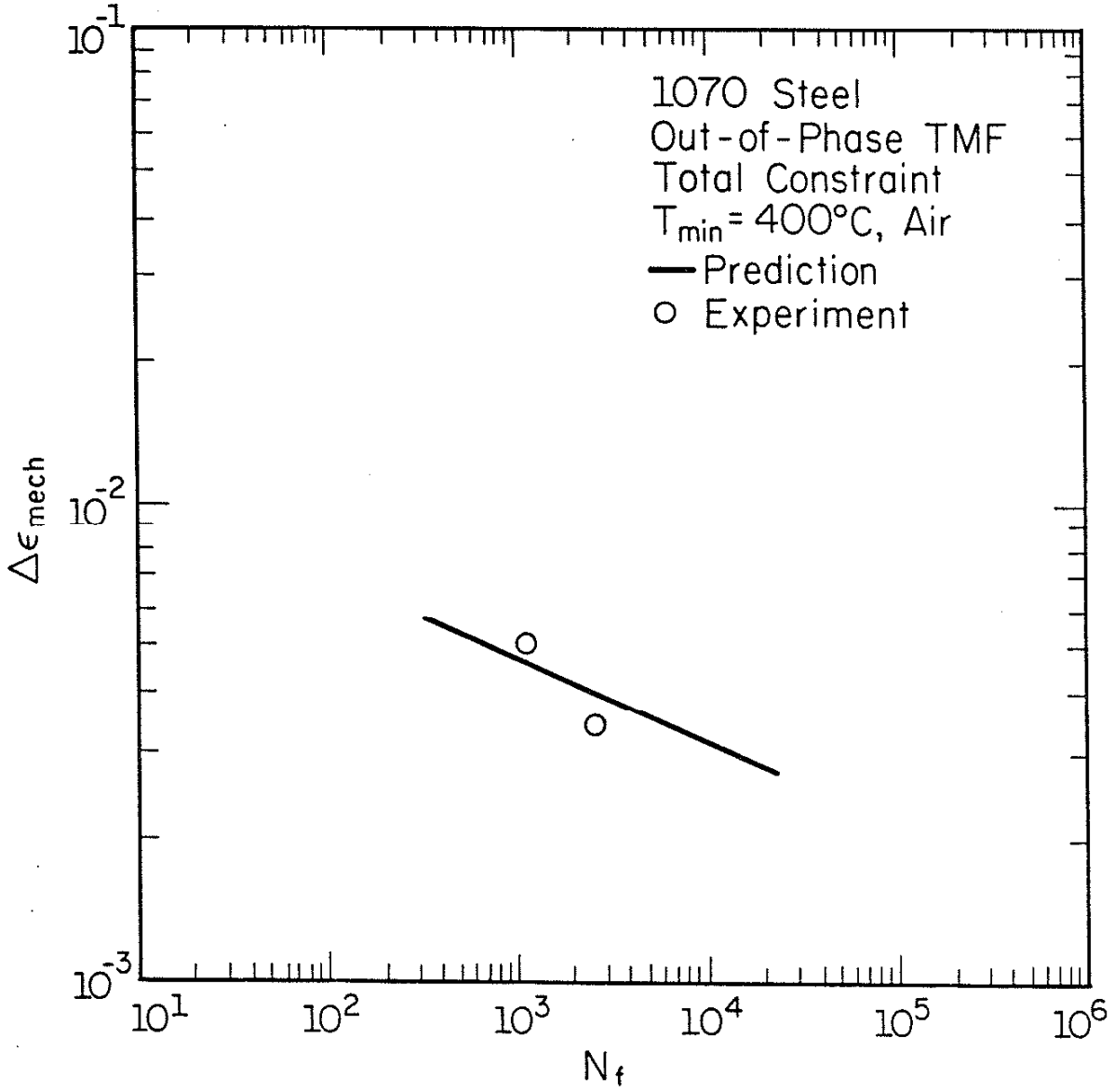


Figure 26 Comparison of predicted and experimental lives for out-of-phase total constraint TMF, $T_{min}$ = 400°C, air.

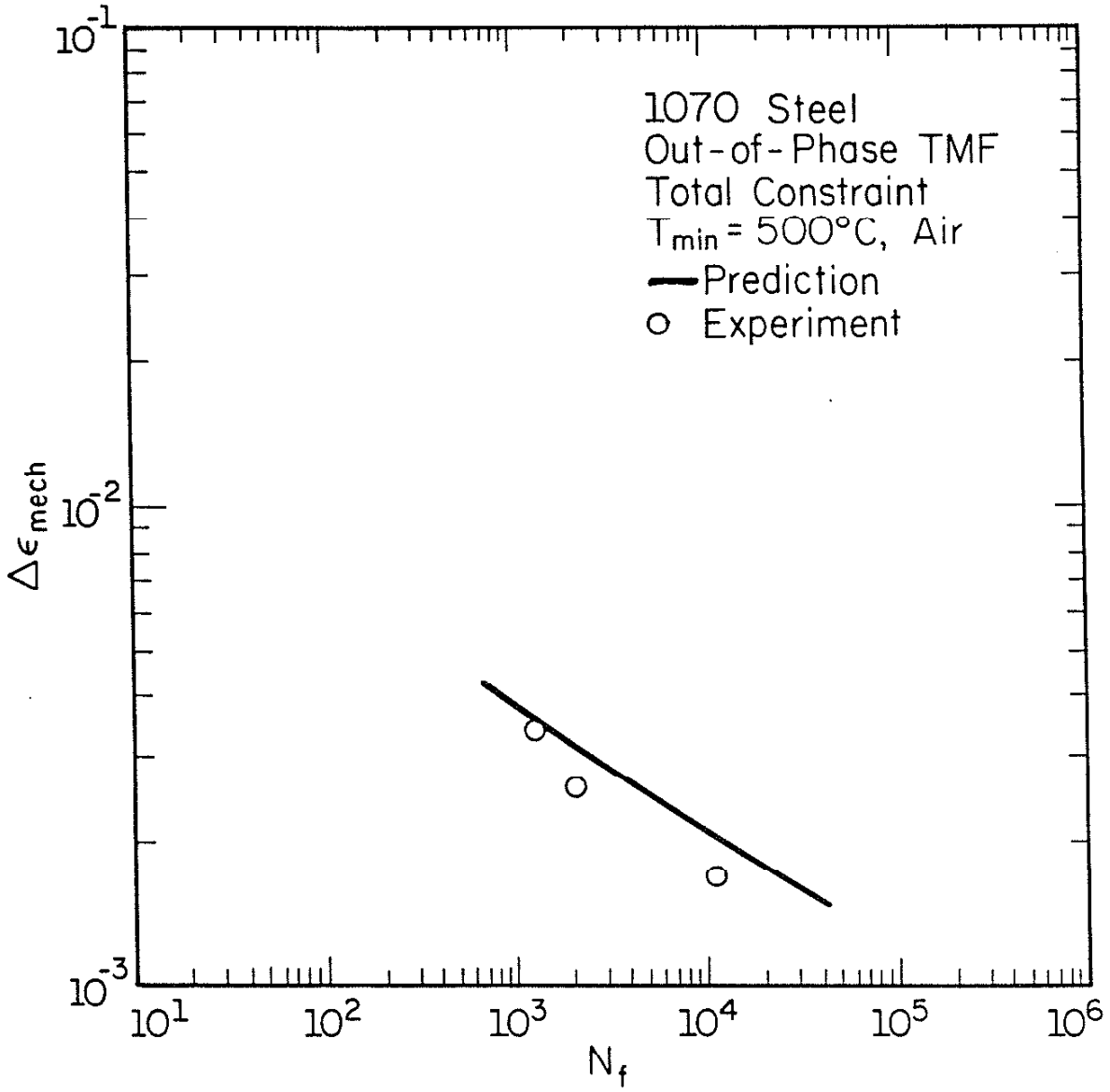


Figure 27 Comparison of predicted and experimental lives for out-of-phase total constraint TMF, $T_{min}$ = 500°C, air.

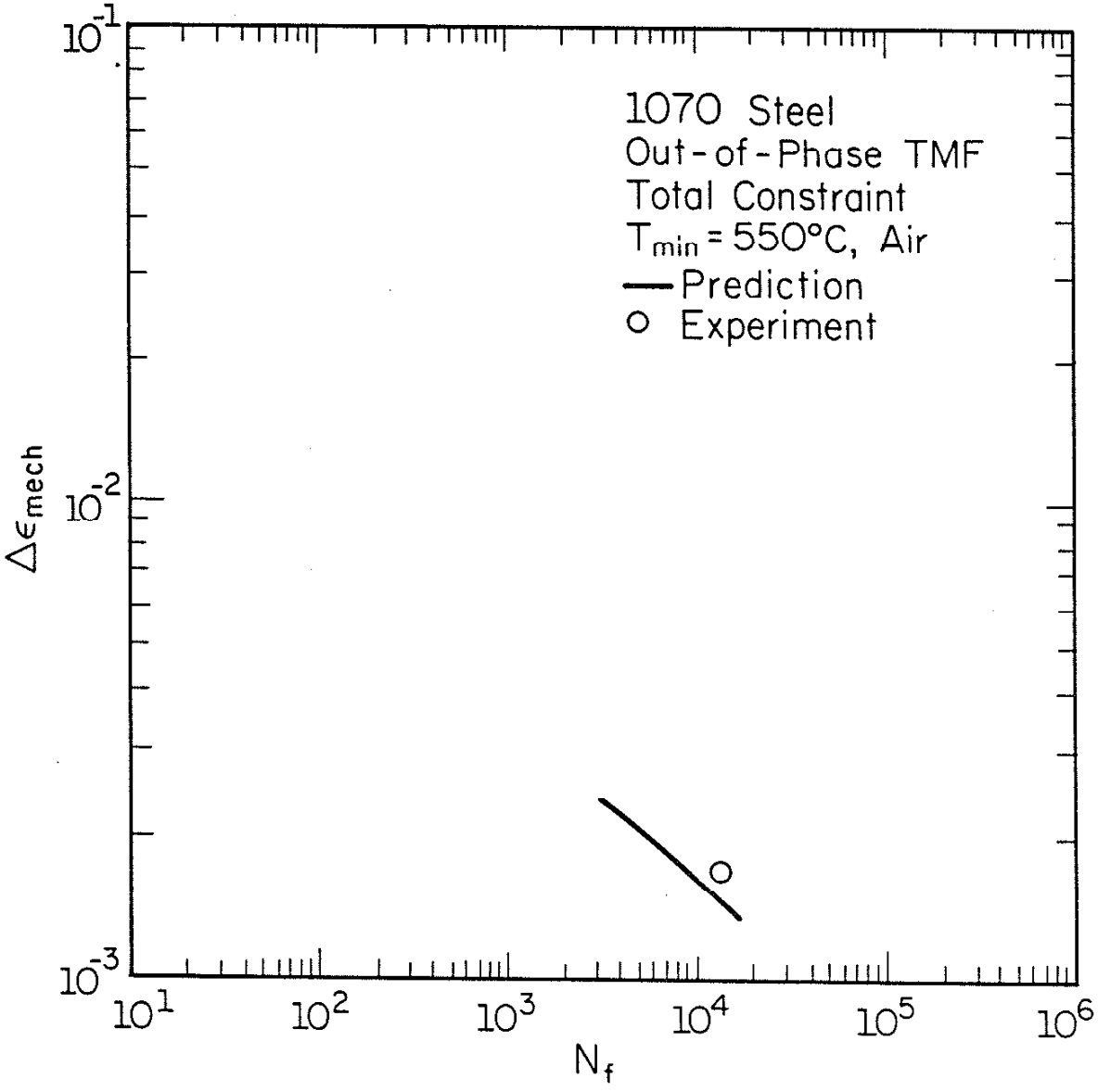


Figure 28 Comparison of predicted and experimental lives for out-of-phase total constraint TMF, $T_{min}$ = 550°C, air.

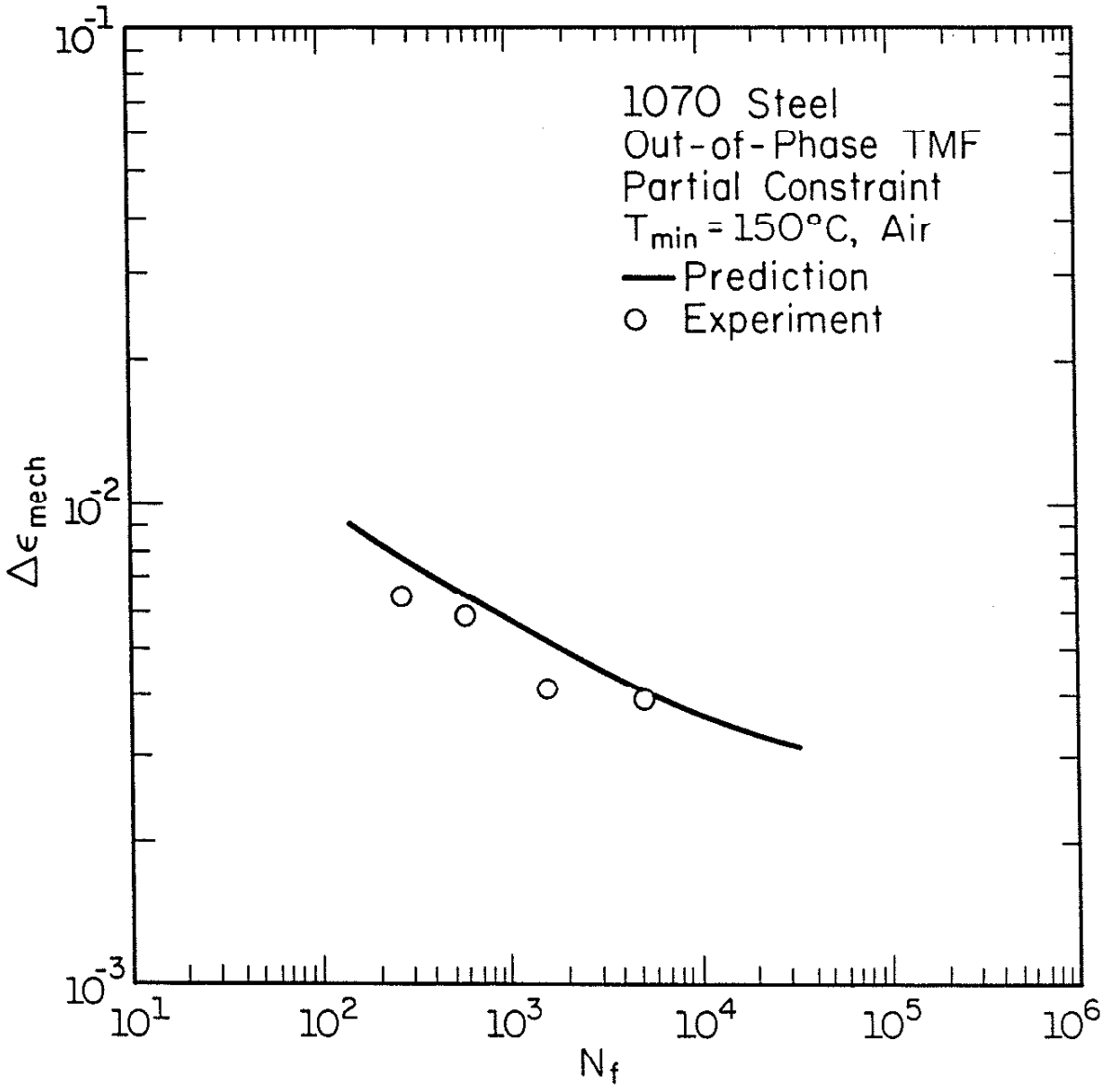


Figure 29 Comparison of predicted and experimental lives for out-of-phase partial constraint TMF, $T_{min}$ = 150°C, air.

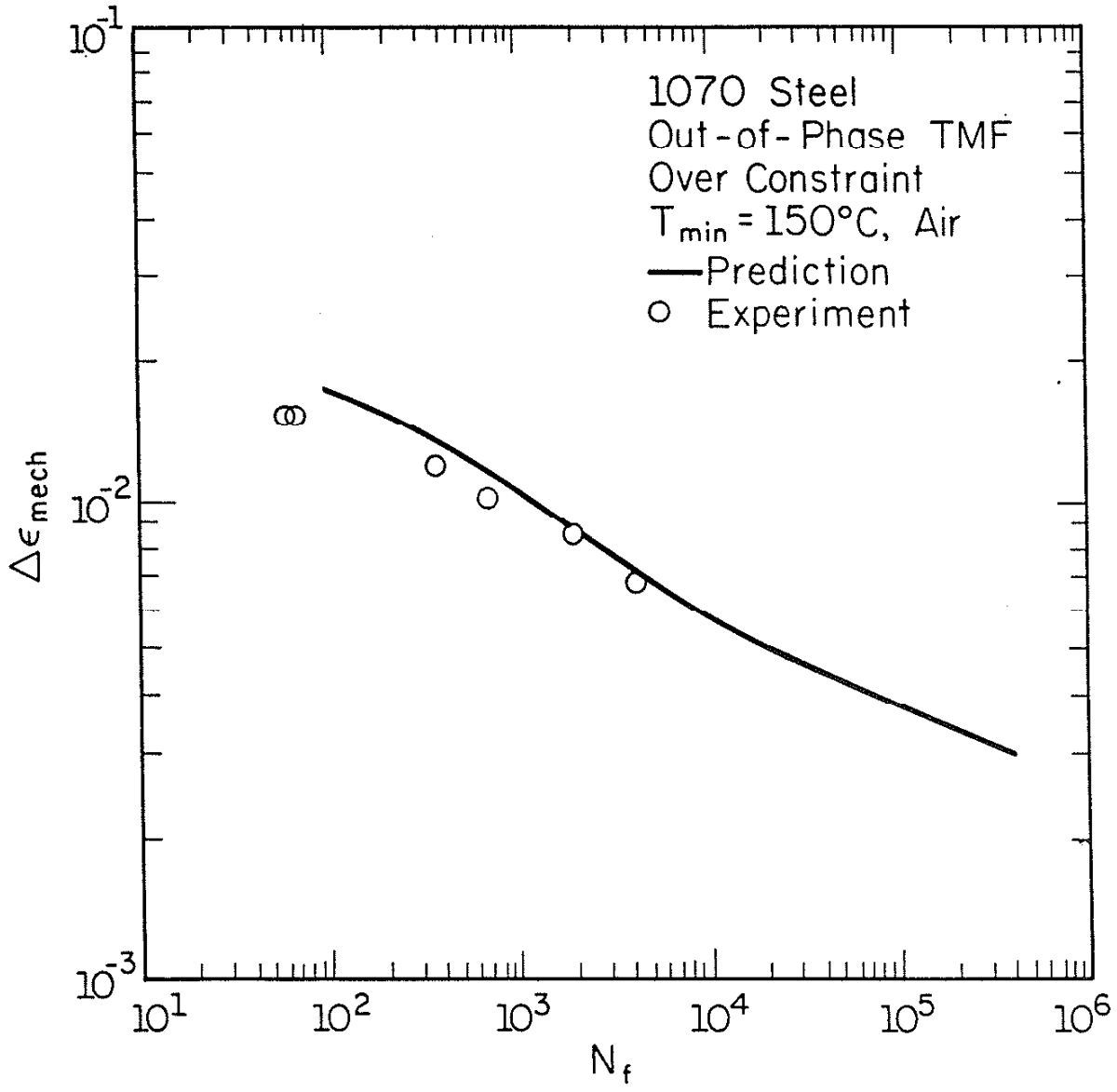


Figure 30 Comparison of predicted and experimental lives for out-of-phase over constraint TMF, $T_{min}$ = 150°C, air.

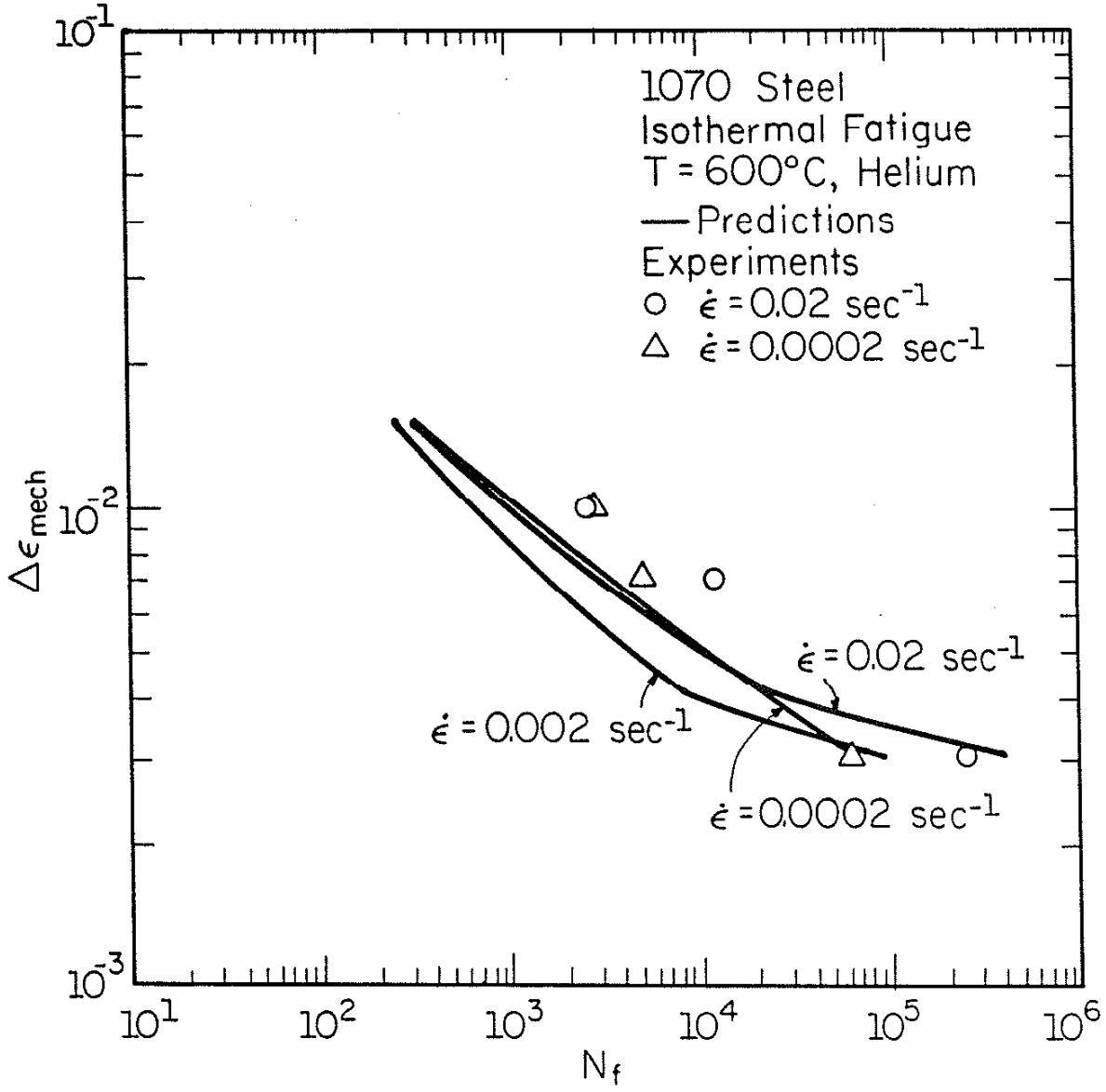


Figure 31 Comparison of predicted and experimental lives for isothermal fatigue, T = 600°C, helium.

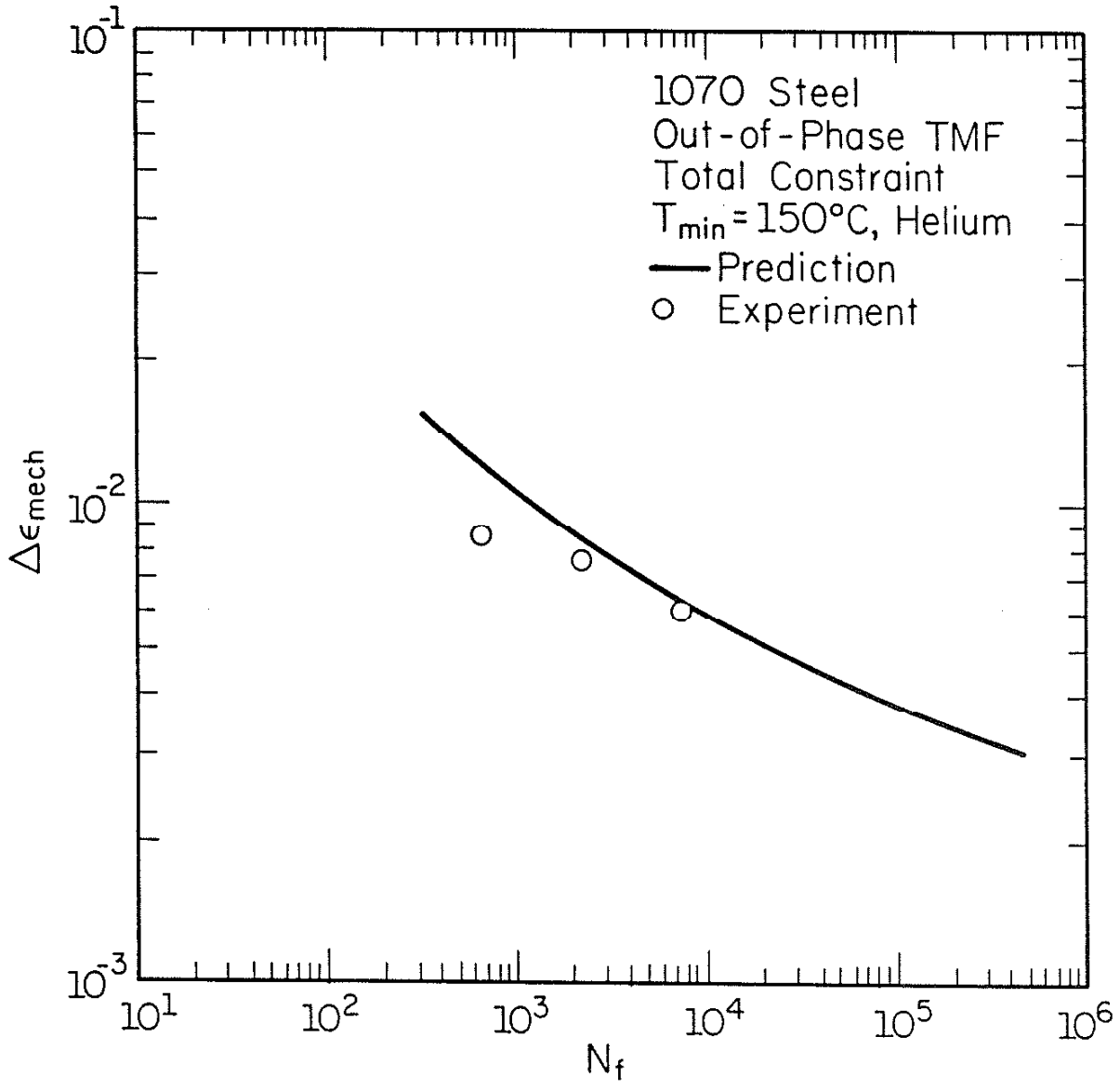


Figure 32 Comparison of predicted and experimental lives for out-of-phase total constraint TMF, $T_{min}$ = 150°C, helium.

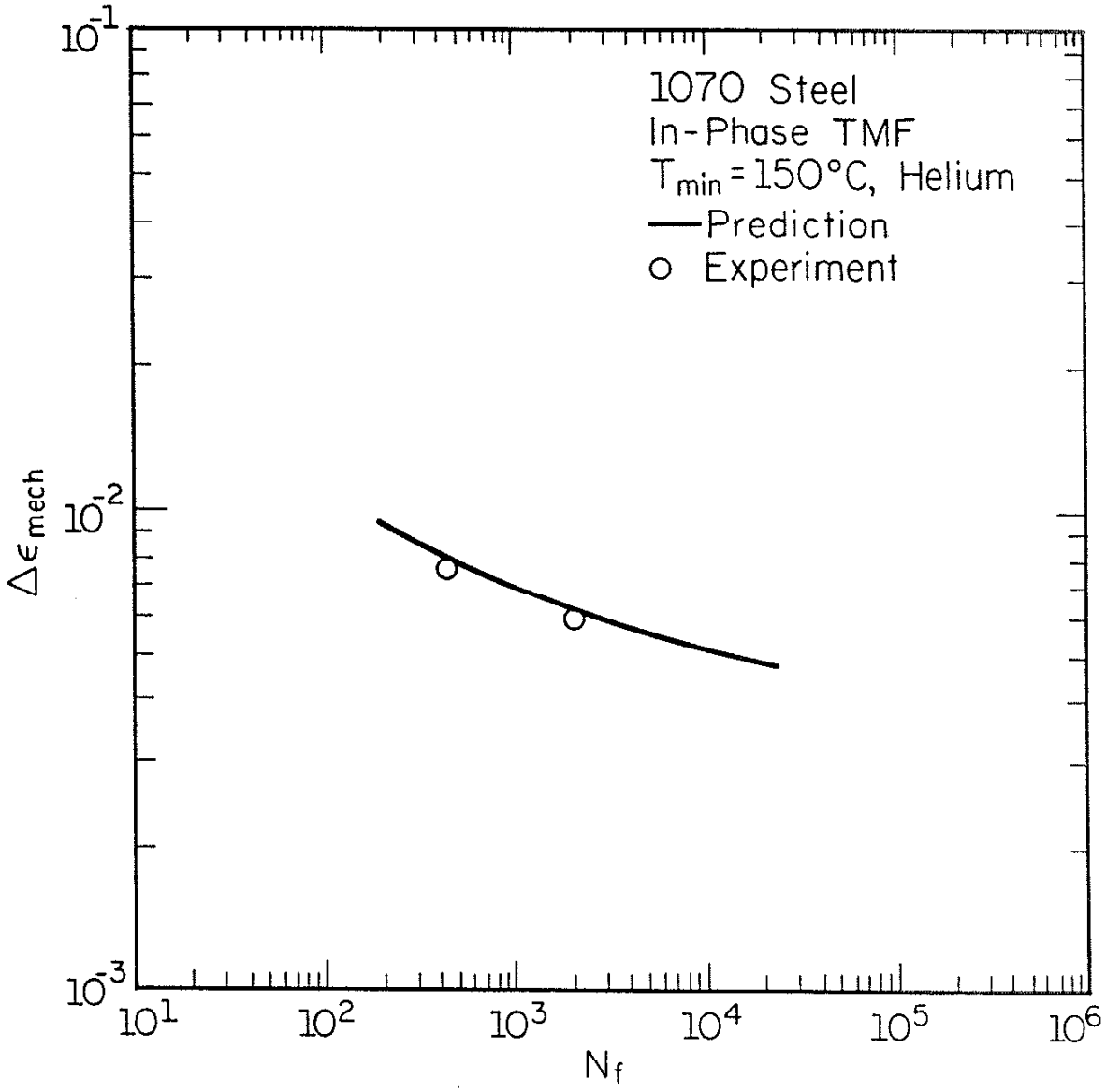


Figure 33 Comparison of predicted and experimental lives for in-phase TMF, $T_{min}$ = 150°C, helium.

## 8. REFERENCES


1. Nelson, R. S., Schoendorf, J. F., and Lin, L.S., "Creep Fatigue Life Prediction for Engine Hot Section Materials (Isotropic) - Interim Report," NASA CR-179550, Dec. 1986.

2. Coffin, L. F., Jr., "Fatigue at High Temperature," *Fatigue at Elevated Temperatures*, ASTM STP 520, 1973, pp. 5-34.

3. Halford, G. R. and Manson, S. S., "Life Predictions of Thermal-Mechanical Fatigue Using Strain Range Partitioning," *Thermal Fatigue of Materials and Components*, ASTM STP 612, D. Spera and D. Mowbray Eds., 1976, pp. 239-254.

4. Kalluri, S., Manson, S. S., and Halford, G. R., "Exposure Time Considerations in High Temperature Low Cycle Fatigue," NASA TM-88934, 1987.

5. Challenger, K. D., Miller, A. K., and Langdon, R. L., "Elevated Temperature Fatigue with Hold Time in a Low Alloy Steel: A Predictive Correlation," *J. Materials for Energy Systems*, Vol. 3, June 1981, pp. 51-61.

6. Antolovich, S. D., Baur, R., and Liu, S., "A Mechanistically Based Model for High Temperature LCF of Ni Base Superalloys," *Superalloys 1980*, 1980, pp. 605-613.

7. Antolovich, S. D., Liu, S., and Baur, R., "Low Cycle Fatigue Behavior of Rene 80 at Elevated Temperature," *Metallurgical Trans. A*, Vol. 12A, Mar. 1981, pp. 473-481.

8. Saxena, A. and Bassani, J. L., "Time-dependent Fatigue Crack Growth Behavior at Elevated Temperature," Proc. AIME on Fracture: Interactions of Microstructure, Mechanisms and Mechanics, Ed. by J. M. Wells and J. D. Landes, 1984, pp. 357-383.

9. Liu, H. W. and Oshida, Y., "Grain Boundary Oxidation and Fatigue Crack Growth at Elevated Temperatures," *Theoretical and Applied Fracture Mechanics*, Vol. 6, 1986, pp. 85-94.

10. Reuchet, J. and Remy, L., "Fatigue Oxidation Interaction in a Superalloy - Application to Life Prediction in High Temperature Low Cycle Fatigue," *Metallurgical Trans. A*, Vol. 14A, Jan. 1983, pp. 141-149.

11. Skelton, R. P. and Bucklow, J. I., "Cyclic Oxidation and Crack Growth During High Strain Fatigue of Low Alloy Steel," *Metal Science*, Feb. 1978, p. 64-70.

12. Coffin, L. F., Jr., "The Effect of High Vacuum on the Low Cycle Fatigue Law," *Metallurgical Trans.*, Vol. 3, July 1972, pp. 1777-1788.

13. Skelton, R., "Environmental Crack Growth in 0.5Cr-Mo-V Steel During Isothermal High Strain Fatigue and Temperature Cycling," *Materials Science and Engineering*, Vol. 35, No. 2, 1978, pp. 287-298.

14. Floreen, S. and Kane, R. H., "An Investigation of the Creep-Fatigue-Environment Interaction in a Ni-base Superalloy," *Fatigue of Engineering Materials and Structures*, Vol. 2, 1980, pp. 401-412.

15. Skelton, R. P., "Growth of Short Cracks During High Strain Fatigue and Thermal Cycling," *Low-Cycle Fatigue and Life Prediction*, ASTM STP 770, 1982, pp. 337-381.

16. Renner, E., Vehoff, H., Riedel, H., and Neumann, P., "Creep Fatigue of Steels in Various Environments," Int. Conf. on Low Cycle Fatigue and Elasto-Plastic Behaviour of Materials, 2nd, Munich, Germany, 1987, pp. 277-283.

17. Bressers, J., Schusser, U., and Ilschner, B., "Environmental Effects on the Fatigue Behavior of Alloy 800H," Int. Conf. on Low Cycle Fatigue and Elasto-Plastic Behaviour of Materials, 2nd, Munich, Germany, 1987, pp. 365-370.

18. Karasek, M., Sehitoglu, H., and Slavik, D., "Deformation and Fatigue Damage In 1070 Steel Under Thermal Loading," *Low Cycle Fatigue--Directions for the Future*, Proc. ASTM Conf., Lake George, New York, Oct. 1985.

19. Halford, G. R. and Saltsman, J. F., "Calculation of Thermomechanical Fatigue Life Based on Isothermal Behavior," Proc. of ASME Conf. on Thermal Stress, Material Deformation, and Thermo-Mechanical Fatigue, Ed. by H. Sehitoglu and S. Y. Zamrik, PVP - Vol. 123, 1987, pp. 9-21.

20. ASME Boiler and Pressure Vessel Code, Case N-47-23, Class 1 Components in Elevated Temperature Service, Section III, Division 1, 1986.

21. Bui-Quoc, T. and Biron, A., "Low-Cycle Cumulative Fatigue Damage on a Stainless Steel at High Temperatures," *Third International Conference on Pressure Vessel Technology*, Part II, ASME, 1977, pp. 853-860.

22. Bernard-Connolly, M., Biron, A., and Bui-Quoc, T., "Low-Cycle Cumulative Damage with Two-Strain Repeated Blocks on a Stainless Steel at High Temperature," Trans. CSME, Vol. 5, No. 3, 1978-79, pp. 173-178.

23. Lemaitre, J. and Plumtree, A., "Application of Damage Concepts to Predict Creep-Fatigue Failures," *Journal of Engineering Materials and Technology*, Trans. ASME, Vol. 101, July 1979, pp. 284-292.

24. Plumtree, A., "Damage Accumulation Methods in High Temperature Fatigue," *Canadian Metallurgical Quarterly*, Vol. 18, 1979, pp. 197-205.

25. Bui-Quoc, T. and Gomuc, R., "A Damage Approach for Analysing the Combined Effect under Creep-Fatigue Loading," *ASME Int. Conf. on Advances in Life Prediction Methods*, ed. by D. A. Woodford and J. R. Whitehead, 1983, pp. 105-113.

26. Chaboche, J. L., "Constitutive Equations in Creep-Fracture Damage," Chap. 4, *Engineering Approaches to High Temperature Design*, Vol. 2, Ed. by B. Wilshire and D. R. J. Owen, 1983, pp. 177-235.

27. Majumdar, S. and Maiya, P. S., "A Mechanistic Model for Time-Dependent Fatigue," *Journal of Engineering Materials and Technology*, Vol. 102, Jan. 1980, pp. 159-167.

28. Majumdar, S., "Thermomechanical Fatigue of Type 304 Stainless Steel," Proc. of ASME Conf. on Thermal Stress, Material Deformation, and Thermo-Mechanical Fatigue, Ed. by H. Sehitoglu and S. Y. Zamrik, PVP - Vol. 123, 1987, pp. 31-36.

29. Wareing, J., "Creep-Fatigue Interaction in Austenitic Stainless Steels," *Metallurgical Trans. A*, Vol. 8A, May 1977, pp. 711-721.

30. Tomkins, B., *Creep and Fatigue in High Temperature Alloys*, ed. by J. Bressers, Applied Science Publishers, London, 1981, p. 111.

31. Jaske, C. E., "Creep-Fatigue Crack Growth in Type 316 Stainless Steel," *ASME International Conference on Advances in Life Prediction Methods*, 1983, pp. 93-103.

32. Tien, J. K., Nair, S. V., and Nardone, V. C., "Creep-Fatigue Interaction in Structural Alloys," Chap. 6, *Flow and Fracture at Elevated Temperatures*, 1985, pp. 179-213.

33. Levaillant, C. and Pineau, A., "Assessment of High-Temperature Low-Cycle Fatigue Life of Austenitic Stainless Steels by Using Intergranular Damage as a Correlating Parameter," *Low-Cycle Fatigue and Life Prediction*, ASTM STP 770, 1982, pp. 169-193.

34. Rie, K.-T. and Schmidt, R.-M., "Lifetime Prediction Under Creep-Fatigue Conditions," Int. Conf. on Low Cycle Fatigue and Elasto-Plastic Behaviour of Materials, 2nd, Munich, Germany, 1987, pp. 223-228.

35. Min, B. K. and Raj, R., "Hold-time Effects in High Temperature Fatigue," *Acta Metallurgica*, Vol. 26, 1978, pp. 1007-1022.

36. Baik, S. and Raj, R., "Wedge Type Creep Damage in Low Cycle Fatigue," *Metallurgical Trans. A*, Vol. 13A, July 1982, pp. 1207-1214.

37. Baik, S. and Raj, R., "Mechanisms of Creep-Fatigue Interaction," *Metallurgical Trans. A*, Vol. 13A, July 1982, pp. 1215-1221.

38. Sehitoglu, H. and Morrow, J. D., "Characterization of Thermo-Mechanical Fatigue," *Thermal and Environmental Effects in Fatigue: Research-Design Interface*, Ed. by C. E. Jaske, S. J. Hudak, Jr., and M. E. Mayfield, ASME, PVP-Vol. 71,1983, pp. 93-109.

39. Sehitoglu, H., "Constraint Effect in Thermo-Mechanical Fatigue," *Journal of Engineering Materials and Technology*, Vol. 107, July 1985, pp. 221-226.

40. Sehitoglu, H., "Material Behavior Under Thermal Loading," *Journal of Pressure Vessel Technology*, Vol. 108, Feb. 1986, pp. 113-119.

41. Sehitoglu, H., "Crack-Growth Studies Under Selected Temperature-Strain Histories," *Engineering Fracture Mechanics*, Vol. 26, No. 4, 1987, pp. 475-489.

42. Leverant, G. R., Strangman, T. E., and Langer, B. S., "Parameters Controlling the Thermal Fatigue Properties of Conventionally-Cast and Directionally-Solidified Turbine Alloys," *3rd Int. Symp. on Superalloys: Metallurgy & Manufacture*, 1976, pp. 285-295.

43. Heil, M. L., Nicholas, T., and Haritos, G. K., "Crack Growth in Alloy 718 Under Thermal-Mechanical Cycling," Proc. of ASME Conf. on Thermal Stress, Material Deformation, and Thermo-Mechanical Fatigue, Ed. by H. Sehitoglu and S. Y. Zamrik, PVP - Vol. 123, 1987, pp. 23-29.

44. Boismier, D. A., Forthcoming Master of Science Thesis, University of Illinois at Urbana-Champaign, 1988.

45. Sehitoglu, H., and Karasek, M., "Observations of Material Behavior Under Isothermal and Thermo-Mechanical Loading," *Journal of Engineering Materials and Technology*, Vol. 108, April 1986, pp. 192-198.

46. Karasek, M. L., "An Investigation into Isothermal and Thermo-Mechanical Fatigue Damage at Elevated Temperatures," *Materials Engineering-Mechanical Behavior*, College of Engineering, Univ. of Illinois at Urbana-Champaign, Report No. 132, Aug. 1986.

47. Morrow, J., "Cyclic Plastic Strain Energy and Fatigue of Metals," *Internal Friction, Damping and Cyclic Plasticity*, ASTM STP 378, 1965, pp. 45-87.

48. Ward, G., Hockenhull, B. S., and Hancock, P., "The Effect of Cyclic Stressing on the Oxidation of a Low-Carbon Steel," *Metallurgical Trans.*, Vol. 5, June 1974, pp. 1451-1455.

49. Forrest, J. E., and Bell, P. S., "The Relationship Between the Deformation of Substrate and Scale in the Mechanism of Multilayer Oxide Formation on Low Alloy Ferritic Steels," *Corrosion and Mechanical Stress at High Temperatures*, Ed. by V. Guttmann and M. Merz, 1981, pp. 339-358.

50. Birks, N. and Meier, G. H., *Introduction to High Temperature Oxidation of Metals*, 1983.

51. Manson, S. S. and Halford, G. R., "Relation of Cyclic Loading Pattern to Microstructural Fracture in Creep-Fatigue," *Fatigue 84*, 1984, pp. 1237-1255.

52. Argon, A. S., Chen, I., and Lau, C., "Intergranular Cavitation in Creep: Theory and Experiments," *Creep-Fatigue-Environment Interactions*, TMS-AIME, ed. by R. M. Pelloux and N. S. Stoloff, 1980, pp. 46-85.

53. Slavik, D., "An Experimentally Based Unified Model for Isothermal and Thermo-Mechanical Loading," *Materials Engineering-Mechanical Behavior*, College of Engineering, Univ. of Illinois at Urbana-Champaign, Report No. 134, Sept. 1986.

54. Slavik, D. and Sehitoglu, H., "A Constitutive Model for High Temperature Loading Part I--Experimentally Based Forms of the Equations; Part II--Comparison of Simulations with Experiments," Proc. of ASME Conf. on Thermal Stress, Material Deformation, and Thermo-Mechanical Fatigue, Ed. by H. Sehitoglu and S. Y. Zamrik, PVP - Vol. 123, 1987, pp. 65-82.

55. Sehitoglu, H., Unpublished work.

56. Manning, M. I., "Geometrical Effects on Oxide Scale Integrity," *Corrosion Science*, Vol. 21, No. 4, pp. 301-316.